From the Institute of Biomedical Optics

of the University of Lübeck

Director: Prof. Dr. rer. nat. Robert Huber

“850 nm Fourier domain mode-locked laser for ophthalmic optical coherence tomography imaging”

Dissertation for fulfillment of requirements

for the doctoral degree of the University of Lübeck,

from the department of Natural Sciences.

Submitted by

Marie Klufts

From Besançon, France

Lübeck, 2025

1st Referee: Prof. Dr. rer. nat. Robert Huber

2nd Referee: Prof. Dr. rer. nat. Christian Hübner

Date of the oral examination: August 8, 2025

Approved for printing. Lübeck, August 11, 2025

“Whatever arises, love that.”

Matt Kahn

ABSTRACT

Non-invasive imaging techniques have become essential in medical diagnostics over the past few decades. Among these, **Optical Coherence Tomography (OCT)** offers micrometer resolution with millimeter-scale depth penetration, making it particularly valuable in ophthalmology. OCT captures backscattered light to generate 3D volumes. For eye imaging, wavelengths around **850 nm** are ideal due to minimal absorption by the vitreous and high scattering in the upper retinal layers. Imaging speed is also critical, as faster speeds reduce motion artifacts. Swept-source OCT, using **wavelength-tunable lasers**, enables high-speed imaging. **Fourier Domain Mode-Locked (FDML) lasers** providing megahertz-level scan rates are ideal for this purpose.

This thesis explores the development and application of FDML lasers for **ophthalmic imaging**. Unlike other tunable lasers, FDML lasers have a unique design that stores a full sweep in their fiber cavity for hundreds of round trips, avoiding rebuilding of lasing from spontaneous emission after tuning to new wavelengths offering **high phase stability** and **long coherence length** necessary for high quality OCT images. A new megahertz FDML laser at 850 nm would merge the unique advantages of this wavelength with the proven benefits of FDML lasers allowing for a low latency, dynamic view of the retina, opening new doors for **real-time diagnostics**.

The first part delves into the challenges of developing an FDML laser around 850 nm, addressing issues like **polarization mode dispersion, chromatic dispersion, and low gain/loss ratios.** These factors contribute to the complexity of managing short wavelength OCT lasers, which explain their scarcity to date. The second part presents ***in-vivo*** **ophthalmic OCT** imaging results, with comparisons to other imaging techniques.

The newly designed FDML laser demonstrates strong performance for OCT imaging, achieving an axial resolution below 10 µm, sensitivity above 84 dB, and a ranging depth of 1.4 cm. Also, its high phase stability, with a time jitter of 25 ps over 1,000 sweeps, makes it suitable for phase-resolved techniques. Retinal images were captured at **414,000 axial scans per second** using a master-slave based calibration technique, at **828 kHz with bidirectional sweeping**, and at **1.7 MHz using optical buffering** with a single-*k*-calibration technique. While increased scattering at 850 nm limits choroidal imaging, most retinal layers of interest are clearly visible.

This FDML laser highlights the advantages of short-wavelength, high-speed imaging and paves the way for new applications.

KURZFASSUNG

Nicht-invasive Bildgebungstechniken haben sich in den letzten Jahrzehnten als unverzichtbarer Standard in der medizinischen Diagnostik etabliert. Unter diesen bietet die **optische Kohärenztomographie** (Optical Coherence Tomography, OCT) eine mikrometergenaue Auflösung bei Eindringtiefen im Millimeterbereich, was sie besonders wertvoll in der Ophthalmologie macht. Die OCT erfasst rückgestreutes Licht, um dreidimensionale Volumenbilder zu erzeugen. Für die Augenbildgebung sind Wellenlängen um **850 nm** ideal, da sie minimale Absorption im Glaskörper und hohe Streuung in den oberen Netzhautschichten aufweisen. Die Bildgebungsgeschwindigkeit ist ebenfalls entscheidend, da höhere Geschwindigkeiten Bewegungsartefakte reduzieren. Die OCT mit schnell durchstimmbaren Lasern (swept source OCT), ermöglicht hochgeschwindigkeitsfähige Bildgebung**. Fourier domain mode-locked (FDML)-Laser** mit Scanraten im Megahertz-Bereich sind hierfür besonders geeignet.

Diese Dissertation untersucht die Entwicklung und Anwendung eines 850 nm FDML-Lasers für die **ophthalmische Bildgebung**. Im Gegensatz zu anderen schnell durchstimmbaren Lasern zeichnet sich der FDML-Laser durch sein einzigartiges Design aus, bei dem ein vollständiger Frequenzdurchlauf (sweep) über Hunderte von Umläufen in seinem Resonator gespeichert wird. Dies vermeidet die Notwendigkeit nach den Wiederaufbau der Laseremission aus spontaner Emission nach der Abstimmung auf eine neue Wellenlänge und ermöglicht eine **hohe Phasenstabilität** sowie eine **lange Kohärenzlänge**, die für hochwertige OCT-Bilder erforderlich sind. Ein neuer Megahertz-FDML-Laser bei 850 nm würde die einzigartigen Vorteile dieser Wellenlänge mit den bewährten Vorzügen von FDML-Lasern vereinen und so eine latenzarme, dynamische Darstellung der Netzhaut ermöglichen, wodurch neue Türen für **Echtzeitdiagnostik** geöffnet würden.

Der erste Teil befasst sich mit den Herausforderungen bei der Entwicklung eines FDML-Lasers im Bereich von 850 nm und behandelt Themen wie **Polarisationsmodendispersion, chromatische Dispersion und geringe Verstärkung bei hohen optischen Verlusten im Resonator**. Diese Faktoren tragen zur Komplexität von OCT Lasern mit kurzen Wellenlängen bei und erklären ihre bisherige Seltenheit. Der zweite Teil präsentiert Ergebnisse der ***in-vivo*** **ophthalmischen OCT-Bildgebung** und vergleicht diese mit anderen Bildgebungstechniken.

Der neu entwickelte FDML-Laser erreicht eine axiale Auflösung von unter 10 µm, eine Sensitivität von über 84 dB und eine Bildgebungstiefe von 1,4 cm. Darüber hinaus ermöglicht die Phasenstabilität des Lasers, mit einer zeitlichen Schwankung von 25 ps über 1.000 Sweeps den Einsatz in phasenauflösenden Techniken. Netzhautbilder wurden mit **414.000 axialen Abtastungen pro Sekunde** unter Verwendung einer *master-slave*-basierten Kalibrationstechnik, mit **828 kHz**

bei bidirektionalem Durchstimmen und mit **1,7 MHz unter Nutzung von optischer Pufferung** mit einer *single-k-Kalibrationstechnik* aufgenommen. Während die erhöhte Streuung bei 850 nm die Bildgebung der Choroidea einschränkt, sind die meisten relevanten Netzhautschichten deutlich sichtbar.

Dieser FDML-Laser unterstreicht die Vorteile der hochgeschwindigkeitsfähigen Bildgebung bei kurzen Wellenlängen und ebnet den Weg für neue Anwendungen.

ACKNOWLEDGMENTS

"Lebe, liebe, lache in der Stadt der sieben Türme."

I would like to extend my heartfelt gratitude to the City of Lübeck for providing an enchanting backdrop for my journey, where I experienced a sweet and enriching life.

I'm grateful to the Marie Skłodowska-Curie Actions for providing the best conditions for PhD candidates. NETLAS has offered me invaluable teaching and networking, allowing me to explore various labs and countries. It truly represents the pinnacle of grants for aspiring researchers.

Robert, thank you for everything. Thank you for all what you taught me during these four years, whether in physics or in life. From our first interview, I genuinely sensed that working under your guidance would be the best thing that could happen to me. I'm excited about the projects we will tackle in the future. From whom I learned it all. Vergelt's Gott!

Hear ye, hear ye, Huber's young stars. Asim, Madita, Philipp, Sazgar, Simon, and Wolfgang, there we are, all on our way to our doctorate. I couldn't have hoped for better colleagues. A special thank you to Simon, who carried me for two years before I flew off to new horizons.

Where my beloved laser first saw the sun, München. I would like to thank Optores, my dear flatmates, and friends from Bavaria. Such an amazing, sweet, and pleasant summer life.

Where my beloved laser illuminated its first retina, Canterbury. Huge thanks to the AOG and to our dear Owl Nest for taking care of me for these seven months. A special thanks to Adrian^2 for their close guidance and supervision, which enabled me to reach my ultimate goal.

Alejandro, my mate. Cheers to all the hard work, our personal growth and the adventures that lie ahead. Gracias por estar siempre ahí, iluminando mi vida con tu amistad y apoyo incondicional.

A special shoutout to Ramona and Bianka for being the paperwork wizards of the century! Thanks for helping me navigate through the bureaucratic maze and crossing borders smoother than a well-oiled machine. Well, maybe just a tiny hiccup or two, but we made it!

Because wherever you are and wherever you go, we will be together. Ankita, Léo, Yektâ, Marion, Carla, Sacha, Philipp. Because you are the best.

Maman, Papa, Julie. Merci de m'avoir laisser partir ici et là, et de m'avoir ouvert les portes vers un monde vaste et magnifique. Oh, et merci pour avoir fait l'effort de lire jusqu'ici, bon courage !

À Lydie, Mathilde, Naomi, Théo, pour avoir été là avant, pendant, et après. Pour tous ces appels, ces messages partagés. Merci du fond du cœur. À tous mes amis, ma famille qui ont tout donné pour tenter de comprendre et d'entrevoir mon nouveau monde.

Mon cœur, mitt røde eple, these past few months with you by my side have been something special, something more. Thank you for being here. More, always more.

CONTENTS

1. INTRODUCTION

Medical imaging plays a pivotal role in contemporary healthcare, facilitating the early detection and characterization of pathological conditions often imperceptible to the unaided human eye. Modalities such as ultrasound and magnetic resonance imaging afford clinicians intricate insights into tissue morphology and pathology without necessitating invasive procedures. Optical coherence tomography (OCT) emerged as a non-invasive optical imaging modality akin to ultrasound. Their difference lies in the fact that OCT is based on white light interferometry. It measures the intensity of backscattered light as a function of its depth in the sample. Furthermore, since light travels much faster than the speed of sound, the delay of the reflected wave cannot be measured like in ultrasound technology. Instead, an interferometer setup must be employed where the light reflected from the sample is superimposed with light reflected from a reference mirror, and the resultant interference pattern is detected. Images can be acquired volumetrically, referred to as C-Scans. Within a C-Scans, each frame constitutes a B-Scans, while an individual column within a B-Scans is termed an A-Scans (Figure 1, right). The term *en-face* is employed to describe a cross-sectional image of the OCT data, parallel to the surface of the sample (top view) at one depth. OCT can bring information about biological tissue only up to a few millimeters' depth but with micrometer axial and lateral resolution, as shown in Figure 1, typically 10s of micrometers.

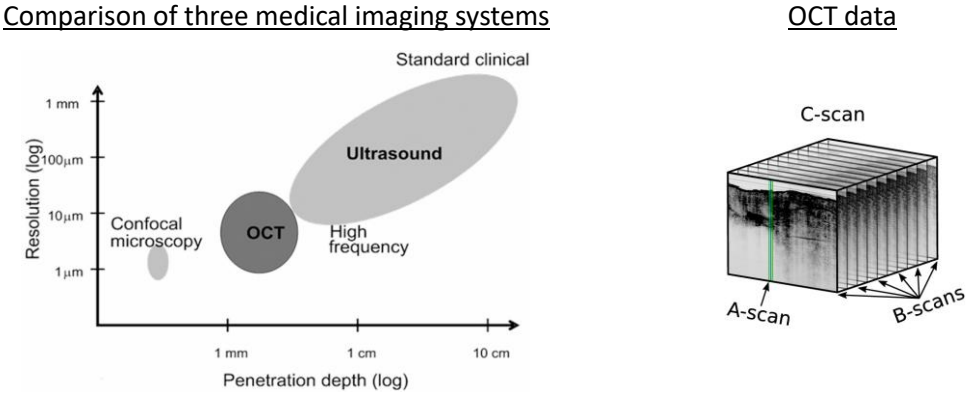

Figure 1. Left: comparison of the resolution and penetration depth of different medical imaging systems [1]. Right: visual depiction of OCT Data. [2]

In OCT, the choice of light source stands as a critical determinant in the attainment of high-quality images. The inherent characteristics of the light source significantly influence both depth and transverse resolution. Moreover, its operational mechanisms dictate the data acquisition speed, also defining the A-Scans repetition rate, directly impacting measurement duration, patient comfort, and image fidelity. Notably, a faster light source mitigates the deleterious effects of patient motion on data quality. Swept-source lasers are on the rising edge in the field of OCT because of their high speed, i.e. high A-Scan repetition rate. Thanks to their mechanisms, which are detailed later in this thesis, they enable to rapidly sweep through a range of optical frequencies. The laser

output is then composed of a succession of wavelengths. The advent of swept-source technology stimulated the development of swept-source OCT (SS-OCT), representing just one technology among the diverse branches of OCT. It distinguishes itself by offering enhanced sensitivity roll-off over longer axial scan ranges and higher speed data acquisition.

Well-known in the SS-OCT community for their high speed, Fourier domain mode-locked (FDML) lasers are fiber lasers with a semiconductor gain medium [3]. They rapidly tune their spectral bandwidth up to 150 nm [4] over a million times per second with an instantaneous linewidth of about ~6 kHz [5]. In an FDML laser, a complete sweep is optically "stored" inside the cavity during several hundreds of round-trip. This is made possible by having a long fiber delay line of ~500 m that acts as a resonator. This storing enhances laser coherence, ensuring that the emitted wavelengths maintain consistent phase relationships over time. Additionally, it enables the laser to amplify each wavelength without the need to build back the sweep from spontaneous emission, resulting in improved signal-to-noise characteristics. They are typically used for ophthalmic and skin imaging [6-10], or stimulated Raman spectroscopy [11, 12]. They also have proven their useful implementation in endoscopic imaging [13], or intravascular imaging [14-16]. Also due to their high phase stability, FDML lasers can be used for phase-sensitive imaging [17, 18]. Depending on the application and the need, 1060 nm, 1300 nm, and 1550 nm FDML lasers are available on the market and manufactured by Optores GmbH. To date, a 1200 nm laser has also been reported in research [19].

The interest in shorter wavelength FDML lasers primarily stems from the prevalent application demands within the ophthalmology field, representing a substantial market segment for OCT technology [20]. From the first scientific article published in 1991 [21], to 2,500 published articles in the year 2015, the number of publications keeps increasing showing the interest of the scientific world. The clinical realm has also witnessed a remarkable adoption of OCT, with over 34,000,000 retinal scans conducted annually, highlighting its pivotal role in contemporary ophthalmic imaging practices. 850 nm is the standard wavelength for most commercial spectral-domain OCT (SD-OCT) systems used for retinal imaging due to the low water absorption at this wavelength. Indeed, prior to reaching the retina, the incident light traverses through ~2 cm of aqueous environment of the human eye, akin to water. Consequently, it necessitates the utilization of a light source less susceptible to water absorption for optimal imaging efficacy. Also, light sources at lower wavelengths enable better axial resolution for a comparable optical bandwidth, and an enhancement of the lateral resolution. However, all the clinical devices use a different branch of OCT technology, they operate on SD-OCT. This technology does not use swept-sources but broadband light sources. Instead of having each wavelength propagating after the other, they send all wavelengths together to the sample and split them afterward using a spectrometer. The latter limits the speed of the system to a few 100s of kilohertz [22, 23]. Since SS-OCT is currently the only method capable of achieving the MHz frame rates necessary for motion artifact-free ophthalmic OCT,

this thesis focuses on this technique. Retinal imaging is already practiced with SS-OCT in research using 850 nm swept-sources [24-27]. However, the fastest speed achievable with these lasers is limited to 50 kHz, which does not confer significant advantages over commercially available SD-OCT. Developing high-performance FDML lasers at 850 nm presents significant challenges, primarily due to the limited availability and low performance of broadband fiber components. At shorter wavelengths, components face issues such as polarization mode dispersion (PMD), higher optical losses, and lower gain. These combined obstacles make the development of efficient sources at this wavelength particularly difficult. Consequently, 1060 nm swept-sources have emerged as the preferred choice in contemporary research endeavors [7-9, 28-30]. This wavelength presents distinct advantages for retinal imaging owing to a drop in water absorption and deeper penetration depth due to less scattering in tissue compared to 850 nm laser sources. However, for the same reason, it leads to lower contrast in the upper retinal layers. Besides, due to the water absorption effect, their depth resolution can hardly be below 4 µm. The main advantage of these sources lies in their speed, high stability, high gain and availability of components. For instance, a 1060 nm FDML laser can reach up to ~3 MHz and a coherence length supporting fringe frequencies above most photodetectors' electrical bandwidth (~1.6 GHz fringe frequency) [8].

Developing a new FDML laser at 850 nm merges the proven benefits of FDML lasers with the unique advantages of this wavelength. The higher scattering at this wavelength in the upper retinal layers and the enhanced lateral resolution, enabling sharper and more detailed images. Coupled with megahertz A-Scan acquisition speeds, this could revolutionize retinal imaging by delivering higher-quality scans in real time. Additionally, the faster acquisition rates would reduce sensitivity to patient motion, minimizing the need for post-processing corrections and potentially allowing for a low-latency, dynamic view of the retina, opening new doors for real-time diagnostics.

This thesis presents a novel 850 nm FDML laser source and its development [31], all the challenges raised by this wavelength, and the final performances that have been achieved. It has been used *in-vivo*, and retinal images have been acquired with two different processing techniques, the Complex Master-Slave technique and what is named here "single-*k*-calibration". The thesis concludes with a comparative analysis of images generated through both processing techniques, supplemented by a comparative evaluation of retinal images obtained using a 1060 nm FDML laser in the past.

2. BASICS AND THEORY

In this chapter, the basics and the theory necessary for understanding the following chapters of this thesis are explained and detailed. Starting with a detailed description of OCT. How can a cross-sectional image of human tissue be created from a laser light source. The main characteristics of OCT are presented along with two different ways on how to acquire images: complex Master-Slave and single-*k*-calibration.

To provide context for the focus on retinal imaging OCT, a brief overview of ophthalmology with the structure of the human eye and a twenty-year period of evolution of retinal OCT is retraced. How ophthalmologists were using OCT, and how they use it nowadays to improve and refine their diagnosis for specific pathologies.

An introduction to lasers and specifically to swept-sources is detailed in the second part. Semiconductor emitters and a few laser technologies of tuning modalities are briefly introduced. An emphasis is on Fourier-Domain Mode-Locked lasers in the third part. Their design, their main components, and the related existing market are presented.

2.1. Optical coherence tomography (OCT)

This section focuses on presenting OCT, from a general point of view to its more detailed and important characteristics. Special attention is paid to SS-OCT, which is the core of the manuscript. The theory behind the axial and lateral resolution and the sensitivity are detailed. The advancements in OCT for retinal imaging are presented, along with a description of the characteristics of the human eye.

2.1.1. General introduction on OCT

OCT is an interferometer-based imaging technique widely used for its ability to capture high-resolution images of biological tissues, particularly in retinal imaging. It works by measuring the interference of light waves reflected from different depths within a sample.

OCT is powerful because of its capability to detect small electric fields. When the light is reflected by a sample $E_s(t)$, depending on the scattering of the sample, only a very small field comes back. It can sometimes be on a scale down to $10^{-13}\ W$, equivalent to a couple of photons. To effectively capture such a weak signal, a heterodyne gain is employed. This involves combining the returning light from the sample $E_s(t)$, with a large electric field coming from a reference arm $E_r(t)$ where a mirror is used to reflect the light, as shown in Figure 2, resulting in a significantly enhanced intensity I_D.

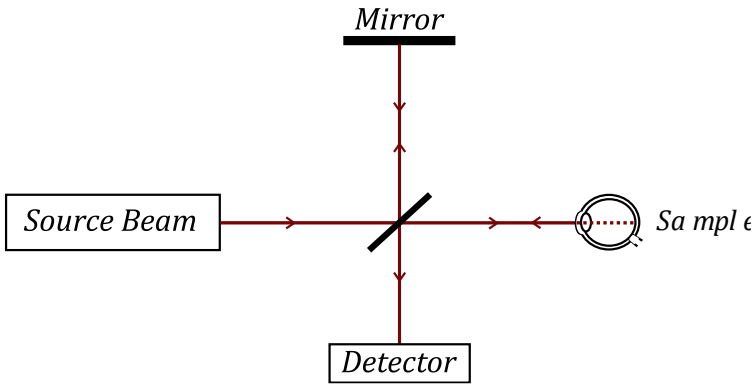

Figure 2. Schematic of a Michelson interferometer. A light source emits a beam that reaches a 50/50 beam splitter, dividing it into two paths. One part is directed toward a reference mirror, while the other travels to the sample — in this case, an eye. The backscattered light from both arms interferes at the beam splitter and is detected by a detector. Variations in the time delay between the sample and the mirror result in different interference frequencies being detected.

When both fields $E_s(t)$ and $E_r(t)$ come back from both arms, they interfere at the beam splitter. Depending on the difference in path length ΔL and the wavelength λ, the intensity I_D

$$I_D \sim |E_r|^2 + |E_s|^2 + 2 \cdot E_r \cdot E_s \cos\left(\frac{4\pi}{\lambda}\Delta L\right) \tag{1}$$

is measured by a detector. With:

$$E_r = A_r e^{i(\omega t - kz)} \; and \; E_s = A_s e^{i(\omega t - kz)} \tag{2}$$

Where A_r and A_s depend on the reflectivity of the mirror and sample respectively, with ω the angular frequency, k the wavenumber, t the time and z the position along the direction of propagation of the wave.

OCT stands out among interferometric techniques by employing short coherence interferometry. In methods utilizing monochromatic light, distance measurement often faces an inherent ambiguity of 2π. However, with OCT's broad spectrum, this ambiguity is mitigated, allowing for direct recovery of various path lengths without such limitations.

OCT can be separated into two main categories: Time Domain OCT (TD-OCT) and Fourier Domain OCT (FD-OCT). While TD-OCT requires a translation of the reference mirror along the beam axis to generate interference at each point in depth in the sample, which leads to a long image acquisition time, FD-OCT allows the entire depth profile to be acquired in one measurement in the spectral domain. Each scattering layer of the sample reflects the incoming beam, resulting in a complex interference pattern composed of each single interference at every depth. Both, TD-OCT and FD-OCT support two different imaging approaches. To acquire volumetric images, a scanning mechanism can be used to move the laser beam across the sample in a method known as "flying-spot" technology. The scanning pattern can vary, but data is captured at each point using a photodetector, generating a sequence of A-Scans. Alternatively, full-field illumination can be used, where the entire sample is illuminated at once. In this case, a camera is employed

to capture the entire volume of data in a single shot, eliminating the need for a scanning mechanism.

When focusing on FD-OCT, it is branched into two sub-systems, SD-OCT and SS-OCT. In the case of SD-OCT, a broadband light source, such as a superluminescent diode, is used. The interference resulting from the combination of the reference arm and sample arm fields after the diffraction grating or spectrometer are detected by a fast line scan camera. The read-out time of these CCD cameras limits the data acquisition speed to around 600 kHz [32]. One disadvantage of this method lies in its complexity and cost. Also, full-field illumination is not possible here.

In SS-OCT, the laser light source rapidly sweeps its wavelength over a broad range. We call a "sweep" the complete cycle in which the laser scans through the entire range of wavelengths. SS-OCT allows the detection of interference across all depth-resolved frequencies in a single scan. In the case of full-field (FF-SS-OCT), as the whole sample and the acquisition of all data is done in one single shot, data acquisition is faster, in the range of 1 kHz volume rates [33]. Thanks to its advanced technology, FF-SS-OCT allows for the acquisition of a phase stable pattern over one *en-face* plane, enabling the observation of the reaction of photoreceptors and nerve in the retina under a light stimulus [34]. However, one drawback is the decrease in sensitivity due to shorter integration times and multiple scattering. Compared to flying-spot SS-OCT, another disadvantage lies in the noise suppression of the light source. In flying-spot imaging, achieving balanced detection is easily attainable due to the use of balanced photodetectors to acquire signals. The interference pattern is split before reaching the detector, allowing both a negative and a positive detector to capture the signals, which are then added to enhance signal quality. In contrast, full-field imaging would require two 2D cameras where each pixel must correspond.

The limitations observed in SD-OCT and FF-SS-OCT have directed this thesis project to focus toward enhancing flying-spot swept-source technology. This approach aims to refine SS-OCT, aligning its speed with that of full-field capabilities while concurrently preserving the high sensitivity and resolution akin to what SD-OCT can accomplish. The next sub-section presents a deeper description of the acquisition of the SS-OCT signal.

2.1.2. Generation of the SS-OCT signal

In the case of swept-sources, a sweep is sent into an interferometer. The source sweeps through a range of frequencies, which results in the pattern shown in Figure 3. When the sweep from the reference and sample arm superimposes, their electromagnetic waves interfere and result in a beat frequency (also called *fringe*). The frequency of the interference term depends on the optical delay, as shown in equation (*1*) above. The photodetector measures the intensity of the resulting beating signal. Due to the limited electrical bandwidth (i.e. below 2 GHz, meanwhile electromagnetic fields vary around 230 THz), only the signal's envelope is measured. The envelope carries information on the delay between both arm lengths. It is important to note that in FD-OCT, the

signal often experiences a decay as the delay increases (sensitivity roll-off). This decline is primarily attributed to the finite coherence length of the light source. As the delay between the sample and reference arms grows, so does the path length difference, leading to reduced interference visibility due to decreasing coherence between the arms. The photo-detected signal arriving from the interference of both arms is commonly known as the channel spectrum and will be used in this thesis.

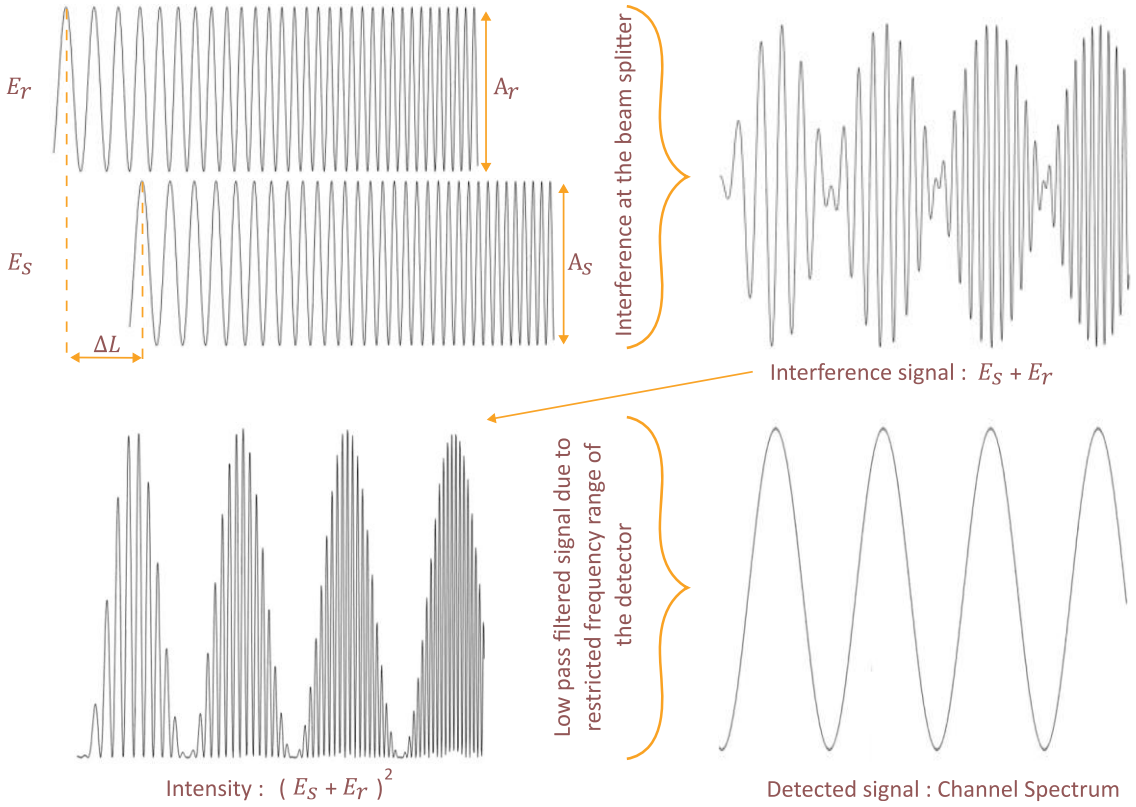

Figure 3. Measurement of the OCT signal in SS-OCT. Both field E_r and E_s coming back from the reference and sample arm with an amplitude of A_r and A_s respectively, experience a delay ΔL. Their superposition at the beamsplitter generates an interference signal. Only the intensity of this signal is measured. Due to the low electrical bandwidth of balanced photodetector, only the envelop of the signal is measured. The detected signal is called channel spectrum [35].

Once the envelope of the intensity of the interference signal is detected by a balanced photodetector, it is sampled via an analog-to-digital converter (ADC). The higher the sampling rate the more information can be acquired. If a fixed ADC clock is used, the signal is sampled equally in time. Since a discrete Fourier transform is performed afterwards to obtain a depth scan, also called A-Scan, the interference channel spectrum must be highly linear in k-space to ensure a sharp A-Scan. However, depending on the swept-source used, it is likely to sweep slower at the extremity of the sweep than in the center due to the deceleration of the mechanical means on the edges, as detailed in the sub-section 2.2.2 presenting several types of swept-sources. A rescaling, also known as calibration, is then necessary to obtain a linear sweep.

One of the main calibration methods used is called k-clocking. Another interferometer and photodetector in parallel to the OCT is used to acquire high frequency interferences. All zero

crossings of this signal trigger the acquisition card to capture data. In this way, each channel spectrum is acquired linearly in k-space [36]. Computational methods can also be used to linearize in k-space the wavelength linear channel spectrum. They are based on linearizing the channel spectrum using the signal phase, which is calculated via a Hilbert transform. The inverse of the phase is used to resample. Once the signal is linearized, a discrete Fourier transform is performed, and the depth scan is obtained [37]. In the case of FDML laser, due to their high sweep-to-sweep stability, k-clocking is not required, hence the name single-k-calibration. Only one calibration spectrum is acquired before an imaging session and used to calibrate all channel spectra. A mirror can simply replace the sample for the calibration spectrum acquisition, which avoids building another interferometer.

Another processing technique called complex master-slave (CMS) interferometry, can also be used to obtain depth scans [38, 39]. Here, the photo-detected channel spectrum is not resampled using directly an external calibration spectrum. Instead, CMS uses two main step processes. At the calibration stage (Master), several calibration spectra are acquired at different delay ΔL. After that, the phases from the photo-detected channel spectra are used to calculate $g(k,z)$ and $h(k)$, which regards to the nonlinearities of the sweep and the unbalanced dispersion respectively. It uses a Hilbert transform:

$$\begin{matrix} E(k,z_1) \\ E(k,z_2) \end{matrix} \xrightarrow{\text{hilbert transform}} \begin{matrix} \varphi_1 = gz_1 + h \\ \varphi_2 = gz_2 + h \end{matrix} \longrightarrow \begin{cases} g = \dfrac{\Delta\varphi}{\Delta z} \\ h = \varphi_1 - gz_1 \end{cases} \tag{3}$$

Here z_1 cannot be determined straightforwardly because of the chirp of the sweep. For this the Fourier transform of $E_1(k,z_1)$ and $E_2(k,z_2)$ is applied. $dz = z_2 - z_1$ is then determined and z_1 can be recovered. To avoid the influence of any phase jump that could arise from the swept-source, more than two masks are acquired and averaged together, which in the end gives:

$$\begin{cases} \bar{g} = \dfrac{\sum g_i}{n} \\ \bar{h} = \dfrac{\sum h_i}{n} \end{cases} \tag{4}$$

With n the number of masks acquired. Once computed these two functions, theoretical channel spectra can be computed for different ΔL and are placed in the rows of a matrix. This matrix T, can be defined as:

$$T(k,z) = \sum_{j=1}^{M}\sum_{i=1}^{N} \frac{\partial g(k_i,z_j)}{\partial k_i} e^{j(g(k_i,z_j)z_j + h(k_i))} \tag{5}$$

$T(k,z)$ is finally known. The rows correspond to the wavenumbers of the sweep, with a total of M samples, and the columns being the theoretical channel spectra inferred, N. At the measurement stage (Slave), the sample replaces the mirror and the acquired channeled spectrum (CS) obtained is multiplied with the set of masks from $T(k,z)$:

$$A(z_i) = \sum_{k=k_{min}}^{k_{max}} T(k_i, z) CS(k_i) \tag{6}$$

The results are integrated over the wavenumber *k* and each multiplication delivers the amplitude of the A-Scan.

CMS processing, in contrast to k-clocking or other calibration methods, enables choosing how many axial points will compose the A-Scan. The number of points used in the A-Scan is determined by the number of masks used in *T(k,z)*. However, it is not entirely arbitrary. Its upper limit is defined by the Nyquist theorem and a lower limit defined by the theoretical axial resolution of the system. Each axial point should be not further apart than half of the resolution. When the number of points is reduced according to the axial range, it enables high real-time processing speed [39]. Apart from this specificity, k-clocking and CMS show the same performance regarding axial resolution and sensitivity, presented in the following sub-section.

As mentioned previously, balanced photodetectors are used to detect the SS-OCT signal. It provides an elimination of all common-noise generated by the reference and sample arm which improves the signal to noise ratio (SNR) and leads to enhanced sensitivity. Also, since the noise is suppressed, weaker signals can be detected which extend the dynamic range. The photodetector on another hand also limits the imaging range Δz_{max} because of their limited electrical detection bandwidth B, as shown in equation (7).

$$\Delta z_{max} \approx \frac{B}{2} \frac{{\lambda_0}^2}{\Delta\lambda} T_{sweep} \tag{7}$$

Where T_{sweep} is the duration of the sweep, λ_0 and $\Delta\lambda$ are the center wavelength and the bandwidth of the laser, respectively. Therefore, the characteristics of the light source affect the imaging range in OCT. A broader bandwidth leads to higher interference frequencies for the same delay, which can be limited by the detector's capabilities for detection. The choice of light source also influences the depth range in OCT. Shorter wavelengths lead to increased scattering, resulting in reduced penetration depth, as described by Rayleigh scattering ($\sim\lambda^{-4}$).

2.1.3. Axial and lateral resolution

The resolution of an optical OCT setup give a direct idea of the quality of the images that will be acquired, and how detailed it will be. It is one of the major points of OCT. The resolution defines the smallest distance between two adjacent structures that can be differentiated. The axial resolution concerns two structures aligned with the beam direction, how precise in depth it is possible to separate two structures. The lateral resolution, also called transverse resolution, regards alongside structures in the perpendicular direction to the beam. Both resolutions are decoupled from each other in OCT.

The axial resolution is fully defined by the light source used in the imaging setup. Its center wavelength λ_0, its full width half maximum (FWHM) spectrum width $\Delta\lambda$, and the shape of the spectrum are the three-parameter defining it. The following equation depicted the axial resolution Δz for a Gaussian spectrum:

$$\Delta z = \frac{2\ln(2)}{\pi}\frac{{\lambda_0}^2}{\Delta\lambda_{FWHM}} \tag{8}$$

In this thesis, since the laser spectrum used when doing imaging has a top-hat spectrum the following equation is used:

$$\Delta z = 0.60\frac{{\lambda_0}^2}{\Delta\lambda_{FWHM}} \tag{9}$$

Both equations can be calculated back from the coherence function as explained in [40]. Furthermore, it is important to notice that the axial resolution also depends on the refractive index of the material being imaged. When focusing on retinal imaging, where biological tissues are mainly composed of water, the axial resolution calculated with equation (9) should be divided by n = 1.33, the refractive index of water. To be considered as usable for ophthalmic OCT, a light source must provide an axial resolution under 15 μm [41]. Implying a bandwidth above 22 nm for a top-hat swept-source centered at 850 nm.

Regarding the lateral resolution, only the optics used in the setup and the center wavelength λ_0 play a role. The transverse resolution is defined by the focal spot size. It is determined as $2w_0$ (beam diameter), where w_0 represents the beam waist radius. Since in most OCT setups, and in the system used later in this thesis for imaging, all fibers used are single mode (SM), we can approximate the beam to have a pure Gaussian shape. This approximation enables to define Δx as:

$$\Delta x = 2w_0 = \frac{4\lambda_0 f}{\pi d} \tag{10}$$

Where d is the $1/e^2$ beam diameter in front of the objective lens and f is the focal length. In our case, the focusing lens being the human eye's lens f~17 mm [42]. However, in practice, experimental results often deviate from theoretical predictions due to imperfections and non-ideal conditions. To account for this, the calculated lateral resolution must be multiplied by the beam quality factor M^2, which quantifies how much the beam diverges from an ideal Gaussian beam.

In retinal imaging where the sample is curved, it is also interesting to have a relatively long depth of focus d_z:

$$d_z = 2z_R = \frac{\pi\,\Delta x^2}{2\lambda_0} \tag{11}$$

Where z_R is the Rayleigh length. With a long depth of focus, information from the choroid could also be acquired. However, the longer the depth of focus, the larger the transverse resolution.

Methods to reduce aberration introduced by a too high numerical aperture can be used, for instance adaptive optics [43, 44].

The final lateral resolution observed in the acquired image can also be affected by the sampling of the acquisition. Depending on the galvanometer scanner frequency, it is possible to oversample or under sample, further detailed in section 4.

2.1.4. Noise and Sensitivity

The sensitivity S, expressed in dB, defines the smallest still measurable signal coming back from the sample depending on the optical power on the sample P. To be measured, the signal coming back from the sample must be higher than the average noise power at the same depth. The three main source of noise present in an SS-OCT system are σ_{shot}, $\sigma_{receiver}$ and, σ_{RIN}. They contribute to the overall noise level σ_{noise} of the system. These noise sources sum up according to the equation:

$$\sigma_{noise}{}^2 = \sigma_{shot}{}^2 + \sigma_{receiver}{}^2 + \sigma_{RIN}{}^2 \quad (12)$$

σ_{shot} represent the shot noise (or quantum noise) of the SS-OCT system. It arises from the random arrival of photons at the detector, causing fluctuations in signal intensity. When a system is "at shot noise," it means that the noise level is primarily determined by the inherent properties of light, it is a fundamental limit, and further improvement may be challenging. A system is "at shot noise" when the measured sensitivity and the calculated sensitivity, see equation (13) following [45], are equal.

$\sigma_{receiver}$ is introduced by the electronics circuits in the detection part of an OCT system. To reliably detect signals, the receiver noise must be lower than the signal itself. Minimizing receiver noise involves optimizing the design and performance of electronic components, such as amplifiers and detectors, to achieve high SNR.

σ_{RIN}, or relative intensity noise (RIN), originates from fluctuations in the output power of the light source. The RIN is defined as the power noise normalized to its average value. RIN can distort the signal intensity and affect the quality of OCT images, especially in systems with high sensitivity requirements. Minimizing RIN involves ensuring stable and consistent laser output power, typically through advanced laser stabilization techniques and careful system calibration. However, as mentioned earlier, balanced photodetectors are used in SS-OCT systems, which enables cancelling the RIN if the system is at shot noise [46].

One of the main parameters to consider in OCT is its sensitivity. If a sensitivity of 100 dB is achieved, it means that the OCT system can detect reflected signals with a power as low as 10^{-10} relative to the incident power, which corresponds to only a few photons. The sensitivity can be calculated as follows in the case of SS-OCT:

$$S_{dB} = 10 \log\left(\frac{\rho P T}{e}\right) - IL \quad (13)$$

Where ρ is the responsivity of the detector (for silicon detectors approximately 0.3 A/W at 850 nm), T is the duration of one sweep, e is the elementary charge of an electron, and IL corresponds to the loss that the signal reflected by the sample experience before reaching the photodiode.

The sensitivity is highly dependent on the noise of the system. The A-Scan rate for example highly impacts the sensitivity since it reduces the energy at one location on the sample, hence the back reflected photons. The interferometer used to generate the interference can also introduce noise, it also highly impacts the shot noise. With increasing power in the reference arm, the excess noise is also increasing. However, if the power in the reference arm is too low, then the electronic noise dominates. A sweet spot value of reference arm power must be found to reach shot noise, hence the highest sensitivity. In general, if shot noise is reached, the sensitivity should reach a plateau [47], i.e. be constant over a range of reference arm power. Averaging is also used to improve sensitivity; it reduces the speckle and improves SNR.

2.1.5. OCT applications in ophthalmology

Since ancient Egypt in 1550 before Christ, human beings have expressed their interest in the eye, writing about its diseases [48]. The first eye dissection happened later, in Ancient Greek [49]. The eye interest has only been growing and tremendous progress has been realized [21]. Nowadays, most eye practices, diagnosis, and treatments are non-invasive. About 66% of the US's adult population has had or is having corrective eyewear, such as glasses or surgery [50].

2.1.5.1. Structure of the human eye

Vision is possible thanks to communication between the eye and the brain via the optic nerve. Light travels through the eye, is converted into neural signals, and is transmitted to the brain who interprets it as images. An average adult human eye is typically 24 mm long. It takes its shape from the presence of the transparent fluid, the vitreous humor, which maintains constant pressure against the sclera, the white protective outer layer of the eye, as shown in Figure 4 (A).

The front part of the eye regulates the amount of light entering the eye to avoid saturation by closing the iris, the colored part of the eye. The smaller the pupil will be (the black opening at the center of the iris), the less light propagating through it. During darkness, the pupil will be open at its maximum to let more light come in and improve night vision.

Our eyes are capable of sharp vision at different distances. This results from stretching or relaxation of the muscles of the ciliary body which stretch or relax the lens. While the cornea is responsible for the primary refraction of light, the lens fine-tunes this focus to ensure that light is

accurately directed onto the retina. The aqueous humor, the clear fluid between the cornea and lens, contributes minimally to the overall refraction.

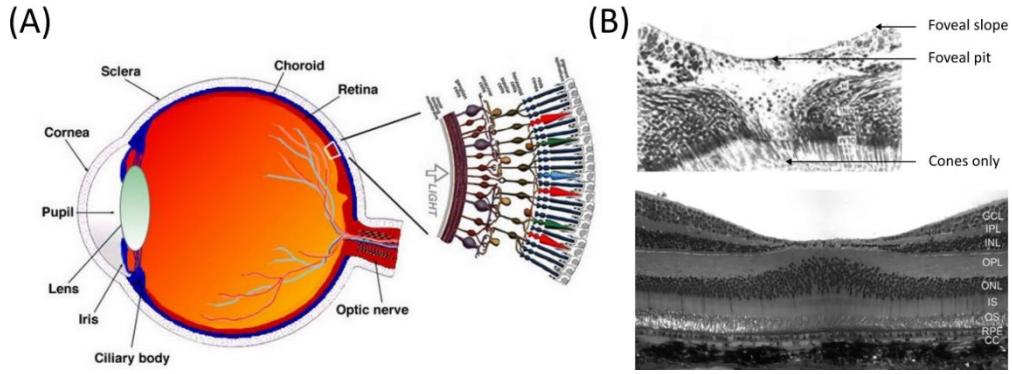

Figure 4. (A) anatomy of the human eye. (B) Cells repartition at the foveal pit of the retina, GCL: ganglion cell layer, IPL: inner plexiform layer, INL: inner nuclear layer, OPL: outer plexiform layer, ONL: outer nuclear layer, IS: inner segment, OS: outer segment, RPE: retinal pigment epithelium, CC: choriocapillaris [51, 52].

The retina is one of the astonishing organs of the entire body having the most active metabolism. It is the most oxygenated organ per unit of size of the whole body. It requires constant high oxygenation throughout the whole life of people due to its incapabilities of storing oxygens [53]. The retina is one of the main keys of the eye. It is 500 µm thick and composed of millions of photoreceptor cells. It converts the light passing through the front part of the eye into neural signals which will travel to the brain via the optic nerve. The photoreceptors are either cones or rods. Cones are sensitive to color while rods are sensitive to the intensity of light. The density of cones increases closer to the foveal pit, which is the center region of the macula. This high density of cells is responsible for our ability to sharpen vision. This area represents a diameter of 200 µm of the retina. The retina also becomes thicker in the macula region due to the increasing number of cones which need more cone bipolar cells for more synaptic interaction with the ganglion cells in the Inner Plexiform Layers (IPL). At the foveal pit, second- and third-order neurons are displaced on the sides to allow the incoming light to strike the cones directly. This displacement creates the foveal slope where the thickness of the retina goes from its maximum to a thinner thickness with almost no neural cells as shown in Figure 4 (B). Regarding the peripheral area of the retina, it is mostly composed of rods which will ease night vision thanks to a wider region being sensitive to light intensity.

Due to the high need for oxygen in the retina, high-density vascularization is also needed. All the blood supply to the eye comes from the ophthalmic artery, which is a branch of the internal carotid artery, as illustrated in Figure 5 (A). The ophthalmic artery supplies 4% of the blood to the retina via the central retinal artery. It enters the retina through the optic disc. Retinal vessels present in the nerve fiber layer branch to capillaries to supply more cell layers. 85% of the blood is directed towards the choroid. This eye layer needs high vascularization to nourish in nutriment the outer layers.

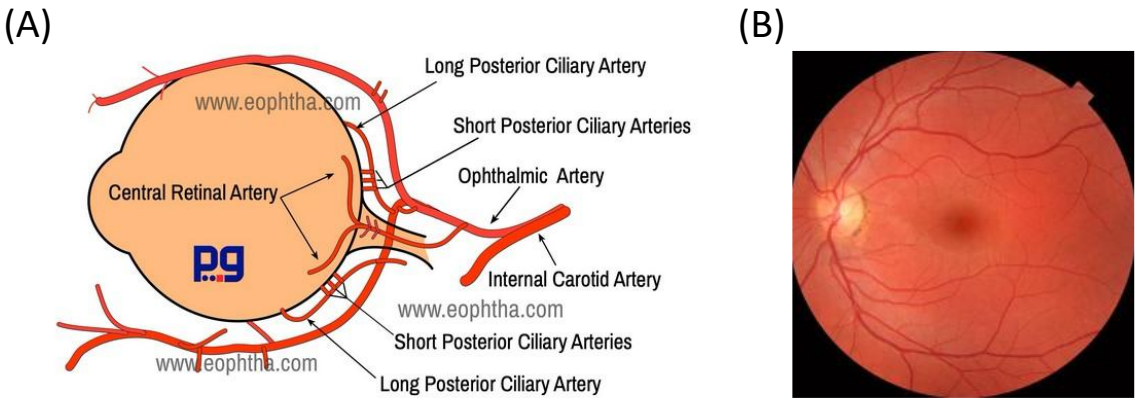

Figure 5. (A) Schematic of the retina vascularization [54], (B) fundus image of the retina and its vascularization [55].

A fundus examination may be carried out to assess the retina's health. It uses a slit lamp emitting white light that will go through the front part of the eye to illuminate the eye's posterior segment. As a result of this technique, blood vessels, as illustrated in Figure 5 (B), the optic disc, the fovea, and the upper retina can be observed. However, this method does not allow information to be received from deeper structures, which could prevent the early diagnosis of certain diseases. In this way, cross-sectional imaging techniques like OCT are of interest. This will be shown and explained further in the next section.

In addition to its above-mentioned capabilities, the eye possesses a subtle, yet crucial function known as micro saccades. These imperceptible, involuntary eye movements persist ceaselessly, even when an individual fixates on a single point. This perpetual motion ensures a steady influx of new visual information, preventing the onset of sensory adaptation – a process that allows our senses to gradually tune out unchanging stimuli. The next section will demonstrate the importance of considering these movements when performing OCT.

2.1.5.2. Retinal imaging OCT

The interest in the study of the retina goes back 100 years. Its first human *in-vivo* appreciation has been possible in 1851. Hermann von Helmholtz invented this year the ancestor of the ophthalmoscope. He was able to predict certain pathologies by observing the retina back then [56]. More than 100 years after his invention, A.F. Fercher, in 1988, made a huge breakthrough when he managed to measure the length of the eye, using partial coherence interferometry [57]. A few years later, in 1990, the first A-Scan was acquired, quickly followed by the first ex-vivo cross-sectional images on the retina, done by James G. Fujimoto's group at the Massachusetts Institute of Technology in 1991 [21]. The first in-vivo retinal OCT was acquired 2 years later [58], and 3 more years later the first clinical ophthalmology OCT was delivered [59]. The OCT market is nowadays valued at 1.47 billion US dollars, with ~60 % dedicated to ophthalmology. In 2017, 25 years after the invention of OCT, about 50,000 OCT systems were installed and operating.

Figure 6 shows the evolution from the first retinal OCT image acquired in 1991 with a TD-OCT setup (A) [21], to the first SD-OCT *in-vivo* retinal image of 2002 (B) [60], and one acquired in 2013 with SS-OCT (C) [8]. These three different types of OCT are detailed in section 2.1.1. The sensitivity has been improved by 19 dB between (A) and (C) enabling the distinction of layers of the retina. The acquisition speed has also experienced a huge increase. In fact, due to their slightly different techniques, these three OCT methods enable different axial rate capabilities. SS-OCT achieves a remarkable acquisition time of 0.56 ms for a single B-Scan, as depicted in Figure 6 (C). This translates to an impressive 3.35 MHz axial scans per second with 1900 A-Scans per B-frames. This image presents the average of 24 B-frames, each separated by 1.3 µm. In contrast, the SD-OCT B-Scan shown in (B) requires a significantly longer 20-second acquisition time and offers a narrower field of view. Axial resolution has also seen a major improvement due to the improvement of technologies, especially light sources. The axial resolution achieved by (C) is 10 µm. Table 1 sums up all the main characteristics of each image presented in this sub-section.

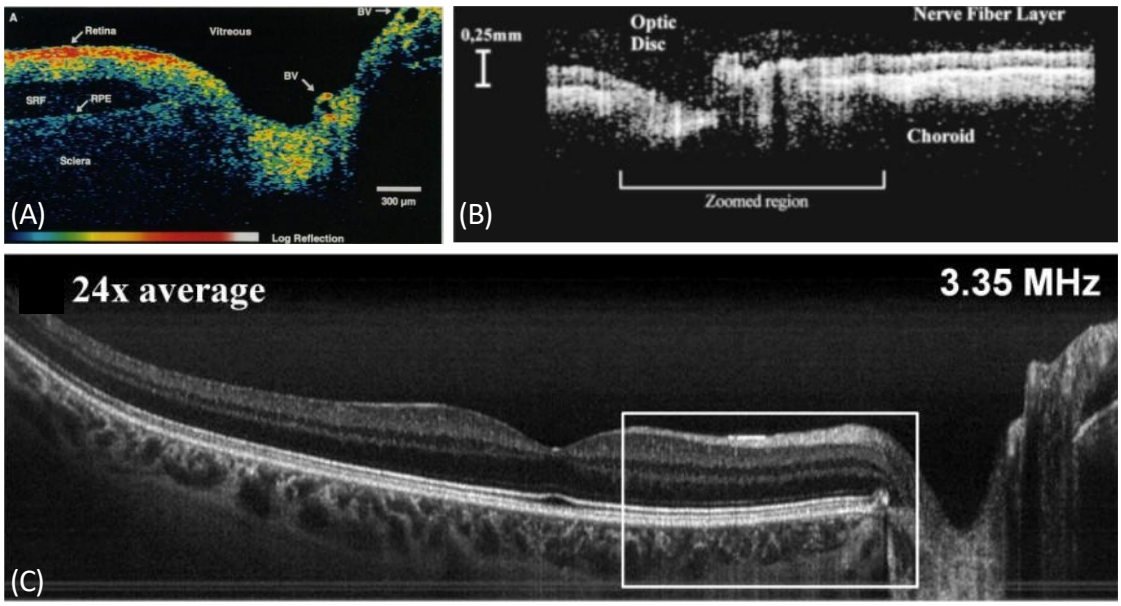

Figure 6. (A) First ex-vivo retinal TD-OCT imaging [21], (B) First in-vivo retinal SD-OCT [60], (C) in-vivo retinal SS-OCT acquired at 3.35 MHz [8].

Table 1. Comparative table summarizing data from the illustrated section.

Images	Year	Technology	Wavelength	A-Scan rate	Sensitivity	Axial resolution
Figure 6 (A)	1991	TD-OCT	830 nm	1 Hz	70 dB	15 µm
Figure 6 (B)	2002	SD-OCT	810 nm	25 Hz	71 dB	14 µm
Figure 6 (C)	2013	SS-OCT	1060 nm	3.35 MHz	89 dB	10 µm
Figure 7 (A)	2022	SS-OCT	1060 nm	1.68 MHz	95 dB	9 µm
Figure 7 (B)	2022	PS-OCT	860 nm	70 kHz	-	4 µm

Further advances in the world of OCT are very promising for retinal imaging. Particularly the advances in angiography (OCTA). They enable better visualization of the blood vessels and capillaries present in the retina and the choroid, as shown in Figure 7 (A). This is enabled by the

acquisition of the same position in the images at a different time which provides, after software processing, more information on the movement of blood cells. A fair number of vision issues are due to vascular problems [61], which show the importance of this processing technique. Another technology that uses the polarization of light can be applied to retinal OCT. Acquiring the fast and slow axis of the light source in different channels enables the acquisition of different contrasts in the image. In the retina, since the different layers do not have the same properties and birefringence, more information on their health can be seen as shown in Figure 7 (B-C).

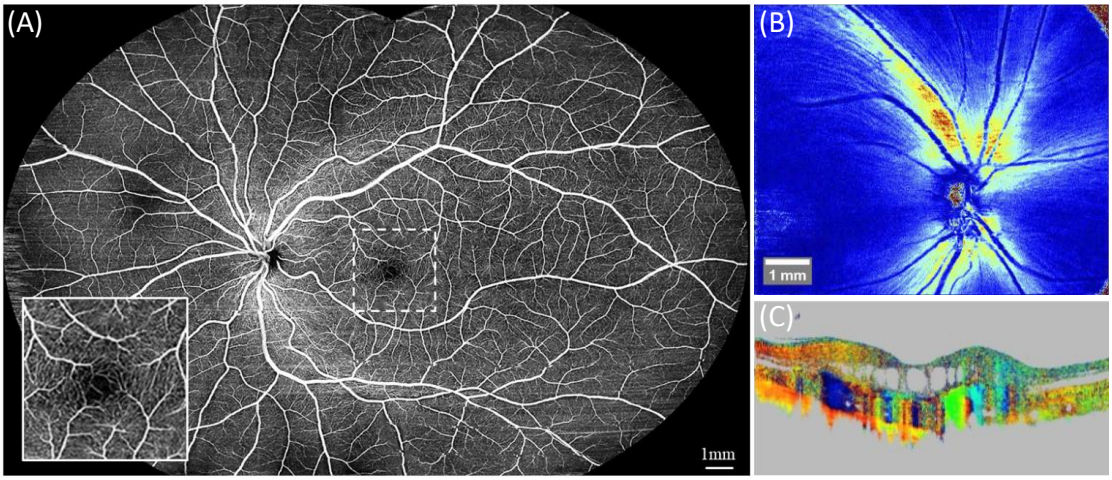

Figure 7. (A) Retinal widefield OCTA acquired at 1.64 MHz with a 1060 nm FDML laser [62], (B) en-face view of a retina imaged by PS-OCT [63], (C) Cross-sectional view of a retina imaged by PS-OCT [64].

Most retinal OCT devices on the market are currently SD-OCT systems centered at 850 nm. They show sensitivity higher than 100 dB, axial resolution of about 5 µm, and repetition rate of 100 kHz. This slow axial scan rate can create problems regarding the microsaccades of the eyes. Hardware and software solutions can correct eye motion, as stated in [65]. This need can be avoided by scanning faster using SS-OCT. With their sweep repetition rate able to reach 3.35 MHz without impacting the sensitivity, all systems will be less subject to eye movement and microsaccades.

Another specificity of ophthalmic OCT setups lies in the pivot point's position. To be able to scan widefield areas without being limited by the opening of the iris, the optics are designed so that all rays are deflected at a specific point, called pivot point. The laser beam hits the scanning mirror being collimated. A 4-F optic is then used to focus the light on the retina while having the pivot point around the lens as shown in Figure 8. The optics are designed in a way that the pivot point's position can be adapted depending on the field of view aimed for. A beam-splitter, or a dichroic mirror, is usually used between the relay lens and the objective lens to enable our eyes to see through, facilitating the fixation on a viewpoint and alignment of the eye.

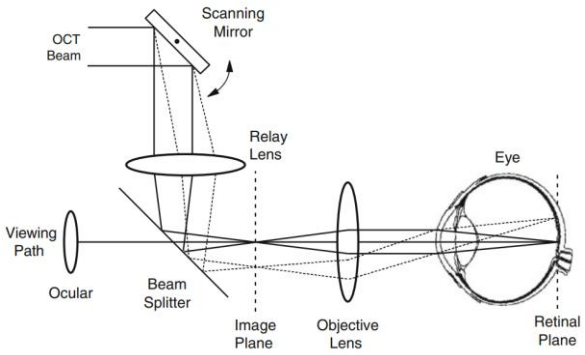

Figure 8. Schematic of an optical setup used for retinal OCT imaging [66].

2.2. Swept light sources

This chapter gives a general introduction to laser technology, starting from a single photon, going towards a laser beam. A more detailed description of wavelength tunable lasers used for OCT follows. Firstly, different technologies of emitters are presented, vertical-cavity surface-emitting lasers (VCSELs), vertical external-cavity surface-emitting lasers (VECSELs), and membrane external-cavity surface-emitting lasers (MECSELs). And secondly, other technologies enabling tuning modalities by either using mechanical filters, such as polygon scanners, or by using optical properties like time stretching.

2.2.1. General laser theory

Before they were even named “photon” by Gilbert N. Lewis in 1926, these elementary particles were studied for several years. Albert Einstein theorized their behavior in 1905 in “Über einen die Erzeugung und Verwandlung des Lichtes betreffenden heuristischen Gesichtspunkt” ("On a Heuristic Viewpoint Concerning the Production and Transformation of Light") [67]. These fundamental quantum particles of light are defined by their energy, momentum, and polarization. They can be emitted from two different quantum mechanics, *spontaneous emission*, and *stimulated emission*. In both cases, their emission happens when an electron of an excited atom or molecule is transitioning from an upper energy level to a lower one as shown in Figure 9.

Figure 9 also shows the pumping procedure of quantum mechanisms. Before obtaining photons, electrons of atoms or molecules must be in an excited state. To reach the conduction band, the incoming energy must be higher than the band gap. If so, the energy is absorbed by the electron, and it transitions to the upper energy level. Once excited, either spontaneous or stimulated emission will occur. Several pumping processes can be used to lift the electron.

Light becomes a laser when photons are emitted by stimulated emission. In this first case, a photon at a specific frequency will irradiate the excited atom or molecule which will decay to a lower-lying level and emit an identical photon. By generating in-phase and coherent new photons from

the originals, a directional laser beam is created at this specific frequency. This is where the acronym LASER takes its name: “Light Amplification by Stimulated Emission of Radiation”.

Spontaneous emission is the second type of photon emission. It occurs without any external influence. The emitted light has its frequency and wavelength defined by the difference of energy between both states E1 and E2, but the photons’ phase and direction are random. The emitting frequency of two photons spontaneously emitted from the same transition band can still vary. Energy levels not being infinitely sharp create uncertainty which will broaden the linewidth Δν of the spectral line, hence the ~ in equation (14).

$$\nu_{12} \sim \frac{\Delta E_{12}}{h} \tag{14}$$

h being the Planck’s constant, ν the frequency and ΔE the energy difference between both bands 1 and 2.

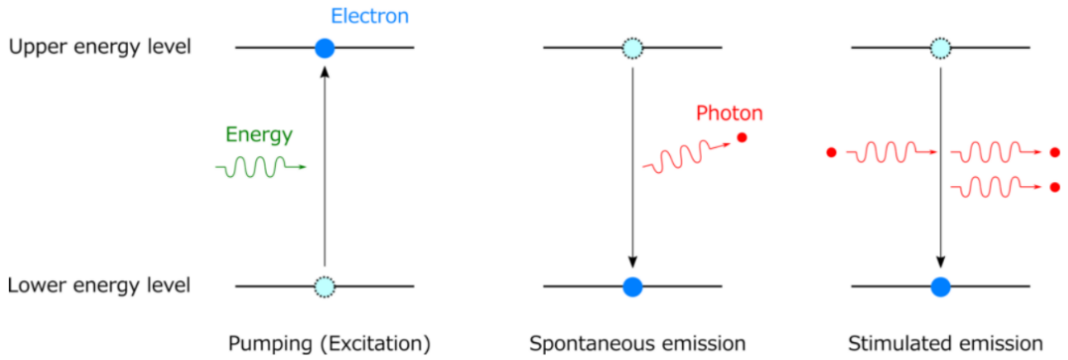

Figure 9. Illustration of the excitation of an electron (pumping) from one lower band to an upper energy level and representation of both processus for photons emission, spontaneous emission and stimulated emission [68].

The three quantum mechanisms mentioned above are essential for the generation of laser light, including amplified spontaneous emission (ASE) observed in devices such as semiconductor optical amplifiers (SOA). The pumping process involves exciting atoms or molecules within the gain medium, which subsequently emit photons through spontaneous emission. These photons can then undergo stimulated emission, where they create additional photons with identical properties, thus amplifying the light. While ASE can occur in certain laser systems, the primary objective of stimulated emission is to produce coherent laser light rather than ASE. Pumping has a key role here. It enables population inversion, by bringing enough energy to obtain a greater quantity of atoms in the conduction band than in the valance one. Population inversion is necessary to have a domination of the emission process.

The sequence of emission and absorption is enabled by the three main components of a laser. The *active laser medium* determines the laser properties, notably the emission range. Energy levels are created in a way that atoms emit in a specific band of wavelength. The second main component is the *pumping mechanism*. As mentioned before, active medium can be electronically pump. It

can also be pumped with light, like in Ytterbium fiber. The laser *resonator* is the last main component. In the simplest case it consists of 2 highly reflective mirrors. The first photons spontaneously emitted will propagate and be reflected in the resonators, only the ones having the right direction and frequency will build up and engage stimulated emission. The laser then has coherent photons. In the case of FDML laser, the resonator is composed of a long fiber cavity and fiber components that connect the output of SOA to its input.

The first functional laser was introduced in 1960 by Theodore Maiman, 43 years after its theoretical demonstration by Albert Einstein in "Zur Quantentheorie der Strahlung" ("On the Quantum Theory of Radiation") [69]. This laser marked the pioneering development among the diverse range of laser types that now exist. From laser welding to fluorescence microscopy passing through OCT, they all demonstrate different characteristics depending on the need. They can have a continuous wave (CW) output or be pulsed. They can be for example extremely coherent, have high power, or be wavelength tunable [70].

Regarding OCT, power above 50 mW is not necessary since it is generally intended for medical imaging. One main requirement is constant power over time. Lasers used in this field are CW lasers. The population inversion in these lasers is kept active as long as the laser is on. In this thesis, as mentioned previously, the focus is on SS-OCT where wavelength-tunable lasers are used. Several of them are presented in the following section.

2.2.2. Swept-sources properties

Wavelength-tunable lasers are a type of laser that emits light at different frequencies. They can be tuned through optical or mechanical means within a specified tuning range. Apart from the resonator, the other main component is the laser gain medium. It enables the introduction of an electric field in the laser and its amplifications.

Tunable lasers find applications in fields like spectroscopy, telecommunications, or OCT. Specifically, in the realm of SS-OCT, the focus is on a specialized type of tunable laser known as swept-sources. They are designed for rapid continuous tuning. In this section, the main properties defining swept-sources are presented.

For a swept-source to be deemed effective for *in-vivo* OCT imaging, it must demonstrate a range of key performances to facilitate high quality image of human tissue. The essential attributes considered in the construction of a swept-source are outlined below. To illustrate, the desired performance of the forthcoming developed laser are used.

- **Center wavelength: λ_0 (nm)**

The center wavelength is chosen depending on the desired application. For instance, in the scenario of imaging the human retina, where approximately 2 cm of vitreous humor – similar in properties to water – intervenes between the front and back of the eyes, it becomes imperative to

factor in water absorption. An ideal center wavelength according to Figure 10, would be in the visible spectrum due to minimum water absorption, which would allow high-quality imaging. However, these wavelengths are highly scattered which results in a shallow penetration depth. Most of the SS-OCT ophthalmic systems are nowadays using 1060 nm swept-source due to a local minimum in water absorption. However, their bandwidth is limited to about 140 nm due to an increase of water absorption around the local minimum, as shown in Figure 10. A trade-off between water absorption and penetration depth is the wavelength of 850 nm.

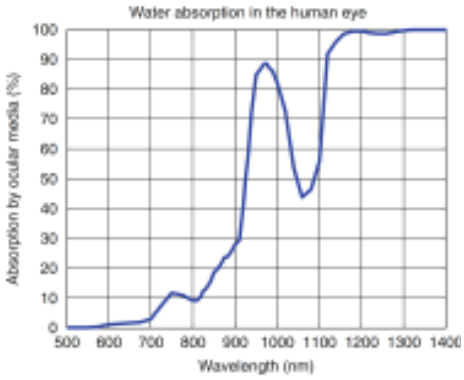

Figure 10. Water absorption in the human eye as a function of the wavelength [59].

- **Bandwidth: Δλ (nm)**

The bandwidth or tuning range is defined by the output spectrum of the laser. How far in nanometer centered around λ_0 the laser is still lasing at -3 dB from the highest amplitude. The wider the spectral bandwidth, the finer the axial resolution (see equation (9)). If an axial resolution below 10 µm is desired with $\lambda_0 = 850$ nm, a minimum bandwidth of 40 nm for a top-hat spectrum is necessary. Nevertheless, a wide bandwidth reduces the dynamic range of the OCT due to the limitation of the detection bandwidth of the photodetector, which is not desirable. Depending on the application, the trade-off between both parameters can be adjusted if higher axial resolution or longer depth penetration is required [71].

- **Instantaneous linewidth: δλ (nm)**

The instantaneous linewidth of a laser is one of its most important characteristics. It defines the spectral width of the frequency emitted by a laser at a given time, instantaneously. The narrower the linewidth the longer the coherence length z_c, they are related by the following equation:

$$z_c \approx 0.44 \frac{{\lambda_0}^2}{\delta\lambda} \tag{15}$$

The linewidth will also have a direct impact on the axial resolution of the system. A narrow linewidth leads to sharper interference frequency resolution, meaning sharper depth resolution, hence axial resolution. For a swept-source intended to be used in OCT, a linewidth $\delta\lambda$ < 100 pm for λ_0 = 850 nm is preferred, which would yield to z_c = 3.2 mm.

- **Tuning curve**

The tuning curve shows how wavelengths are being emitted over time, one after another. In an ideal swept-source, the tuning curve of the wavenumber over time is linear. Depending on the type of tuning modalities used in the laser, the tuning curve might not be linear, it will then have to be corrected using a calibration method, two are presented in 2.1.2. In the case of a laser using a Fabry-Pérot filter, the sweep must be calibrated since the tuning curve follows a sinewave. It also has two directions, sweeping from short to long wavelength called the forward sweep, followed by the backward sweep, sweeping from long to short wavelength. Both sweeps, depending on their similarity level, might require independent calibration.

- **Sweep repetition rate: f (Hz)**

The sweep repetition rate determines the time it takes for the wavelength-selective element in the cavity to transmit from the shortest to the longest wavelength or vice versa. It is also defining how fast OCT images can be acquired. The time it takes to acquire an A-Scan refers to the laser sweep rate. Hence, the higher the sweep repetition rate, the faster an OCT image can be acquired and hence the less it is sensitive to sample motion (e.g. eye motion). Several factors can limit the sweep speed. In case of lasers with mechanical tunability, it is imperative to align the resonator frequency closely with the resonance frequency of the tunable mechanism. Resonance occurs when the driving frequency of a system matches its natural frequency, which results in maximal amplitude. The natural frequency f of an oscillating object, such as a mechanical system, is given by the formula [72]:

$$f = \frac{1}{2\pi}\sqrt{\frac{k}{M}} \tag{16}$$

with k the spring constant of the mechanism. This resonance frequency is directly linked to the mass M of the tuning element, rendering it a critical factor in performance. In the case of employing a mirror within a filter, the mass of the mirror holds a significant role in defining the resonance frequency. More factors impact the resonance frequency, like the quality of the micro-electromechanical systems (MEMS) in VCSELs (elaborated upon in the subsequent section) or their pull-in voltage, which won't be detailed in this thesis. In the case of FDML laser, the fundamental sweep repetition rate is generally around 410 kHz and can be increased further using optical buffering, see 2.3.

- **Output power: P (mW)**

Like λ_0, the desired output power P is defined depending on the potential future application. Standards must be respected to protect the sample/subject from hazards originating from the light source. Also, the power applicable on sample depends on the wavelength used, if the sample will be more subject to absorb this wavelength, the limit will be lower to avoid heating of the sample

and destruction. For retinal imaging at 850 nm, the optical power applicable at the cornea is 0.720 mW for a static beam according to standard [73, 74].

- **Intensity and phase noise**

Depending on the laser source, several noises can arise. Regarding swept-sources, intensity noise, and phase noise are the main noises to be considered. The intensity noise defines the noise of the transient optical power output. The RIN can be used to quantify the intensity noise by using the normalization of its average value. It can be defined, with P the optical output power, as [59]:

$$RIN = \frac{< \Delta P^2 >}{P^2} \, [Hz^{-1}] \tag{17}$$

The phase noise defines how stable the output phase of the laser is overtime. How similar the phase of one sweep is to the following. It can be quantified by the normalized average of the phase drift in radians over a certain number of sweeps.

The intensity and phase noise mainly come from quantum noise. It can also arise from what can be called technical noise. If the laser is subject to temperature instability, or for laser based on mechanical resonator (detailed in the following sub-section), vibration can introduce intensity noise. The intensity noise can be reduced by using dual-balancing which cancels out common-mode noise, all non-coherent light, and all DC components as mentioned in 2.1.4. This is one of the strengths of SS-OCT. Phase noise, on the other hand, cannot be improved by dual balancing. It requires improved phase-locking in the laser, and better engineering.

- **Coherence length**

Each electromagnetic wave can be defined by its amplitude, frequency, and phase. The term coherence is related to the phase of a combination of waves. It expresses the tendency of all waves constituting the resulting one to maintain a constant phase difference between them. The phase can be analyzed over time and space. Spatial coherence, which won't be detailed here, looks at the phase of the wave in a plane perpendicular to the direction of the beam. It studies the differences in the wavefront of the wave across different points in space. The directionality of laser beams is mainly defined by spatial coherence [75, 76]. Temporal (longitudinal) coherence involves analyzing a wave's phase over time, determining how long the wave maintains the same phase. It can also be measured over a distance along the wave's direction of travel, known as coherence length L_{coh}, and described as:

$$L_{coh} = \frac{c}{\Delta \nu} \approx \frac{{\lambda_0}^2}{n \, \Delta \lambda} \tag{18}$$

where c is the speed of light and $\Delta \nu$ the FWHM linewidth of the light source. Interferometers, such as Michelson or Mach-Zehnder interferometers (MZI), can be used to measure the coherence length of a source. An interference pattern is generated, and the coherence length can be measured by increasing the delay between both arms.

One of the factors influencing the coherence length of lasers is their bandwidth. When a source has a large bandwidth, it emits different frequencies. When two frequencies travel, their phase relationship changes over time and will degrade the contrast with which the frequency of the interference pattern can be distinguished. When the contrast drops by 3 dB (50%) it defines the coherence length of the source. Another common term used to define the coherence length is 'roll-off'. However, it is usually measured at a decrease of 6 dB and not 3 dB.

As bandwidth increases, coherence decreases, necessitating a tradeoff to achieve optimal resolution and penetration depth. Yet, for retinal applications, deep penetration is less critical due to the thinness of the retina.

In summary, the ideal swept-source for this study exhibits a center wavelength of 850 nm, a top-hat bandwidth of 40 nm, and an instantaneous linewidth narrower than 100 pm, with a preference for higher repetition rates and a linear tuning curve. Moreover, it should minimize intensity and phase noise while delivering a power of 0.720 mW to the sample.

2.2.3. Existing swept-sources

The wavelength tuning techniques of wavelength swept laser can be separated into three, semiconductors, optomechanical filters, and optical tuning.

As far as semiconductors are concerned, they can be grouped into two classes. Edge-emitting lasers where the laser light propagates in the plane of the wafer surface, and surface-emitting lasers, where the light propagates perpendicularly to the wafer.

Regarding surface-emitting lasers, their tuning modalities are mostly inside the laser structure. For **VCSELs**, for instance, the gain material is directly positioned between two high reflective mirrors, as shown in Figure 11. Between both mirrors standing waves build up and give the lasing wavelength. If the distance between both mirrors is changed, the standing wave's frequency changes, and a sweep is created, hence the swept laser. It is possible to tune VCSELs by modulating the current which will change the temperature of the device and enable the tunability. However, these tunings are limited in bandwidth. Numerous VCSELs are nowadays working along with MEMS. The MEMS can be a distributed Bragg reflector (DBR) mirror or for instance, high contrast gratings [77], which are lighter. This implies a difference in the resonance frequency, which depends on the mass of the mirror, as explained in the previous section. **MEMS-VCSELs** can then be tuned electrostatically by changing the voltage between the top mirror and the electrodes below, which will also have an impact on the sweep speed. Some are also optically pumped as shown in Figure 11 B [78].

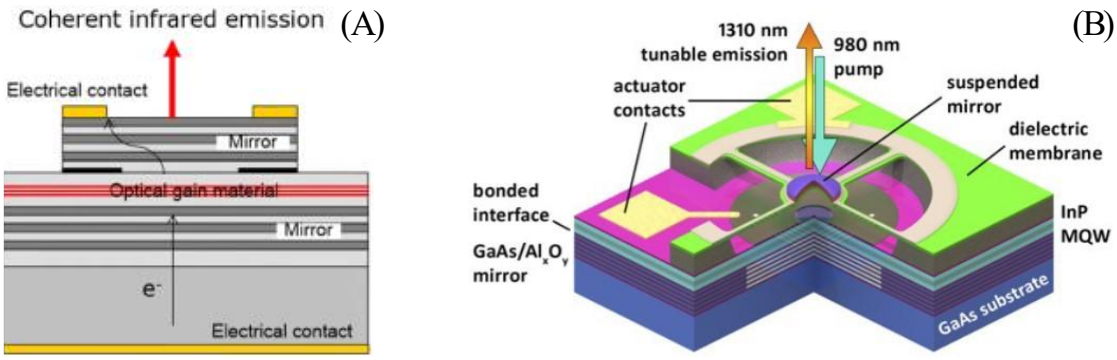

Figure 11. (A) Standard electrical pumped VCSEL. The optical gain material is positioned between two high reflective mirrors, a current is transmitted from the yellow electrode at the bottom to the top one to enable tunability [79]. (B) Optically pumped MEMS-VCSEL. A suspended mirror is placed a few micrometers above the below gain medium. A 980 nm laser light is used to pump the gain medium and enable the emission around 1310 nm. The MEMS enables the tuning electrostatically [78].

Due to the thin gain medium used in VCSELs, around 20 nm thick, a material with a lot of amplification is needed to reach a certain amount of gain. However, the center wavelength and the bandwidth must be considered when choosing the laser medium. Each decision includes some tradeoffs. Free spectral range (FSR), and tuning efficiency is favored with thinner gain, however, thicker semiconductors improve thermal dissipation. VCSELs are well known for their high coherence length, [80] shows no roll-off over 5 cm. This is due to their very small cavity. Also, for the same reason, wide bandwidth and high speed are hard to reach together. Only the Doppler shift makes it possible [81]. It dynamically adjusts each wavelength to consistently align with the resonant frequency of the resonator.

The mirror on top of the gain medium can also be placed outside the laser structure, at about 1 cm from the gain medium as shown in Figure 12 (A). These lasers are called vertical external-cavity surface-emitting lasers: **VECSELs**. The purpose of placing the output mirror further away enables to have more control over the laser beam profile while increasing the output power [82]. These types of lasers are optically pumped [82]. An issue with VECSELS is the temperature cooling which is limited by the thermal conductivity of the DBR mirror placed under the active region [83, 84]. A heat spreader having good thermal conductivity (SiC, Diamond, sapphire, …) must be placed on top of the active region to enable better cooling [85].

To counteract this thermal issue, another type of surface-emitting laser has been developed. The active region is placed between two heat spreaders, while two mirrors are strategically positioned on either side, distanced from the active region to create the laser. They are called **MECSELS**, shown in Figure 12 (B). Like VECSELs, they are optically pumped, however, in this case, they can also be pumped from both sides [86, 87]. Other advantages of these devices are less strain issues and new wavelength region reachable since no DBR is needed. Some have been recently created in the 1770 nm range [88].

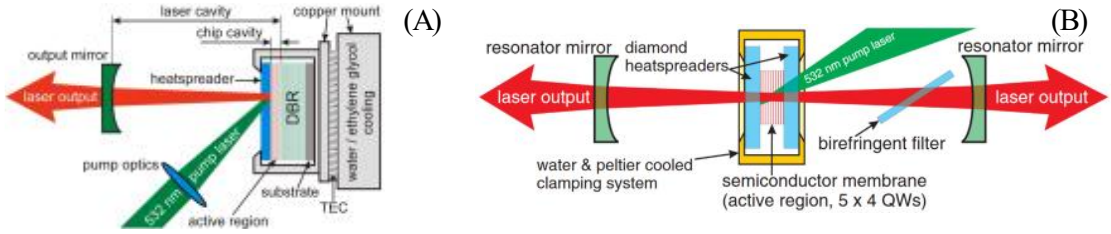

Figure 12. (A) Optically pumped VECSEL. The gain medium is pumped with a 532 nm pump laser. The laser beam is reflected between a DBR and an output mirror placed 1 cm away from the active region [89]. (B) Optically pumped MECSEL. The semiconductor membrane is placed between two resonator mirrors reflecting the beam back and forth. A 532 nm pump laser is used as pumping light [86].

All these semiconductors will emit in different wavelength ranges, depending on the gain materials used. Their future application will also impact the choice of the materials if high power is needed, or rather wide bandwidth. As shown in Figure 13, Gallium-Arsenide (GaAs) gives more amplification gain in the range of 1060 nm wavelength for example.

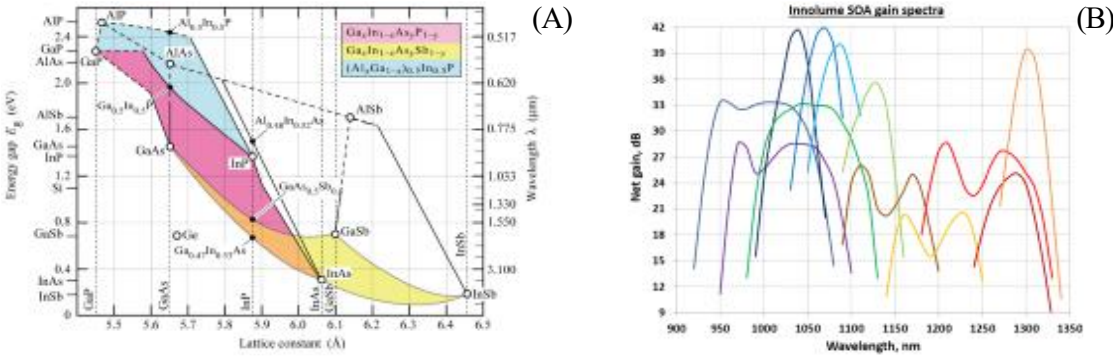

Figure 13. (A) Lattice constant versus energy gap and wavelength for several semiconductors [90], (B) quantum wale/quantum dot GaAs semiconductor optical amplifier based [91].

Tunability can also be achieved by using mechanical filters. These types of lasers use SOA, described in more detail in section 2.3.3, which can emit a broad spectrum of wavelengths around a specific wavelength (> 50 nm around 850 nm from Superlum diodes Ltd., > 70 nm around 1060 nm and > 80 nm around 1300 nm from Thorlabs GmbH.). By filtering each wavelength of the emission band one after the other, a sweep can be created. The two main types of mechanical filters used for filtering are coarsely presented hereunder. They can be used in either long or short cavities.

- **Grating-based tunable filters** relies on diffraction gratings, named for their ability to spread an incoming light across its entire spectrum. This property makes them particularly effective in filtering applications. When an incoming wave interacts with a diffraction grating, its amplitude and phase will create interference in the backscattered wave. They came in various forms, they can be transmissive or reflective and be made of blaze angles or grooves. The more repeating patterns by millimeters the grating has, the sharper the wavelength selection, hence the linewidth. They are defined mathematically by the formula $a \cdot \sin(\theta_m) = m \cdot \lambda$ where a represents the grating period, θ_m the diffraction angle for the m^{th} order, and λ denotes the wavelength. Once all spectral components of

the incoming light have been dispersed, rotating elements can then be employed to select a specific wavelength and sweep over all of them. For instance:

- Polygon scanners: they consist of a multi-faceted, highly reflective mirror mounted on a rotating spindle driven by a motor. They can spin up to 60,000 revolutions per minute. They are generally used in a 4f-optics configuration to obtain the beam reflection from the grating directly onto the scanner, Figure 14 (A) [92, 93]. Overall, polygon scanners are interesting because of their rotating speed, and sweep rate of around 40 kHz, but might introduce noise due to their mechanical concept.
- Galvanometer scanners: in this case, the grating is mounted on a resonant scanner, Figure 14 (B). The backscattered light from the grating is focused on a mirror which redirects it back towards its point of origin. As the grating angle changes (following a sinusoidal wave), wavelength selection happens. In this case, a sweep rate of 16 kHz is achieved [26].

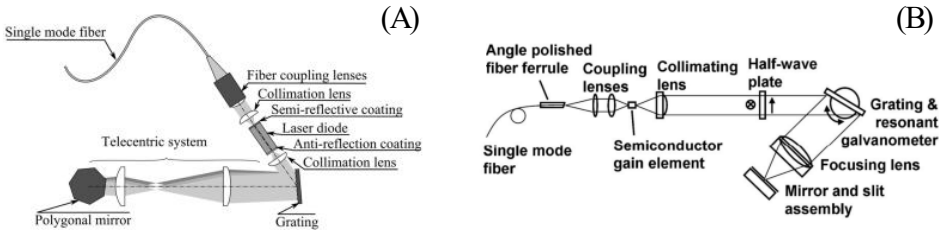

Figure 14. Grating-based mechanical tunable filter using (A) a polygon scanners [93] or (B) resonant galvanometer scanners [26].

- **Fabry-Pérot filter**: the basic mechanism of these filters is to face two high reflective mirrors separated by a micrometer gap. Constructive and destructive interferences happen between these two surfaces whether waves are in phase or not. Due to the high reflectivity of the surfaces, only the high intensity reinforced wavelength that has interfered constructively will pass through. If the gap between both plane surfaces is changed following a specific pattern, a sinewave for instance, the filter is made tunable and enables the sweep creation. These filters can be commercially available with a sweep frequency of 2 x 170 kHz (Lambdaquest, Inc.). Fabry-Pérot filters are attractive for their narrow linewidth and for their simple and robust design. However, like polygon scanners, they might be sensitive to the mechanical mechanism which could introduce vibration. They are also temperature sensitive, and their manufacturing process is challenging mainly because of the alignment process. FDML lasers use home-made FFP-TF as tunable elements. A sweep frequency of ~2 x 410 kHz is achieved [31]. A more detailed description of Fabry-Pérot filters is given in chapter 2.3.2.

To mitigate the introduction of noise from mechanical components, and be less temperature sensitive, it is possible to achieve wavelength sweeping solely through the utilization of light. These lasers are called Akinetic. There are three akinetic types of lasers:

- **Time-stretch**: the idea here is to stretch a very short wideband pulse of light using a dispersive element, like a long fiber delay line or a chirped fiber Bragg grating as shown in Figure 15 (A). The pulse used can be emitted from a supercontinuum source [94, 95] or from a broadband mode-locked laser [96]. This technique can encounter issues like low power since the pulse is stretched a lot, or low performances regarding their point spread function due to several kilometers of fiber introduced in the cavity. Moreover, when using a supercontinuum source, the inherent noise of the source can further degrade performance. However, this technique is not limited by any mechanical component and have showed repetition rates of 400 MHz using optical buffering [97].
- **Stretched pulse mode locking**: In this case, an optical amplifier emits ASE, which is then transformed into a pulse using an intensity modulator. Subsequently, the pulse is stretched through a dispersive element. To achieve mode-locking, the stretched pulse must undergo a reverse dispersion process. Maintaining equal negative and positive dispersion is crucial to prevent any loss within the sweeping wavelength range. To achieve this balance, a chirped Fiber Bragg Grating (cFBG) can be employed in both directions, as illustrated in Figure 15 (B) [98-100].
- **Dispersion tuning mode locking**: this last tunable laser presented in this section is made possible by modulating the frequency in the cavity [101-103]. The ASE emission from an SOA or from Ytterbium doped fiber (Figure 15 (C)), is stretched via a dispersive element. The long pulse will then be chopped depending on the frequency of the modulator to select in each round trip one unique wavelength. By changing the modulation frequency, the laser becomes tunable and one wavelength after each other will go through, which is creating the sweep.

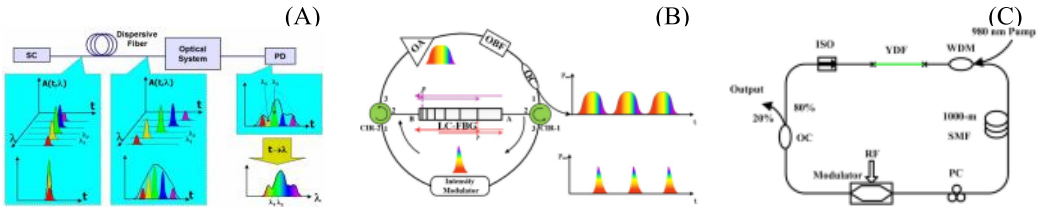

Figure 15. Various akinetic lasers. (A) Time-stretch, a supercontinuum source (SC) emits a pulse which is then broaden by dispersive fiber [95]. (B) Stretched pulse mode-locking, uses an intensity modulator to pulse ASE from the optical amplifier (OA), which is then stretched to create the sweep via a linearly chirped fiber Bragg grating (LC-FBG). It is recompressed via the same LC-FBG afterwards to achieve mode-locking [100]. OBF: optical bandpass filter. (C) Dispersion tuning mode locking, Ytterbium doped fiber (YDF) emits ASE which is then stretched by 1000 m of single mode fiber (SMF). A modulator chopped this long pulse to select one unique wavelength per round trip, creating the sweep at the output of the laser [104].

As demonstrated in the preceding two akinetic lasers, mode locking plays a crucial role in the lasers' functionality. In the absence of mode locking, these swept lasers are susceptible to higher levels of loss and noise. While there are various methods to achieve mode locking, they all share the common objective of achieving optimum operation for each of their applications. The subsequent section will delve into the theory of mode locking.

2.2.4. Mode locking

The term mode locking combines several methods to generate picosecond or femtosecond pulses, also called ultra-short pulses. Three types of mode-locking are possible: active mode-locking, where the subject has a hand on the system, passive mode-locking, where the system is modulating itself, and the last one is hybrid mode-locking, where active and passive mode-locking are used in parallel.

These techniques are based on a resonator composed of a gain medium placed between two mirrors. One mirror can be a saturable absorber mirror and the second an output coupler mirror. Due to this configuration several longitudinal modes, $m \in \mathbb{R}$, are active in the cavity at the same time, all being standing waves having a frequency υ, defined as follow [105]:

$$\upsilon_m = \frac{mc_0}{2Ln} \tag{19}$$

L being the length of the cavity, n the refractive index and c_0 the speed of light. All modes propagating in the cavity will interfere with each other constructively or destructively. To obtain short pulses from all these longitudinal modes, specific care of the phase of each mode should be given. If they all have uncorrelated phases, all photons from different phases will interfere resulting in a random amplitude interference pattern. To achieve high amplitude pulses, the phase of each mode must be correlated and reach all at the same time constructive interference. Repetitive constructive interference, i.e. short pulses, would then happen over time, with a period of t_{RT}, the round-trip time in the cavity. Each mode is defined by the length of the cavity, as described above, and the spectral bandwidth of the active medium. The wider the gain medium, the more modes are present in the cavity. The higher the number of modes in the cavity, the narrower the peak of the pulse in time. The following formula describes the FWHM of the pulse τ_p:

$$\tau_p = \frac{1}{N\Delta\nu} \tag{20}$$

If N, the number of modes, increases in the cavity, the smaller τ_p becomes. However, it is important to note here that the time-bandwidth product limits it.

For all modes to oscillate in a synchronized phase, all types of mode locking use the same principle. The goal is to modulate periodically the resonator, its amplitude or frequency, with a frequency equal to the difference of frequency between two neighboring longitudinal modes noted, $\Delta\omega_q$.

In active mode-locking, if a longitudinal mode of frequency ω_0 is modulated at $\Delta\omega_q$, the frequency separating two neighboring modes, additional radiations component appears at

$$\omega_0 \pm n\,\Delta\omega_q \tag{21}$$

which corresponds to all neighboring modes, causing coupling of the modes. Hence, there is a correlation between the phase of each mode. To modulate the modes, the refractive index of the medium is modulated. This modulation can be performed, for instance, using an acousto-optic modulator. A piezoelectric transducer can be used to generate acoustic waves that travel through the medium. In this specific case, all generated sidebands are deflected, so only the main frequency participates in the laser beam. Electro-optics modulators are another example of components that can be used to modulate resonators in active mode-locking.

In passive mode-locking, a saturable absorber is used for the modulation, for instance dye cells or semiconductor saturable absorbers (SESAMs). Saturable absorbers are media which allows two electrons' states E_1 and E_2. When the intensity traveling in the resonator is low, the absorbers, as its name suggests, absorb the photons. Once the saturable absorber reaches saturation by receiving a higher number of photons, it becomes transparent, and all electrons in the conduction band E_2 deplete to the valence band E_1, emitting a high and narrow pulse. Once one pulse is emitted, the process of amplification starts again. For ultra short pulses to happen, the saturable absorber must have an excited state lifetime, or recovery time τ, below the pulse duration [106].

So-called mode-locked lasers can employ either active or passive mode-locking principles. However, FDML lasers operate on distinct principles from traditional mode-locked lasers. Despite this difference, FDML lasers establish a phase relationship among successive modes traveling their cavity, earning them the designation 'mode-locked.' A more detailed description of the phase locking mechanism is provided in the following section.

2.3. Fourier Domain mode locking (FDML)

In 2006, Huber et al. presented the principle of FDML [3]. The laser had its central wavelength around 1300 nm, achieving a bandwidth of 105 nm at a repetition rate of 290 kHz. These promising results paved the way for a flourishing future for this technology, which has now become one of the fastest swept-sources in the world usable for OCT, achieving a repetition rate of 13.4 MHz [107]. In this subsection, the general principle of FDML laser is presented along with the operation of two of its main components, the gain medium and its optical bandpass. An introduction to chromatic dispersion and polarization mode dispersion is also given to facilitate the understanding of the challenges encountered in building the 850 nm FDML laser.

2.3.1. General FDML laser principle

As shown in Figure 16, the three main components of FDML lasers are an optical bandpass filter, enabling the tunability of the laser, a gain medium, which amplifies the sweep after each round trip, and a dispersion managed delay. The goal here is to match the driving frequency of the optical bandpass with the inverse round-trip time of the light traveling in the resonator. The resonator is composed of a ~500-meter-long fiber spool used to store and delay the sweep optically. This fiber length is used in FDML lasers to reach a resonator frequency close to the resonance frequency of the optical bandpass, which is around 410 kHz. The advantage of matching the optical bandpass frequency with the resonator frequency is that the laser does not need to build up from spontaneous emission. Precisely, wavelengths filtered by the optical bandpass exit it and traverse the optical path, undergoing amplification by the gain medium before reentering the bandpass. If the length of the fiber and the frequency of the filter match, the wavelength will reach the filter when it is set to this exact filtering wavelength. Consequently, in an ideal case, the wavelength traverses the filter without attenuation beyond the inherent losses of the filter. On the other hand, any wavelengths not in resonance arriving at the filter are reflected by 99.7% (reflective coating of the bandpass filter). It has been observed that only ~10% of the light is actually back reflected [108]. This observation implies that the light entering the filter has the same phase as the previous modes exiting the filter, indicating a significant phase matching, thus affirming the concept of mode-locking.

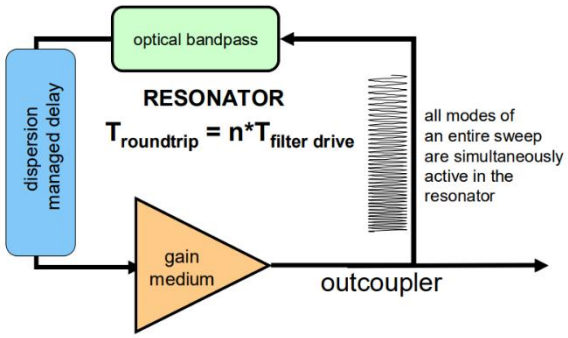

Figure 16. Simplified schematic of a Fourier domain mode locked laser. The light from a gain medium is spectrally filtered by an optical bandpass. An entire frequency sweep is optically stored in the resonator and is subject to a dispersion managed delay to ensure the same round-trip time for all frequencies. The synchronous drive of the optical tunable filter ensures that the light transmitted through the filter will return to the filter at a time when the filter is tuned to the same spectral position again [3].

In FDML lasers, an identical frequency is stored over several hundred round trips, undergoing multiple filtrations and amplification, leading to a progressive reduction in the instantaneous linewidth. Hence, the coherence of the laser output is enhanced. For the same reason, mode-locking improves the RIN of FDML. Also, a Doppler shift happens in the optical bandpass; it forces each successive wavelength to fit in the filter to the resonance frequency. It ensures that the laser can tune as fast as the optical bandpass sweeps.

To achieve mode-locking of all frequencies composing the sweep of an FDML and ensure phase-matching from sweep to sweep, the laser must be dispersion compensated [31, 46]. Due to the long fiber length cavity, chromatic dispersion is introduced in the laser, creating a delay between each wavelength. To compensate for it and achieve the exact same round-trip time for all wavelengths, a dispersion-managed delay is used, as shown in Figure 16. It is usually composed of several types of optical fibers and a cFBG along with temperature control elements. A cFBG is an optical fiber whose core sees its refractive index changing following a specific non-periodic or chirped pattern. This property leads to a reflection of wavelengths with different delays. The design of the grating structure depends on the amount of dispersion in each laser. For the development of the laser source described in this thesis, a chromatic dispersion measurement setup has been developed and is presented in section 3.2.1. The mix of fiber, for instance, HI1060, SMF28e, and LEAF can also be used to help compensate for higher-order dispersion by shifting the zero-dispersion wavelength [46].

To achieve a low noise FDML, i.e. high phase-matching, the remaining chromatic dispersion should ideally be zero [109]. All laser modes are simultaneously active in the cavity, ensuring constant output power. However, it has been estimated that under ~200 fs remaining dispersion over the full bandwidth, the laser is considered ultra-low noise [46], so having a high phase-matching. When an FDML achieves ultra-low noise, it hits what is called the 'sweet spot', making it ideal for OCT applications. Despite effective dispersion compensation, optical phenomena known as 'Nozaki-Bekki holes' persist [110], also named 'intensity dips' when talking about FDML lasers. These are characterized by a significant drop in intensity followed by a sharp overshoot. They occur when a particular wavelength is “lost” due to, for instance, chromatic dispersion, birefringence, or nonlinearity, and require its reconstruction from spontaneous emission. They create a ~30 GHz noise which could seem initially inconsequential when using photodetectors with a bandwidth of 1.6 GHz for OCT. However, it becomes problematic as this noise aliases back into frequencies within the detectable range, introducing noise in the images. The occurrence of holes, when detuning the laser positively or negatively, is asymmetrical around the sweet spot frequency [46, 111, 112]. These observed asymmetries in FDML lasers are discussed further in the subsequent paragraph. Combining this observation and the count of holes, a method has been implemented in the FDML lasers so that they dynamically adjust their frequency over time to maintain the sweet spot [113]. Indeed, a change in temperature causes the laser to drift in frequency, necessitating adjustments. If these adjustments are not compensated for, the high phase-matching is lost over time.

The optical bandpass filter in an FDML laser is a fiber Fabry-Pérot tunable filter (FFP-TF). It is driven by a sinewave generated by a waveform generator; the frequency is set to match the light circulation time in the cavity. Besides, the amplitude can be adjusted within the limits of the filter to achieve a wider bandwidth. Due to the sinusoidal driving of the FFP-TF, it generates two

distinct sweeps: one forward and one backward. Both sweeps can be utilized for OCT, which can be called bidirectional OCT, resulting in a laser repetition rate twice the frequency of the FFP, hence the notation "2x410 kHz." However, as shown in [36, 114], both sweeps show a linewidth asymmetry due to SOA nonlinearities [111, 115-117]. For this reason, when performing bidirectional OCT imaging, both sweeps must be calibrated independently, as detailed later in 4.1.1 and in [31]. Another issue arising from this asymmetry is the stability of the output of the laser [112, 118]. When positive or negative detuning is applied to the laser frequency, causing it to deviate from the sweet spot, each sweep encounters a different type of noise. For instance, the forward sweep experiences discrete frequency jumps while the backward one experiences GHz oscillations, and vice versa.

Instead of using bidirectional OCT, the optical buffering technique can be employed to increase the sweep repetition rate of FDML lasers. The idea is to modulate the SOA with a duty cycle of 2^{-n} and fill the gaps with copies generated by the optical buffering mechanism. By toggling the SOA on and off, specific portions of the sweep can be amplified while blocking out others. This technique offers the flexibility to select the most linear segment of the sweep. Since a sinusoid drives the filter, the outer wavelengths of the spectrum correspond to the turning point of the filter, which creates significant non-linearity in the sweep. Such pronounced non-linearity is undesirable given its implications for post-processing, as elaborated in 2.1.2. Switching on and off the SOA also ensures a gap of signal between subsequent sweeps, hence allowing optical buffering, as shown in Figure 17 top right. For example, opting for a duty cycle of 25% with a filter frequency of 410 kHz results in a complete sweep taking 609.76 ns, with a gap of 1.829 µs between each sweep. Within this gap, it is possible to include three additional sweeps of 609.76 ns each. To achieve this, the laser output is split into two using a 50:50 optical coupler. Half of the light travels directly to a second 50:50 coupler, while the other half traverses approximately 250 m of optical fiber, half of the length of the laser, before reaching the second coupler. At this juncture, during one cycle of 410 kHz, two identical sweeps are present, which results in a frequency of 2x410 kHz = 820 kHz. This process repeats after the second coupler, this time with roughly 125 m of optical fiber. Consequently, the two previous sweeps are duplicated, resulting in a total of four sweeps within approximately 2.439 µs. This configuration yields a frequency of 1.64 MHz, four times the original 410 kHz frequency. The duty cycle can be adjusted like this and has enabled an FDML to reach ~13 MHz with a buffering of 32 times, so a duty cycle of 3.125 % [107]. This process of truncating, for example, 3.125% or 25% of the original sweep, inherently diminishes the bandwidth of the laser. Nevertheless, by increasing the amplitude of the FFP-TF, it is possible to maintain the same bandwidth within the limit of the filter. Furthermore, it has been demonstrated that each sweep after buffering is not entirely identical; they exhibit slight variations in both phase and amplitude arising from single mode optical fibers and different polarization states [119, 120]. Nonetheless, these deviations are minuscule to the extent that buffered FDML remains suitable for application in phase-sensitive OCT [17].

As mentioned earlier, FDML lasers can be used for various applications, and depending on the application, different characteristics are required. In the case of OCT, as mentioned in 2.2.2, an FDML should provide, depending on its center wavelength, an axial resolution of ~10 µm. For instance, at 1300 nm, this corresponds to a bandwidth >100 nm. All FDML lasers developed by the group of the University of Lübeck have a repetition rate of 410 kHz and are usually buffered to 1.6 MHz or 3.2 MHz. It provides fast imaging speed without reducing the axial imaging range.

Figure 17 visually reinforces the earlier explanation regarding the operational principles of FDML lasers. Two isolators are used in addition to ensure unidirectional lasing. A circulator is positioned along the cFBG to ensure that the incoming light that is reflected at the cFBG is then directed again toward the ring. The output of the FDML laser can be at a fiber coupler, as illustrated in the schematic. In some configurations, the output of the cFBG serves as an output to minimize losses.

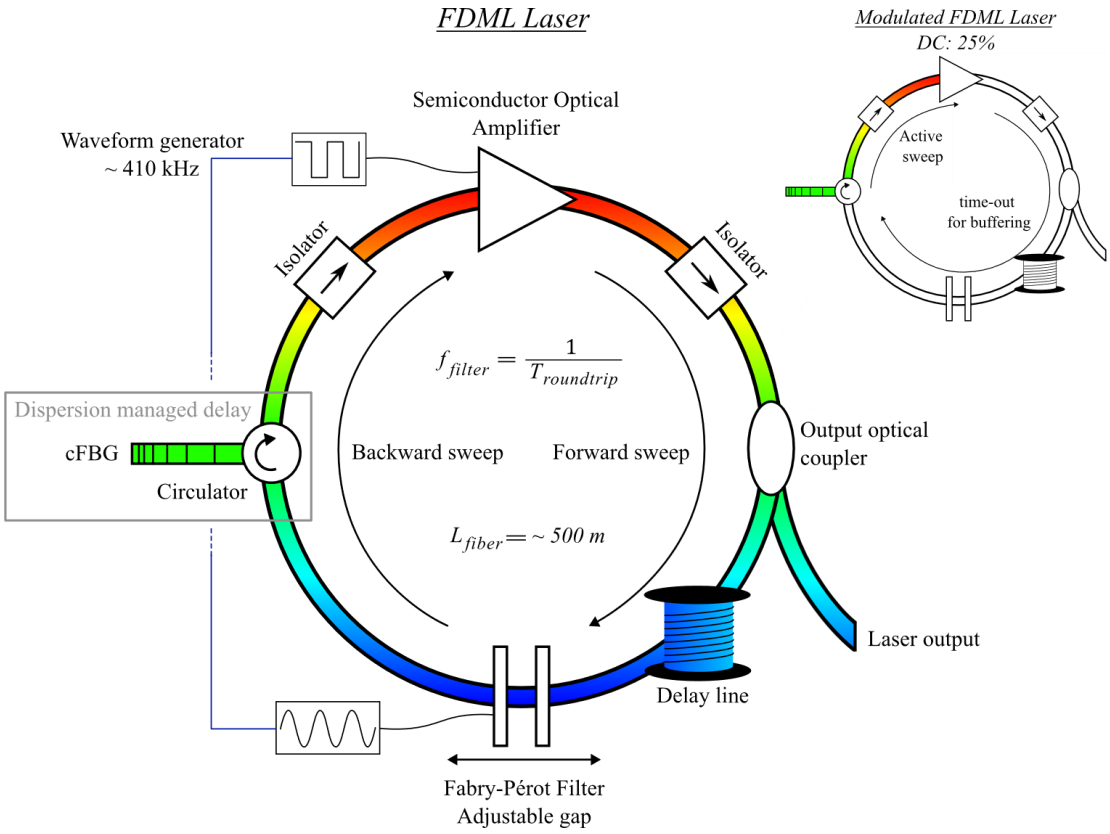

Figure 17: Schematic of an FDML laser and a modulated FDML laser with a duty cycle, DC, of 25%. A complete forward and backward sweep is stored in the long fiber cavity. The Fabry-Pérot filter filtering the broad spectrum emitted by the semiconductor optical amplifier is driven by a sine of 410 kHz generated by a waveform generator. If modulation, a synchronized square waveform is modulating the SOA. Isolators are used to unsure the unidirectional propagation of the light. A dispersion managed delay, composed of a circulator and a cFBG, chirped fiber Bragg grating, is used to compensate for chromatic dispersion. The colors are for illustration purposes only and do not represent the actual bandwidth of the laser.

2.3.2. Fabry-Pérot theory

Since 1899, when C. Fabry and A. Pérot presented this new type of optical bandpass, they have been widely used for several applications like in telecommunications [121], or as optical wavemeters owing to their ability to precisely select wavelengths below the nanometer scale [122]. They are mainly composed of two highly reflective optical glass plates facing each other, where interference happens in between due to the reflection back and forth of the light. Only wavelengths λ that have an integer number of mode N fitting the cavity will create constructive interference. In other words, standing waves. If the distance between both plates is L, the equation defining this phenomenon is as follows:

$$N \cdot \lambda = 2 \cdot L \tag{22}$$

The light circulating in the resonator circulates at a speed $c = c_0 \cdot n^{-1}$. In the case of the FFP-TF used in this thesis, n = 1 since only air is present between both reflective plates. The round-trip time t_{RT} of a wave in a resonator of length L is defined as follow:

$$t_{RT} = \frac{2 \cdot L}{c} = \frac{1}{\Delta \upsilon_{FSR}} = \frac{{\lambda_0}^2}{c_0 \cdot \Delta \lambda_{FSR}} \tag{23}$$

with $\Delta \upsilon_{FSR}$ the free spectral range of the filter. It defines the frequency spacing between two successive transmitted maxima, i.e. two fitting standing waves in the resonator. It can also be expressed in wavelength using $\Delta \lambda_{FSR}$. Figure 18 shows the transmittance spectrum in wavelength of a Fabry-Pérot filter. Three waves with different wavelengths, each spaced by $\Delta \lambda_{FSR}$, have constructive interference in the filter; they are in resonance with the filter. Each successive transmitted wave is separated in phase by:

$$\delta = \left(\frac{2 \cdot \pi}{\lambda}\right) \cdot 2L \tag{24}$$

Each wave matching the resonance is when entering the filter constructively interfering with the circulating wave. These resonances waves also experience reflection at the input mirror of the filter. However, they interfere destructively with the waves leaking out of the resonator. For all other frequencies out of resonance, the inverse phenomenon occurs. Most of them are directly reflected back at the input mirror and interfere constructively with the small field leaking out of the filter. The reflection graph on the right of Figure 18 picture this. All frequencies close to the resonance of the filter travel through the filter. All others are back-reflected when arriving at the filter. An isolating optical component is hence always needed at the input of the filter to block the light.

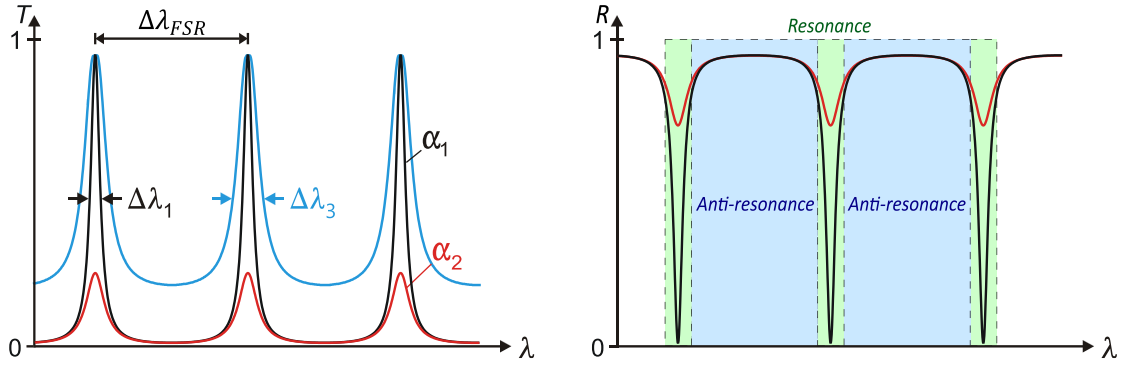

Figure 18. FFP transmittance T and reflectivity R, adapted from [123], α_{loss}: intensity-loss coefficient, $\Delta\lambda_n$: linewidth, $\Delta\lambda_{FSR}$: free spectral range of the filter. The intrinsic optical losses in the filter reduces the filter's transmittance, as shown with $\alpha_1 < \alpha_2$. A high finesse filter, represented here by the black line, shows sharper peaks with a thinner linewidth $\Delta\lambda_1 < \Delta\lambda_3$ and lower transmissions minima than the lower finesse filter drawn with the blue line. The transmittance is at its maximum when the waves entering the filter are at resonance with the latter. All waves in anti-resonance are reflected back and do not travel through the filter.

Fabry-Pérot filters are also characterized by their finesse F, as detailed below:

$$F = \frac{\Delta\lambda_{FSR}}{\Delta\lambda_n} = \frac{\pi\sqrt{R}}{(1-R)} \tag{25}$$

Where $\Delta\lambda_n$ is the linewidth of one fundamental mode at FWHM, as represented in Figure 18 and R the mirrors' reflectivity [124]. It gives information on the filter's ability to discriminate all frequencies (i.e. wavelengths) transmitted. A high finesse induces thin peaks, hence, higher possible discrimination. A high finesse comes with a high reflectivity of both mirrors. The higher the reflectivity the narrower the transmission peak, as shown in Figure 18 left, $\Delta\lambda_1 < \Delta\lambda_3$. The intrinsic loss of the resonator, α, must also be considered. These can arise from poor alignment or absorption from the coating for instance. The higher the reflectivity of the mirrors, the lower the loss must be to ensure a proper transmission of the light and narrow linewidth [125]. Indeed, this loss shortens the photon-decay time which impacts the transmission.

The mirror spacing L directly impacts the free spectral range $\Delta\lambda_{FSR}$. The closer the mirrors the larger the FSR. A large FSR is desirable in FDML laser to only have one covering the gain medium bandwidth. However, the amplitude of the piezo oscillation is limited by the distance of both mirrors. Any contact between both mirrors must be avoided during sweeping to prevent any damage to both coatings.

In this thesis, a home-made FFP is designed and built [126]. The filter is divided into two integral components: the resonator and the fiber coupling stage.

- The resonator is constructed from a fiber ferrule with a high-reflectivity coating, featuring a small concave indent, also called dimple, at its tip. A coated glass plate with the same high-reflective coating is facing the ferrule. These two coated parts are the fundamental elements of the filter. The glass plate is mounted on a piezoelectric actuator ring, offering tunability by adjusting the gap between both components. The piezo-ring presents a hole

at its center to let the light pass through to enter the fiber coupling stage, as shown in Figure 19.

- To recouple the light into an optical fiber, a fiber focuser is used behind the glass plate. To avoid the creation of a second resonator behind the glass plate, its backside is coated with an anti-reflective coating.

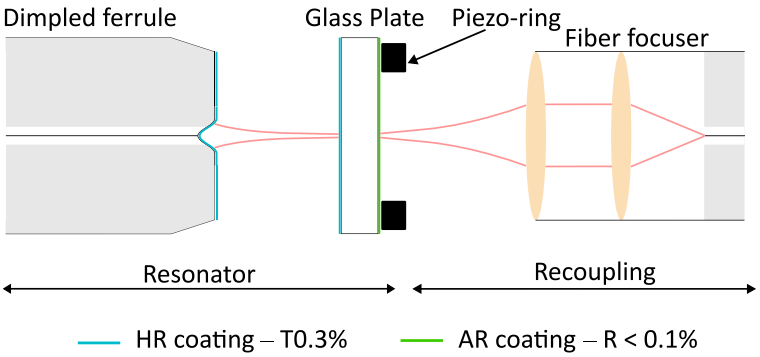

Figure 19. Schematic of an FFP-TF filter design. The light enters the filter from a dimpled ferrule previously coated with a high reflective (HR) coating of ~99.7%. A glass plate coated with the same coating is glued on a piezo-ring positioned in front of the ferrule. The alignment with the dimpled ferrule and the glass plate creates the resonator. Wavelength in resonance with the resonator build up and exit the filter through the glass plate. These modes are re-coupled into an optical fiber by using a fiber focuser. The backside of the glass plate is coated with an anti-reflective (AR) coating to avoid the generation of a second FFP-TF between the glass plate and the fiber focuser.

The resonance frequency of the filter is impacted by several factors:

- The thickness of the glass plate is one of the first impacting components. As mentioned earlier, a reduction of mass, hence a thinner plate, should induce a higher resonance frequency. However, in the case of this Fabry-Pérot filter, the glass plate also acts as a spring. The thicker the glass plate, the harder it is, which implies a higher resonance frequency. Also, as the plate becomes thinner, the escalating presence of Brownian motion within the resonator significantly heightens. This Brownian motion introduces greater random fluctuations, impacting the characteristic of the resonator, hence, for instance, the laser coherence.
- The hole size in the piezo-ring also influences the resonance frequency, similar to the glass plate. A larger hole reduces mass and gives the glass plate greater freedom to oscillate, resulting in a lower resonance frequency.

Therefore, careful consideration must be given to the thickness of the glass plate and the size of the hole in the piezo ring. With meticulous adjustments, it can ultimately approach the targeted resonance frequency, which is defined beforehand by the length of the fiber in the laser.

The above-mentioned dimple created at the tip of the ferrule is used to counteract natural divergence. It also refocuses the beam all the time and reduces loss. This dimple is created by using a CO_2 laser, as shown in Figure 20. The laser beam is aimed at the ferrule and creates a dimple by melting (evaporating) the fiber. The radius of curvature of the dimple must correspond to the wavefront curvature $R(z)$ at a distance z which corresponds to the gap of the filter. z is calculated

with equation (26) and z_R, the Rayleigh range, is determined with equation (27). $R(z)$ can finally be determined with equation (28).

$$z = \frac{\lambda_0}{\Delta\lambda_{FSR}} \cdot \frac{\lambda_0}{2} \tag{26}$$

$$z_R = \frac{\pi {w_0}^2 n}{\lambda_0} \tag{27}$$

$$R(z) = z\left[1 + \left(\frac{z_R}{z}\right)^2\right] \tag{28}$$

The depth Z_t and the width D of the dimple shown in the figure below will depend on the radius of curvature that can be calculated with equation (28).

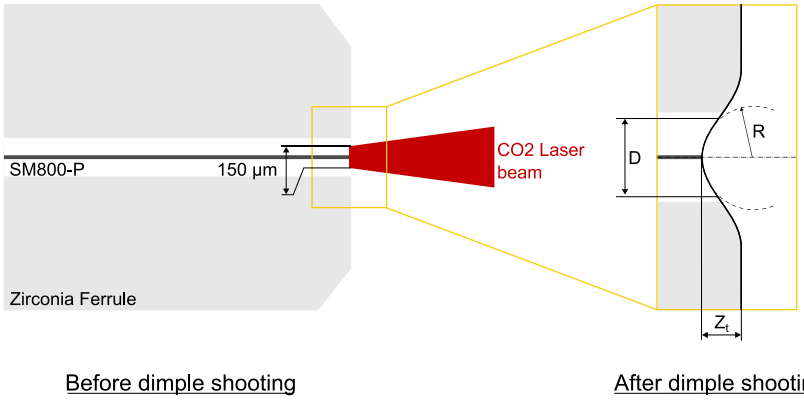

Figure 20. Schematic of the dimple creation on a fiber pigtail. An SM800-P fiber is glued into a ferrule with hi-temp epoxy glue. A 150 µm CO2 laser beam is aimed at the tip of the fiber to create the dimple by evaporation of the fiber. The final dimple shows a radius R of curvature, a diameter D and a depth Z_t.

In FDML lasers, the FFP-TF is designed to achieve an FSR nearing 100 nm, necessitating a narrow gap of just a few micrometers between the ferrule and the glass plate. A finesse of approximately 1,000 is desired and made possible by employing high-reflectivity coatings with reflectivity levels of around ~ 99.7%.

2.3.3. Semiconductor optical amplifier

The second main component present in FDML laser is the SOA. It is the gain medium of the FDML laser enabling for amplification of the sweep. There are several types of SOA. Their active medium can be composed of quantum wells, quantum wires, or quantum dots. In this work, only Gallium Arsenide (GaAs) quantum well SOAs are used.

Quantum wells are nanometer layered structures. They are generally composed of a semiconductor medium positioned between two other semiconductor layers of wider band gaps. Due to this difference in bandgap, the electrons are trapped in the middle layer; here, GaAs. This is called electron confinement. Both outer layers are made from Aluminum Gallium Arsenide (AlGaAs).

The electrons are free to move in the perpendicular plane of the deposition process. These types of devices are electrically pumped, a current is applied to the active medium to create population inversion, as mentioned in section 2.2.1. The electrons will start emitting photons from spontaneous emission. On both sides of the active medium two anti-reflective coatings are deposited to avoid any back-reflection of the light. It is also important to notice that both facets have a slight angle to avoid any Fabry-Pérot effects.

A quantum well can support different energy levels, which results in multiple "sub-bands." These different energy levels allow for a broader emission spectrum. Some of them will only start emitting when the pumping current is above a threshold. These thresholds are important for achieving lasing action. Several quantum wells can also be layered to reach higher amplification gain. The small signal gain of SOAs stands as a pivotal parameter, defining both the amplification capability of the SOA for the laser and the threshold for allowable losses. Maintaining losses below the gain threshold is imperative to enable lasing operation.

Another property of SOAs, which will show its importance in the following, is its catastrophic optical damage (COD). The COD defines the maximum output power that must not be exceeded at both extremity of the SOA. Due to amplification of the gain material, high intracavity power can be observed in SOAs which might, if too extreme, lead to a melting of the material at the facets inducing destruction of the chip. SOAs are fiber-coupled on both sides.

2.3.4. Chromatic dispersion

[Parts of this section have been extracted from the conference paper [127]]

As mentioned in the general introduction of FDML lasers, chromatic dispersion plays a crucial role in their performances. A short introduction of the theory behind it is given here.

When an electromagnetic wave, such as light, encounters a medium, it can be absorbed, reflected, or refracted. If a transparent medium is considered, e.g. optical fiber, light with a specific wavelength travel through the medium at a certain speed, called phase velocity:

$$v_p = \frac{c}{n(\lambda)} \tag{29}$$

It can also be denoted with the angular frequency ω and the wavenumber k as

$$v_p = \frac{\omega}{k} \tag{30}$$

v_p is defined by the velocity with which a phase front propagates in a medium [128]. When individual waves propagate at distinct phase velocities, the resulting wave will not possess a phase velocity that matches its group velocity v_g, as shown in Figure 21. v_g is defined by the speed at which the envelope shape of the waves' amplitudes propagates [129]

$$v_g = \frac{\partial \omega}{\partial k} \tag{31}$$

The lower graph of Figure 21 is the addition of the three waves with three different frequencies plotted in the upper graph. This phenomenon of $v_p \neq v_g$ is known as dispersion.

In the case of optics, it can be called chromatic dispersion. Due to the dependency of the refractive index of glass n, with the wavelength λ, $n = \frac{\lambda_0}{\lambda}$, where λ_0 is the wavelength in air, each wavelength travels at a different phase velocity in a dispersive media. In the case of normal dispersion, the speed of propagation is lower for higher frequencies. Anomalous dispersion depicts the opposite.

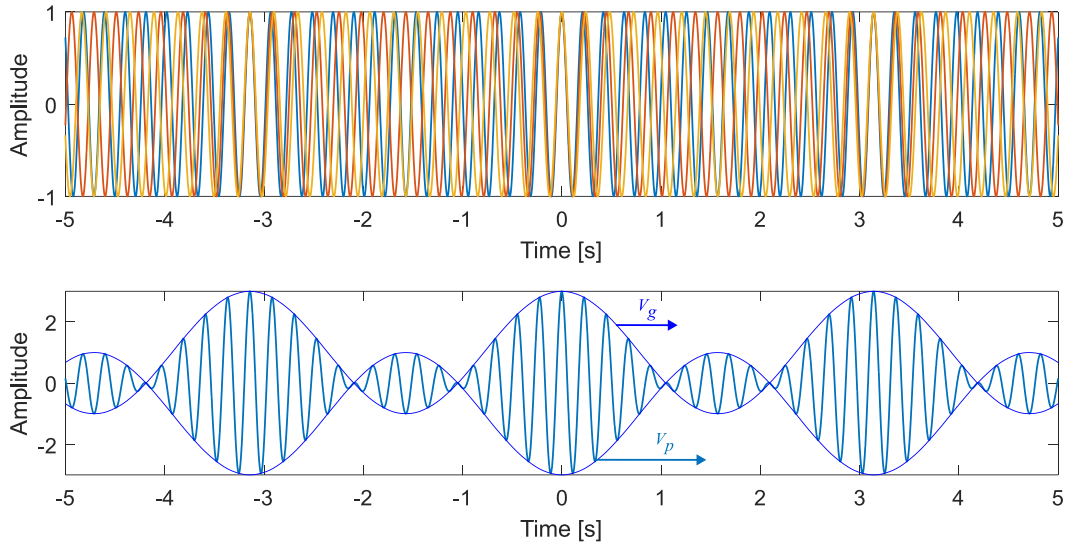

Figure 21. Demonstration of a wave having its phase velocity v_p different from its group velocity v_g. This wave, bottom, is the summation of the three upper waves having three different frequencies.

Chromatic dispersion can be defined using the Taylor expansion of the wavenumber k, as a function of the angular frequency ω, around ω_0 the central frequency of all measurements [130]:

$$k(\omega) = k_0 + \frac{\partial k}{\partial \omega}(\omega - \omega_0) + \frac{1}{2}\frac{\partial^2 k}{\partial \omega^2}(\omega - \omega_0)^2 + \frac{1}{6}\frac{\partial^3 k}{\partial \omega^3}(\omega - \omega_0)^3 + \cdots \tag{32}$$

In other words, the Taylor expansion allows to approximate the relationship between the phase delay and the wavelengths. Each of its orders has several definitions, which are depicted below. Only the two first orders are studied and measured in this thesis. If more precision on the approximation of the dispersion is needed, higher-order dispersion can be considered.

- Zero-order dispersion, defining a common phase shift: k_0
- First-order dispersion noted k', describes the overall time delay without an effect on the pulse shape, it is the linear component. k' is, as shown in the formula below, defined by the inverse of v_g, which corresponds also the group delay per unit of length. The unit of k' is $fs \cdot mm^{-1}$.

$$k' = \frac{\partial k}{\partial \omega} = \frac{1}{v_g} \tag{33}$$

- Second-order dispersion noted k'', or also called the group velocity dispersion GVD. It is the derivative of k' with respect to ω. The unit of k'' is $fs^2 \cdot mm^{-1}$.

$$k'' = \frac{\partial^2 k}{\partial \omega^2} = GVD \tag{34}$$

Regarding optical fiber, the more commonly used parameter is the dispersion parameter, D_1, which is the derivative of the first-order dispersion with respect to the wavelength. Its unit is usually written as $ps \cdot (nm \cdot km)^{-1}$. The following equation is linking $k''$to D_1:

$$\boldsymbol{k''} = \frac{\partial^2 k}{\partial \omega^2} = \frac{\partial}{\partial \omega} \cdot \frac{\partial k}{\partial \omega} = \frac{\partial \lambda}{\partial \omega} \cdot \frac{\partial}{\partial \lambda} \cdot \frac{\partial k}{\partial \omega} = \frac{-2\pi c}{\omega^2} \cdot \frac{\partial}{\partial \lambda} \cdot \frac{\partial k}{\partial \omega} = \frac{-{\lambda_0}^2}{2\pi c} \cdot \frac{\partial}{\partial \lambda} \cdot \frac{\partial k}{\partial \omega}$$
$$\boldsymbol{k''} = \frac{-\boldsymbol{\lambda_0}^{\boldsymbol{2}}}{\boldsymbol{2 \cdot \pi \cdot c}} \cdot \boldsymbol{D_1} \tag{35}$$

Considering D_1 and not k'', a specific care should be given about the definition of normal and anomalous dispersion. Since they have an opposite sign, normal dispersion is defined for D_1 such that the propagation is faster at lower frequency (i.e. longer wavelength), hence $D_1 < 0$ for normal dispersion and $D_1 > 0$ is anomalous dispersion is considered. The different sign is due to k'' using the frequency derivative and D_1 the wavelength derivative. D_2 is the second parameter used in optical communication. It corresponds to the derivative of D_1, with respect to the wavelength expressed in $ps \cdot nm^{-2} \cdot km^{-1}$.

Due to chromatic dispersion, if a light pulse propagates through an optical fiber, it will broaden due to the GVD. This broadening can lead to major issues in applications like data transmission in telecommunications [131], fiber-based mode-locked lasers or, for instance in FDML lasers [3] as mentioned in section 2.3.1. In the aim of compensating chromatic dispersion, its amount must be known beforehand.

Four fundamental methods are often used to measure the chromatic dispersion of optical fiber [132]. Temporal or spectral interferometric methods can be used, such as Mach-Zehnder [133, 134] or other interferometers [135]. They are used for short fibers of interest of a few meters. The Chromatis™ Dispersion Measurement System commercialized by Thorlabs is using a white light interferometer that achieves a group delay dispersion resolution of ± 5 fs^2. On the other hand, the time-of-flight of pulses can be measured with either supercontinuum lasers to cover a very broad spectrum [136] or with a simple tunable light source [137-139] to determine the group delay. For instance, FDML lasers can be used to measure the dispersion of optical fibers at high speed [140]. The latest method requires a relatively long fiber, about 1 km, to add a long enough delay to differentiate between reference and sample. Lastly, the time delay can be determined from the phase shift between two signals. However, this method is time-consuming because a full

interference spectrum must be measured repeatedly [141]. The company Viavi is achieving a dispersion uncertainty of ± 0.3 ps/nm/km with a 10 km fiber length in a few 10^{th} of a second in their system T-BERD/MTS around 1550 nm.

In this thesis, the optical fiber used, Hi780, is subject to normal dispersion at 850 nm. Their turning point to anomalous dispersion is around 1300 nm, where the zero-dispersion wavelength can be observed. A new system has been developed to characterize them. It combines a time-of-flight measurement with a cross-correlation algorithm for higher accuracy measurement than the ones mentioned above. All experiments and results are presented in section 3.2.1

2.3.5. Polarization mode dispersion

In the realm of optics, it is widely acknowledged that circulators can introduce polarization mode dispersion (PMD). During the development of the new 850 nm FDML laser, it was noted that the circulators being used introduced PMD. Since a few experiments have been conducted to analyze this phenomenon, a brief introduction to its theory is provided.

Electromagnetic waves, such as light waves, are defined as transverse waves. E and B, the electric and magnetic field vector respectively, are perpendicular to each other and to the propagation of the wave. In the scenario presented in Figure 22, the light beam is described as linearly polarized. All electric field E can be decomposed into components along two orthogonal axes called the slow and fast axis. If both axes do not propagate at the same speed, a phenomenon called PMD occurs. It is typically measured in $ps/\sqrt{\text{km}}$. One axis experiences a delay relative to the other, as indicated in Figure 22 right. This delay, expressed in picoseconds, is called differential group delay (DGD). This can happen if the wave propagates through a birefringence medium. Birefringence happens when the refractive index changes with the polarization state of the input state. Optical fibers might become birefringent if a defect in the material occurs. For instance, internal stress like core stress, cladding eccentricity, or an elliptical design occurring during the fabrication process. Also, external stress like fiber bending or fiber stress can generate birefringence.

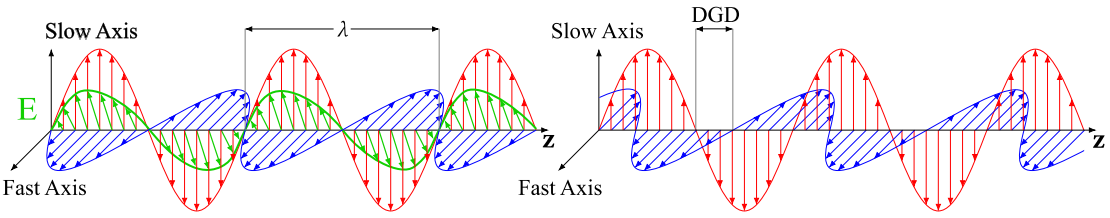

Figure 22. Linearly polarized electric field, E, of wavelength λ, propagating in the Z direction. E can be decomposed in two axis, the slow and fast axis. Both axis experience a differential group delay on the right which impact the polarization of the electric field [142].

If a light beam enters a single mode fiber, it propagates in a single fundamental mode with a specific polarization defined by both orthogonal states. Polarization might be distorted due to PMD and arrive at the output of the fiber with a completely different polarization. The separation

of both polarization components causes pulses to broaden in time which can be an issue for telecommunications for example [143, 144]. This issue can be mitigated by employing polarization-maintaining (PM) fibers, where the preservation of polarization state is achieved through the integration of two stress rods encircling the core. These stress rods induce controlled high birefringence in the core, reducing its sensitivity to external factors such as bending and temperature variations.

In general, PMD compensation should be possible if no wavelength dependent PMD is introduced (linear system), i.e. narrow bandwidth. Fiber polarization controllers can be used along with a polarizer to align the polarization of the light to one polarization direction. Polarizing fibers can also cancel PMD, however, it is more expensive, and it might introduce much loss since the polarization has to be aligned at the interface. Non-linearly cFBGs, liquid-crystal modulator arrays, or electrical PMD compensators [145-149] are also known to be able to compensate for PMD exhibited by kilometer long optical fiber. It should also be known that PMD is sensitive to temperature changes, which makes it time dependent. Also, since PMD effects are random, its compensation usually needs a feedback loop to ensure compensation over time.

2.3.6. Motivation for building a new light source: 850 nm FDML Laser

Numerous iterations of FDML lasers have undergone development and experimentation in pursuit of optimal performance for specific applications. Variants utilizing PM-Fiber were explored to mitigate PMD concerns, yet this approach yielded suboptimal outcomes [150]. Early FDML implementations lacking dispersion compensation exhibited reduced performance for OCT compared to the one developed specifically for this application today [108]. Additionally, efforts to enhance FDML gain involved integrating various types of active fibers into the cavity, such as Erbium and Ytterbium fibers [7, 151-154]. However, these endeavors were met with challenges, notably the emergence of Q-switching behavior leading to potential damage to critical components, including the FFP-TF, owing to excessive power and mirror burning [108]. Diverse filtering techniques, such as polygon scanners, were also investigated [155, 156]. Furthermore, strategies to broaden the laser's bandwidth included incorporating dual SOAs within the cavity [157].

Current research efforts predominantly center around enhancing the speed of lasers and refining post-processing techniques for OCT image optimization. Additionally, significant attention is directed towards advancing the capabilities of these lasers towards new frontiers, including phase-sensitive OCT, dynamic OCT, and endoscopic OCT applications. Notably, lasers from Optores GmbH are prominently featured in these endeavors. Available commercially at wavelengths of 1060 nm, 1300 nm, and 1550 nm, these lasers encompass a broad spectrum tailored to address various SS-OCT requirements.

Ophthalmic imaging stands as the foremost market for OCT technology to date. Continuous advancement in this field necessitates the extraction of additional information from samples to

enhance medical diagnostics for potential diseases. As previously highlighted, the advent of an 850 nm FDML laser holds promise for enhancing retinal imaging capabilities, particularly in terms of resolution and heightened scattering in the upper retinal layers. Moreover, such technological progress may extend beyond ophthalmic imaging, presenting opportunities for novel applications.

In pursuit of this objective, the conventional FDML laser architecture, depicted in Figure 17, is tailored to operate at 850 nm. The comprehensive developmental processes are delineated in subsequent sections, wherein all encountered challenges stemming from the transition to lower wavelengths – such as heightened chromatic dispersion, elevated PMD, and diminished gain – are meticulously addressed. Various techniques employed to cope with them and corresponding results attained are exhaustively presented.

The evaluation of laser performance involves conventional measurements such as phase stability, roll-off, sweet-spot characterization and noise analysis. It also includes an assessment based on retinal imaging, in which *in-vivo* images are acquired using two separate processing techniques, subsequently subjected to comparative analysis and discussion.

Furthermore, a comparative study is conducted between ophthalmic SS-OCT data obtained using a 1060 nm FDML laser and the 850 nm variant. This comparative analysis aims to discern the improvements, if any, facilitated by the 850 nm laser in ophthalmic imaging applications.

3. DEVELOPMENT OF AN 850 NM FDML LASER

This chapter outlines the development process of the 850 nm FDML laser. All newly developed key components enabling this wavelength, such as the home-built FFP-TF and the SOA manufactured by Superlum Diodes Ltd., are introduced. Promising results achieved with a narrow bandwidth, ~24 nm, are presented, highlighting the challenges that need to be addressed to extend the FDML's bandwidth. The subsequent challenges and the experiments conducted to overcome them are discussed. Finally, the performance and characterization of the new light source are detailed before the concluding part of this section.

3.1. Initial development and identification of challenges

This section presents the characteristics of the two main components used in the laser: the custom-developed FFP-TF and the SOA. It also discusses initial results from the first laser prototype, which achieved an optical bandwidth of 24 nm, along with an evaluation of its performance at this stage and strategies for enhancing the design to further expand the bandwidth.

3.1.1. Customized FFP-TF for 850 nm

In this sub-section, all characteristics and performances of the filter used for all forthcoming results are detailed. The filter's theory and schematic can be found in 2.3.2.

Filter's components:

Due to the coating process used to coat the glass plates and the ferrules' tips, as detailed in section 2.3.2, high-temperature-resistant components must be used to avoid any evaporation of chemicals that could potentially impair the coating machine. For this, home-made pigtails were assembled. Fibers with a high-temperature coating (SM800(5.6, 125)P, fibercore) were glued with high-temperature epoxy (EPO-TEK 353ND, Thorlabs) into ferrules. Once polished, dimples were shot to aim for an FSR of 80 nm, which leads to a radius of about 250 µm, as demonstrated with equation (28).

The ferrule used in the filter has a dimple with a radius of 140.28 µm and an eccentricity of 0.49 µm. A trade-off must be found between the eccentricity of the dimple and its radius. In this case, an eccentricity below 1 µm is preferred as a radius closer to 250 µm. It ensures easier and better alignment of all components. The radius of 140.28 µm would imply a gap in the filter of 8 µm leading to an FSR of 45 nm. It can be increased to 80 nm by bringing the glass plate and the ferrule closer together. However, this might increase the loss in the filter since the dimple would not be used at its best performance. A dimple with a radius of 250 µm and an eccentricity of 2 µm would require precise tilting of the ferrule for proper alignment. However, the tilting is

significantly constrained due to the narrow micrometer-sized gap, especially considering the ferrules used here have a diameter of 2.5 mm. Hence, the first option is preferred.

Figure 23 (A) and (B) show the characterization of the polishing process. The dimple profile can be seen in (C). A profilometer utilizing a light-emitting diode (LED) with an emission wavelength of approximately 532 nm enables precise surface profile measurement of a ferrule through interferometry. In this setup, a piezoelectric element positioned beneath the ferrule holder allows controlled movement along the optical axis (parallel to the incident light beam). This motion enables accurate reconstruction of the surface topography by shifting the interference fringes. The spacing between two adjacent interference fringes, or circles, corresponds to half the wavelength of the light used. In this case, with a wavelength of 532 nm, the fringe spacing is 266 nm. The two noncircular distinct black lines in (A) are due to dust on the camera of the profilometer.

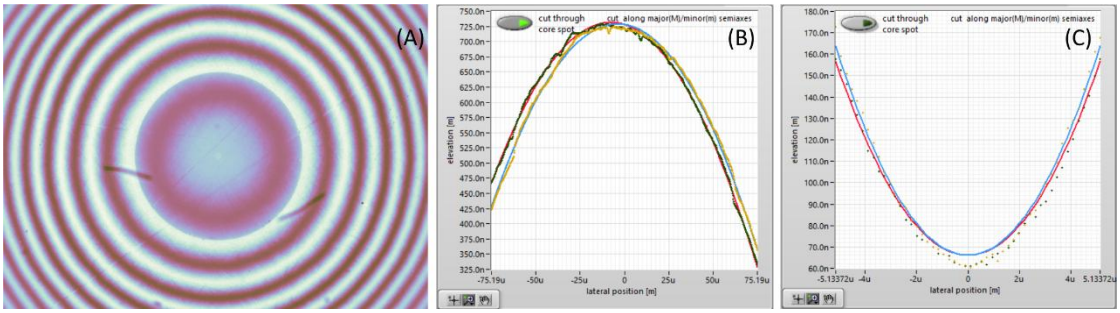

Figure 23. Ferrule surface characterization after gluing and polishing. (A) shows the interference pattern at one position on the ferrule after polishing. (B) and (C) show the elevation as a function of the lateral position of the ferrule's tip after polishing and the one of the dimple after shooting respectively.

(A) and (B) show that the polishing process produced a satisfactory surface finish without cracks and holes. The surface is smooth and free of any defects or discontinuities. Care must be taken to ensure that no cracks are present near the fiber where the dimple will be formed. Experimental observations have shown that if a crack is located close to the tip, it can distort or displace the dimple by several micrometers, which is undesirable. If any cracks are detected during the polishing process, an additional round of polishing should be performed to eliminate them. The minor roughness observed at the tip of the ferrule in (B) is not a concern, as it is minimal and will not affect the dimple's formation or performance. The dimple in (C) shows low roughness, which can be attributed to the precision of the laser-based formation process.

Once dimples are shot and characterized, all ferrules and glass plates are sent for coating. A high reflective coating of 99.7 % is deposited on the front of the dimples and the glass plates. A 99.9 % anti-reflective coating was deposited at the back of the glass plate. 250 µm thick glass plates are used.

A piezo element with a hole of 2.02 mm is used and shows a resonance frequency of 413 kHz.

Filter's performances:

The filter's spectral window Δλ has been measured to be 84 pm at FWHM, as shown in Figure 24. A reference measurement, represented by the orange curve, is obtained by measuring the ASE of an SOA isolated from the OSA using an isolator. The spectral window of the filter, shown as the blue curve, is then measured by positioning the FFP-TF after the isolator and recording the output on the same OSA with identical sensitivity and resolution settings. The gap between both reflective surfaces is estimated to be about 3 µm. From this estimation, the FSR is calculated to be about 83 nm for a center wavelength of 850 nm. Unfortunately, the FSR cannot be measured due to the narrow gain spectrum of the SOA, about 50 nm, presented in the following sub-section.

The quality of the alignment is of importance to define the finesse of the filter, as mentioned in the section presenting the theory on Fabry-Pérot filters, section 2.3.2. As shown in Figure 24, the loss of the filter used in the laser is measured to be 5 dB. The finesse is estimated to be around 1,000 considering no extra loss coming from alignment and using equation (25).

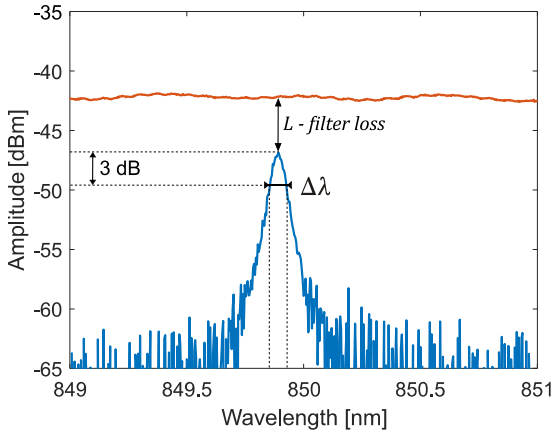

Figure 24. FFP-TF characterization. The filter shows a spectral window of 84 pm and a loss of 5 dB. Blue: output of the filter, orange: input of the filter.

3.1.2. Semiconductor optical amplifier in use

All SOAs tested and used in the laser were provided by Superlum diodes Ltd and are GaAs quantum well SOAs.

Various SOAs (SOA-372, SOA-372-SM, SOA-372-DBUT-SM, SOA-372-DBUT-PM-NEW) were used during this PhD thesis. This choice stemmed from the ongoing development of SOAs by the company, featuring enhancements such as increased gain, expanded bandwidth, and diverse fiber end options, including PM and SM fibers. Nevertheless, all of them exhibited a comparable ASE spectrum characterized by two distinct "sub-bands," as shown in Figure 25. The initial sub-band starts emission from the outset, featuring a central wavelength of approximately 850 nm. The second sub-band, requiring a higher pumping current due to its lower wavelength, manifested around 820 nm. This higher bandgap lasing contributes to achieving a broader gain

spectrum. Figure 25 facilitates the comparison of the output spectrum of the SOA at 100 mA and 150 mA, with 250 mA being the maximal current applicable, revealing the emergence of a distinct sub-band. Additionally, a subtle variation in output power between the input and output ports of the SOA is noticeable. This discrepancy could be attributed to factors such as fiber coupling effects post-facets or variations in the coating on the two facets.

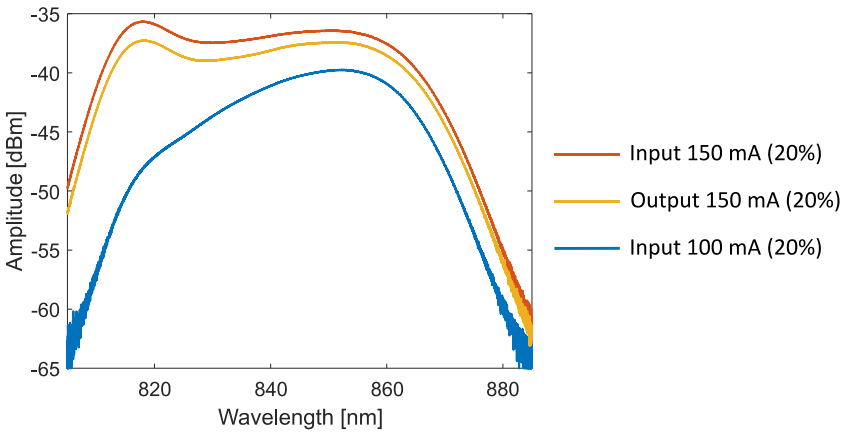

Figure 25. Output spectrum measured at the input and output of the SOA-372-DBUT-SM used in the FDML laser, at 100 mA and 150 mA. A sub-band of the emission appears at around 820 nm when the pumping current is increased around 150 mA.

This SOA has a small signal gain of 22 dB and a FWHM bandwidth of 52 nm at around 150 mA. It is coupled in SM fiber, and the output power at maximum forward current is 7.2 mW (SOA-372-DBUT-SM). It presents a COD of 20 mW, imposing a constraint on the circulating power within the FDML laser and consequently affecting the output power.

3.1.3. From 24 nm to 72 nm

In results of new research in semiconductor photonics and manufacturing of SOAs around 850 nm as shown previously, a door opened for the development of a new 850 nm FDML laser [158]. The performances of the first 850 nm FDML laser are presented in this section. The FPP-TF, as outlined in section 3.1.1, is employed in conjunction with a comparable SOA to that described in section 3.1.2, albeit with lower output power (SOA-372-SM, Superlum diodes Ltd.). The cFBG used here (Teraxion, PSR-840-23(+D50.318-0.105)-0S1-0R) has a bandwidth of 23 nm and a reflectivity of 47.8 %. The narrowness is due to the high chromatic dispersion present in Hi780 optical fiber around 850 nm. Standard cFBGs are manufactured by UV illumination with 10 cm masks. The masks' length limits the group delay's compensation to 1200 ps, which is linked to the bandwidth by chromatic dispersion. At 850 nm, a chromatic dispersion of 100.636 $ps.nm^{-1}.km^{-1}$ is measured with the setup presented in the next section. To synchronize the cavity round-trip time with the filter period of approximately 2.421 µs (413 kHz), calculations were performed for a 500-meter length of fiber (with n=1.4586). This yields a chromatic dispersion of 50.318 $ps.nm^{-1}$, corresponding to a maximum bandwidth of approximately 24 nm.

Figure 26 shows the first design of the 850 nm FDML. Both, 90/10 fiber couplers are used as probe output to monitor the power circulating in the laser. The output of the laser is taken at the output of the cFBG. Figure 27 shows the performance of the 23 nm FDML at a repetition rate of 411,779.588 Hz. The spectrum is presented in (A). (B) illustrates the time trace acquired with a 30 GHz photodiode (Thorlabs, DMX30AF). The backward and forward sweep can be seen. The forward sweep, from 2.25 µs to 3.4 µs shows less noise on the left than on the right side, which indicates that there is some first-order chromatic dispersion remaining. Also, it indicates that the laser is close to sweet spot operation. If the dispersion is better compensated, both sweeps, the forward and backward are more alike. All data presented in Figure 27 (B), (C), and (D) are acquired with the 80 GS/s digital storage oscilloscope (DSO) (Keysight, DSOZ634A).

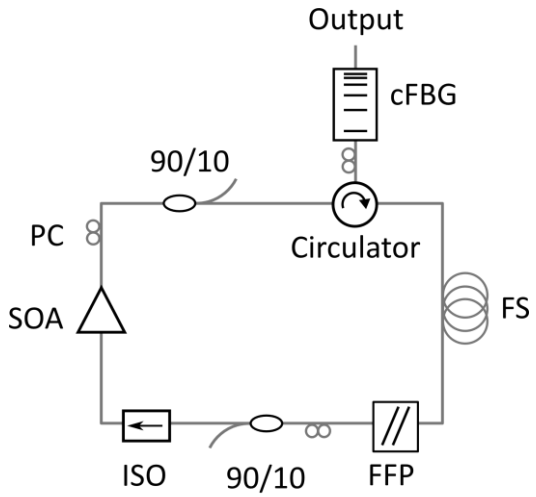

Figure 26. Schematic of the first 850 nm FDML laser. SOA: semiconductor optical amplifier, PC: polarization controller, cFBG: chirped fiber Bragg grating, FS: Fiber spool, FFP: Fiber Fabry-Pérot filter, ISO: Isolator.

A MZI has been set up, with two free-space beam paths to measure the sensitivity roll-off of the laser, presented in Figure 27 (C). An interference fringe is acquired every 1 mm. The phase of the 7th fringe is used for calibration of all others after being filtered by a low pass filter (sampling rate: 80 GS/s, cut-off: 400 MHz). The single-*k*-calibration technique is used for calibration. All data are acquired here with a 1.6 GHz balanced photodiode spliced with Hi780 and Hi1060 to avoid any multimode operation due to the use of SMF-28 fiber in the photodiode (Thorlabs, PDB480C-AC). As shown in Figure 27 (C) the coherence length at 12 mm decreases by 6 dB. The cut-off frequency of 1.6 GHz can also be observed in (C) by the sudden decrease of the noise floor around 1.6 GHz.

Finally, the phase evolution of the laser over 100 segments, representing 100 sweeps since the oscilloscope's re-arm time is around 2.5 µs, is presented in Figure 27 (D). The phase of the first acquired segment, at around 5 mm, is used to calibrate all following segments. Only the forward sweep of a complete sweep (forward and backward) is used for calibration. It can be seen that the phase breaks down after the 49th segment, as a loss of amplitude is observed in the point spread function, indicating that the calibration based on the first segment is not effective for these

segments. However, it is recovering in less than 10 more segments which shows the capability of the laser in terms of phase stability.

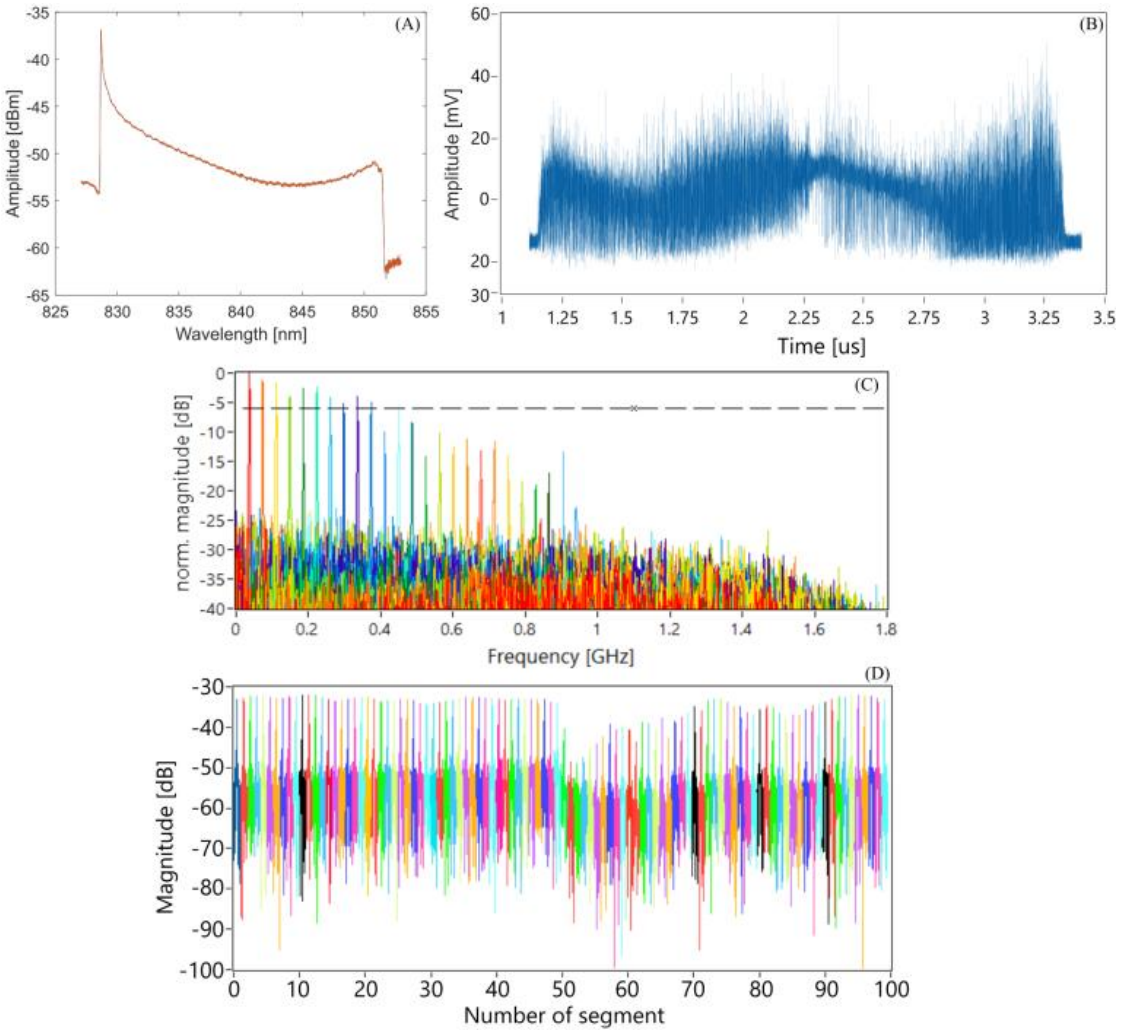

Figure 27. (A) output spectrum of the 850 nm FDML laser. (B) time trace of the laser output showing both backward and forward sweep. (C) Sensitivity roll-off, dashed line illustrating the limits of -6 dB. (D) Phase evolution at one frequency over 100 consecutive segments.

All these initial results are promising, but they point to areas where there is room for improvement. Especially regarding the chromatic dispersion compensation, which would improve the noise, the sensitivity roll-off and the phase stability of the laser. Besides, in the hope of achieving an axial resolution below 10 µm, the bandwidth must be extended. Yet, the cFBG is the limiting component. If removed while keeping the circulator as isolation component, it is shown in Figure 28 (A) that the laser could lase over a wider range than 24 nm. The polarization in the laser and the frequency of the filter are adapted to enable lasing over the full range of the sweep. Generally, the frequency is optimized for one side of the spectrum and the polarization for the other side. If both are optimized for the same side, a band might experience too high loss. For instance, in Figure 28 (A) the frequency is optimized at around 832 nm, and the polarization is optimized on the right side. Figure 28 (B) shows narrower spectra of about 25 nm at different positions along

the gain spectrum. The frequency is adjusted at around 848 nm as the higher amplification shows i.e. for a good phase matching at these wavelengths.

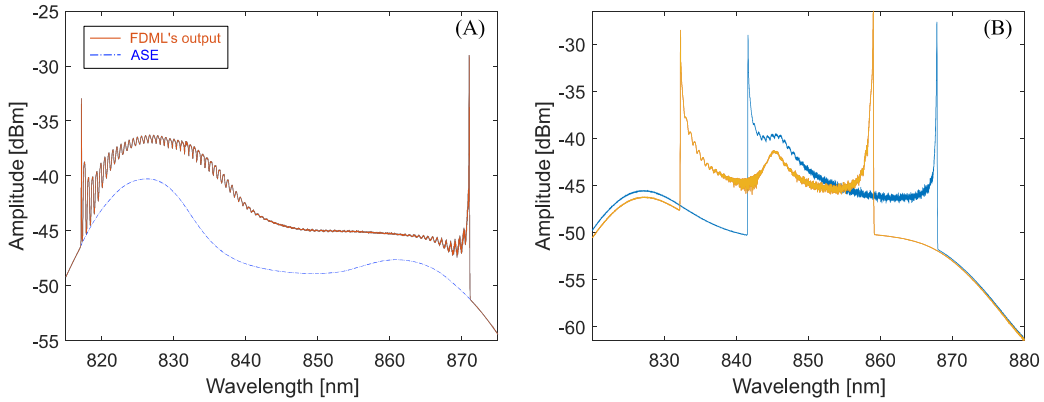

Figure 28. Output spectrum of an FDML laser without chromatic dispersion compensation. The frequency of the laser is optimized at around 832 nm and 848 nm in (A) and (B) respectively. Polarization is optimized in both cases to obtain a broader spectrum. (A) shows a bandwidth above 50 nm and (B) 25 nm.

However, without using a dispersion compensation element, the long roll-off and phase matching characteristic of FDML lasers would be absent, resulting in poor-quality OCT images. By employing three cFBGs (custom-design, TeraXion Inc., Canada), each compensating a third of the cavity dispersion, the bandwidth of the sweep can be theoretically extended to a maximum of 72 nm. Consequently, three circulators are required, as shown in the first draft of a new laser presented in Figure 29.

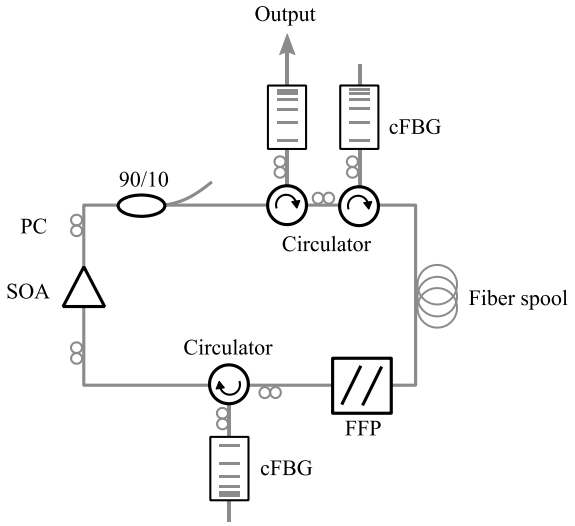

Figure 29. New FDML laser configuration using 3 cFBGs. SOA: semiconductor optical amplifier, PC: polarization controller, cFBG: chirped fiber Bragg grating, FFP: fiber Fabry-Pérot.

While employing three cFBGs would indeed expand the available bandwidth, and the SOA demonstrated its proficiency in amplifying over a wide range, additional hurdles emerged. This particular wavelength also introduces challenges such as heightened losses in optical components, reduced gain amplification, and increased polarization mode dispersion. To address these issues,

a series of experiments were conducted prior to the laser's construction, all of which are detailed in the subsequent section.

3.2. Challenges in developing an 850 nm swept-source

Optical components have been developed principally with telecommunication aim. Implying 1550 nm, or 1310 nm wavelength range. For this reason, very high performing optical components, low loss, high gain etc. can be found. Nowadays, new applications needing shorter wavelength ranges like for ophthalmic OCT, have brought interest in shorter wavelengths. Production of 850 nm optical components started a few decades ago and enabled the first retinal OCT. However, components remain less performant than 1310 nm parts. These induce a lot more challenges in building swept-sources at shorter wavelengths. Also, 1310 nm is a more forgiving wavelength than 850 nm due to its lower dispersion, reduced signal loss, and greater tolerance to misalignment.

All experiments carried out to study these new challenges, the description of the methods and all results are presented in the following order. First, how to accurately compensate for the high amount of chromatic dispersion. This followed by the issue introduced using circulators at 850 nm, how to deal with PMD. The noise of the laser will also be presented related to the gain present in the laser. A new layout of the FDML laser has also been tested and is presented in the following. To compensate for the high losses, it uses a dual amplification method. Finally, the last challenge that had to be faced was the low performance of photodiodes at 850 nm. Either due to low sensitivity or low amplification, a new photodiode had to be home-built. A comparison of different photodiodes is presented.

3.2.1. Measurement of chromatic dispersion in optical fibers

[The work presented in this section has already been published in 2022 at the Photonics West conference [127]. Most of the sentences, paragraphs and figures are extracted from it.]

As mentioned in the previous section 2.3.1, it is necessary to accurately compensate for the dispersion in FDML lasers to obtain a high-performance laser. Chirped fiber Bragg gratings are used in FDML for this purpose. To obtain accurate compensation for chromatic dispersion, it is necessary to determine the amount of chromatic dispersion in the optical fiber at the design wavelength. In that context, a high accuracy chromatic dispersion measurement has been developed and is presented here.

The method used in this setup measures the 1st and 2nd-order dispersion of optical fibers with an ultra-high accuracy system combining a time-of-flight and a phase-shift measurement. The reference and sample arm, where the fiber under study is placed, are separated to enable the measurement of the time shift in short and long fiber. Thus, the delay between the reference and sample arm is measured at each wavelength to retrieve the group velocity slope and finally obtain D_1 and

D_2, the dispersion parameters of the fiber of interest. The system has been built at first around 1080 nm for proof of concept and for characterization, components being more performants allowing for better precision than at 850 nm.

3.2.1.1. Experimental setup

The optical setup is presented in Figure 30. It consists of a self-built wavelength tunable laser. A broadband SOA (Innolume, SOA-1070-70-HI-24dB) emits a broad ASE spectrum, being subsequently spread spatially by a ruled diffraction grating (Thorlabs, GR25-0610). Only a small fraction of the light is then coupled back into a fiber achieving a wavelength bandpass filtering. The measured linewidth of the laser is <5 GHz or <20 pm which is limited by the resolution of the optical spectrum analyzer (OSA) (Yokogawa, AQ6370). The filtered light propagates back to the SOA where it is amplified. The laser has an optical output power of 9.5 mW at 1090 nm. 30% of the laser light is coupled out and split again by a 90:10 coupler. The 10% output is used to monitor the emitted wavelength of the ring laser with the OSA. The light coupled out at the 90% output is used for the dispersion measurement. It propagates through polarization controllers and a polarizer until it is modulated by an electro-optic modulator (EOM) (iXblue, NIR-MX-LN-40). The light is split again into a 70:30 ratio where the 70% output is going in the sample arm, where losses from the long fiber spool need to be compensated for. The other 30% are used for reference measurements. Fast photodiodes detect each signal. In the case of the reference light, a 35 GHz photodiode (PD1) (Discovery Semiconductors Inc., DSC20H) is used, and in the case of the sample light, a 30 GHz photodiode (PD2) (Thorlabs, DXM30AF) is used, as shown in Figure 30. The photodiode with the higher amplification, PD2, is used for the sample arm where the power is lower. Both PDs are connected to an 80 GS/s real-time DSO (Keysight, DSOZ634A) to acquire the data. All the dispersion measurements in the 1080 ± 50 nm range are realized with a 307 m long fiber spool of Hi1060. The spool is placed inside a thermally insulated housing where the temperature is constant at 27°C or 30°C. The output power of the reference and the sample arm is 1.1 mW and 1.4 mW, respectively, at 1080 nm.

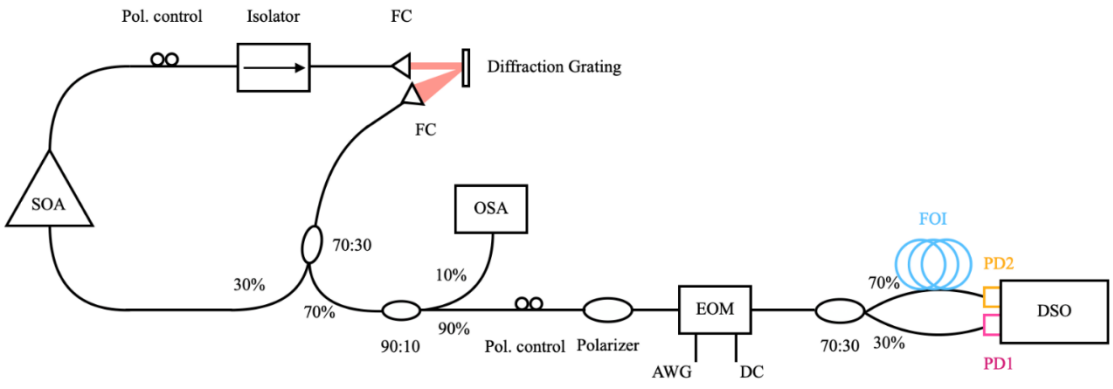

Figure 30. Dispersion measurement setup based on a tunable ring laser on the left followed by the modulation and dispersion measurement part on the right. (SOA, semiconductor optical amplifier; FC, fiber collimator; OSA, optical spectrum analyzer; EOM, electro-optic modulator; AWG, arbitrary waveform generator; DC, direct current; FOI, fiber of interest; PD, photodiode; DSO, digital storage oscilloscope).

The optical setup has been adapted to realize 850 ± 15 nm measurements. A 610 m long 780-OCT fiber spool (Nufern) is used as the fiber of interest, and all components were specifically designed for 810 ± 50 nm with 780-HP (Nufern) single-mode fiber. This fiber spool is placed inside the thermally insulated housing likewise. The center wavelength of 810 nm was initially chosen because it was anticipated that an SOA with a center wavelength near 810 nm would be used. However, the SOA ultimately procured had a center wavelength of approximately 850 nm, which consequently determined the laser's center wavelength.

The modulation is realized by a 24 GS/s arbitrary waveform generator (AWG) (Tektronix, AWG7122B). It consists of a 4 GHz sine burst with 1000 cycles including a pulse type marker at the beginning and the end of the burst. It is important to mention here that the AWG used in this setup does not provide the same output amplitude at different frequency, as shown in Figure 31. The higher the frequency the lower the output amplitude created by the AWG. Usually, the output waveform of the AWG is amplified by several amplifiers, such as a MTC5515. The amplification and the amplitude of the modulation must be adapted as a function of the frequency of the modulation to reach a voltage near the V_π of the EOM, 4.5 Vpp. In this case for instance, as shown in Table 2 where one amplifier MTC5515 is used at the output of the AWG, the 4 GHz sinewave has been designed with an amplitude of ± 0.3 V to reach an amplified output of 3.95 Vpp. A safety buffer of 0.5 V has always been kept to remain around 4 Vpp and not go over 4.5 Vpp. The direct current applied to the EOM must also be adjusted to observe a modulation.

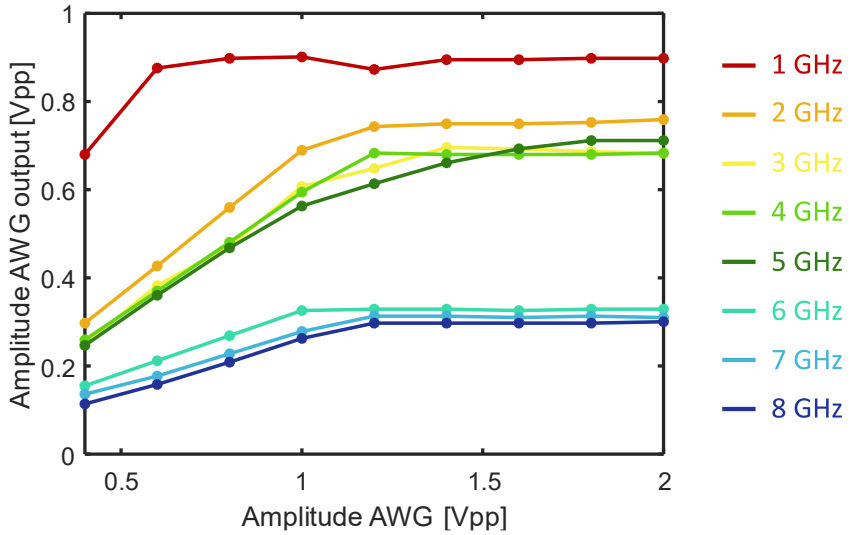

Figure 31. Evolution of the actual measured output waveform's amplitude of the AWG as a function of amplitude defined in the AWG depending on its frequency.

Table 2. Definition of the usable amplitude settings depending on the frequency of the modulation signal. The two first columns represent the setting entered in the AWG. The third column, "Amplitude output" shows the actual measured output of the AWG, amplified by a MTC5515, and attenuated by a 10 dB attenuator for safety. The fourth column calculates back what would be the amplified output amplitude without the 10 dB attenuator. The last column on the right defines which amplitude can be used with which frequency.

Frequency (GHz)	Amplitude (V)	V_2: Amplitude output with -10 dB (V)	Amplitude output without attenuator (V): $V = V_2 \cdot 10^{\frac{10}{20}}$	Settings
4	± 0,2	0,885	2,8	
4	± 0,3	1,25	3,95	✓
1	± 0,2	1,21	3,83	✓
1	± 0,25	1,49	4,71	
0.40	± 0,21	1,26	3,98	✓
0.40	± 0,22	1,32	4,17	
0.040	± 0,17	1,297	4,1	✓
0.040	± 0,18	1,36	4,3	

3.2.1.2. Dispersion measurement

The ring laser is tuned over a bandwidth of 100 nm around 1080 nm by rotating the diffraction grating. For each wavelength, a reference measurement, and a measurement of the fiber of interest are acquired in parallel as shown in Figure 32.

The signal is low pass filtered and a 10-times spline interpolation is used to increase the number of data points. A first coarse estimation of the time delay is determined by placing two markers on the first pulse of each signal, as shown in Figure 32. The length of the modulation is indicated by a third marker placed on the second pulse after the sinewave of the reference data. The sine burst is then cropped out of both signals. A cross-correlation algorithm is applied afterward for a precise calculation of the coarse alignment error. Finally, both values are added to give the total delay. Special emphasis should be placed on the formatting of saved data for future processing. In the case of shorter fiber lengths, failing to consider an adequate number of figures may result in rounded-up final values, potentially leading to inaccurate information. This process is realized for every wavelength and all upcoming datasets. The post-processing has been automated to accelerate analysis. The three markers are set once, at one wavelength, for a full set of measurements. Typically, data gathered at the midpoint of the bandwidth, around 1080 nm, is employed for markers' positioning. This choice is motivated by two factors. Firstly, it optimizes the signal-to-noise ratio, as less loss and more power are concentrated within this central range of the gain bandwidth. Secondly, the delay linked to this central wavelength falls within the midpoint of the dispersion curve. This ensures the markers' position to remain reasonably close to each pulse, even for the most distant wavelength.

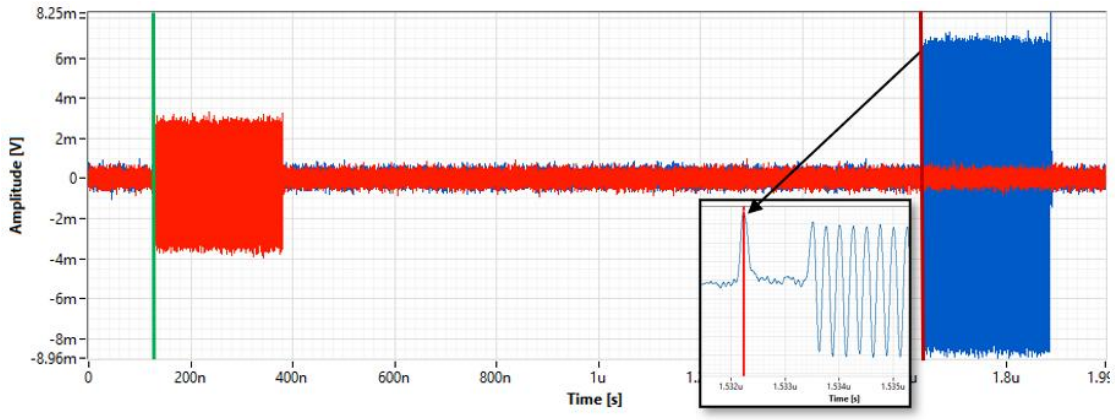

Figure 32. Acquired data after low pass filtering, 10 times interpolation, and mean subtraction at 27°C with 307 m of Hi1060 fiber at 1094.78 nm. The red and blue datasets represent respectively the reference (red) and the sample path (blue). The green and dark red markers are placed at the beginning of each signal, on the first pulse, as shown in the inset: zoomed area around the start of the modulated signal in the sample arm.

Since a time-delay measurement at one wavelength takes about one minute, the temperature of the fiber spool may shift during a set of measurements. The warm exhaust air from the measuring devices should be discharged in such a way that it does not heat up the measurement setup. To observe the behavior of the temperature, the time delay is first measured by tuning the ring laser from short to long wavelengths (forward direction) and afterwards from long to short wavelengths (backward direction). This gives a time difference between the measurement series of about 5 min. These results are then fitted by a 2nd-order polynomial such that $a_2x^2 + b_2x + c_2$. The linear coefficient a_1 of the fit is determined with a 2nd-order Taylor expansion performed at the center wavelength of a set of measurements. Once all coefficients are defined, D_1 and D_2 can be calculated with the following:

$$D_1 = \frac{a_1 \cdot n}{c \cdot T_{AVG}} \tag{36}$$

$$D_2 = \frac{a_2 \cdot n}{c \cdot T_{AVG}} \tag{37}$$

With T_{AVG} the average of all time delays of one set of measurements.

The standard deviation (STD) of a series of values is calculated after removing the 1st, 2nd, and 3rd order. This value will give information on the quality of the last series of measurements. A short 1 m fiber and a long 307 m fiber are used to evaluate the limits of the measurement technique.

For a 1 m Hi1060 fiber, the group delay's standard deviation for a set of 14 measurements between 1036 nm and 1121 nm goes down to 54 fs. For a set of 18 measurements between 1038 nm and 1127 nm, a 307 m Hi1060 fiber spool induces a group delay's standard deviation of 414 fs. The higher STD can be explained by an increased influence of temperature and lower signal-to-noise ratio when using longer fibers. However, with longer fibers, chromatic dispersion has a greater impact on the delay, increasing the accuracy of the measurement. Nevertheless, a shift of 0.01 nm in wavelength will impact the time delay by 104 fs with a fiber spool of 307 m, while

with a 1 m fiber, the impact is in the order of 0.1 fs. Thus, the longer the fiber is, the more accurately the wavelength should be measured. It confirms that the accuracy of the measurement of long fiber lengths is limited by the resolution of the wavelength measurement and not the time delay measurement.

This time delay performance enables an accurate chromatic dispersion measurement in optical fibers. D_1 measured at 1080 ± 50 nm equals -33.697 ± 0.698 ps/nm/km and, D_2 equals 0.075 ± 0.003 ps/nm^2/km. The results obtained at 850 ± 15 nm can be seen in Table 3. The 610 m of 780-OCT fiber introduces a comparable STD to the one obtained around 1080 nm. However, the low signal-to-noise ratio, due to less performant components, limits the measurements' quality.

Table 3. The table presents in its first part the 1st order and 2nd order chromatic dispersion of different fibers at several wavelengths. Secondly it shows the group delay's standard deviation and time delay caused by a measurement error in wavelength for different lengths of fiber.

Wavelength nm	**1st order dispersion ps/nm/km**	**STD**	**2nd order dispersion ps/nm²/km**	**STD**	**3rd order dispersion ps/nm³/km**	**STD**
1190 ± 45	-20.606	0.789	0.052	0.002	-	-
1080 ± 50	-33.697	0.698	0.075	0.0026	$-1.14.10^{-4}$	$5.44.10^{-5}$
850 ± 15	-100.186	0.526	0.209	0.031	$-2.4.10^{-3}$	654.10^{-6}

	1 m Hi1060	**307 m Hi1060**	**610 m 780-OCT**
Group delay's STD	54 fs	414 fs	320 fs
0.01 nm impact	0.1 fs	104 fs	614 fs

The time delay measurements around 1190 nm and 1080 nm have been realized with the same fiber spool but with two different setups. However, a comparison can be made between these two graphs, see Figure 33. The setup used in this study can be adapted to any wavelength. Furthermore, a broader tunable source would enable the dispersion analysis of optical fibers over a wider range.

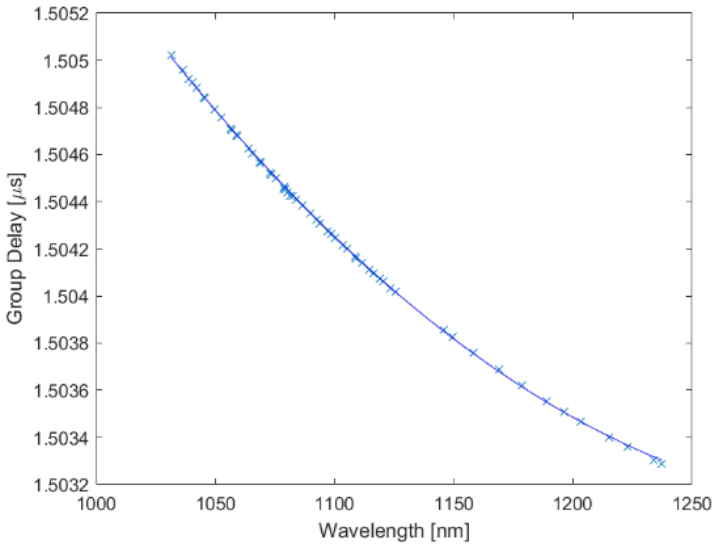

Figure 33. Dispersion measurement, i.e. group delay measurement realized with a 1080 nm and an 1190 nm system using the same fiber of interest, 307 m of Hi1060.

In addition, it has been noted that chromatic dispersion cannot be measured in a 1 m fiber. Indeed, the linear dispersion in Hi1060 fiber at 1080 nm is according to our data processing, - 33.697 ps/nm/km. Thus, to be able to measure the dispersion in a 1 m fiber length, a system with a minimum resolution of 30 fs/nm should be sufficient. Having a 1 m fiber length, a group delay's STD of 54 fs with a 100 nm tunable laser should allow to measure this resolution. However, 1 m and 2 m fiber lengths measurements could not be achieved reliably. A wrong dispersion value D_1 of -26.614 ps/nm/km and a dispersion slope D_2 of 0.326 ps/nm²/km for a length of 2 m was measured. For 1 m, the incorrect value D_1 = - 7.512 ps/nm/km and D_2 = 0.088 ps/nm²/km was measured. Down to this precision, many different factors impact the measurement. For instance, special attention should be paid to the fiber length connection of the reference and sample arm to each photodiode. The same regarding the length of the SMA cable linking the photodiode to the oscilloscope. The temperature that might also have a substantial impact on chromatic dispersion is investigated in the following paragraphs.

3.2.1.3. Influence of temperature

The fiber of interest is placed, as mentioned above, in a thermally insulated box to control its temperature. Depending on the experiments, the temperature is set either to 27°C or 30°C. All measurements are taken 1 hour after the temperature stabilization in the insulated box to ensure that the entire fiber spool is at the target temperature. All other components are not placed in this box due to impracticability, which might impact further short fiber measurements. Several measurements were taken at 27°C and 30°C to compare the influences of the temperature on D_1 and D_2.

According to Yang & al. [159], the refractive index of Hi1060 fiber changes by $1.178.10^{-5}°C^{-1}$. Thus, for a shift of 3°C and a fiber spool of 306.789 m, a time shift of 53.162 ps will be observed.

The experiment at 30°C and 27°C shown in Figure 34 resulted in 66.479 ps. Both values are in the same order of magnitude within a factor of 1.25. Nevertheless, a change of 1°C in 1 m of fiber will impact the time delay by 131 fs. Thus, some uncertainty remains due to the inability to control all components' temperature. Indeed, thanks to the forward and backward measurement technique, a slight temperature shift during each series can be observed with the second-order dispersion. Some examples are circled in red in Figure 34. An ideal dispersion measurement setup would be fully temperature controlled, from the tunable ring laser to the photodiodes.

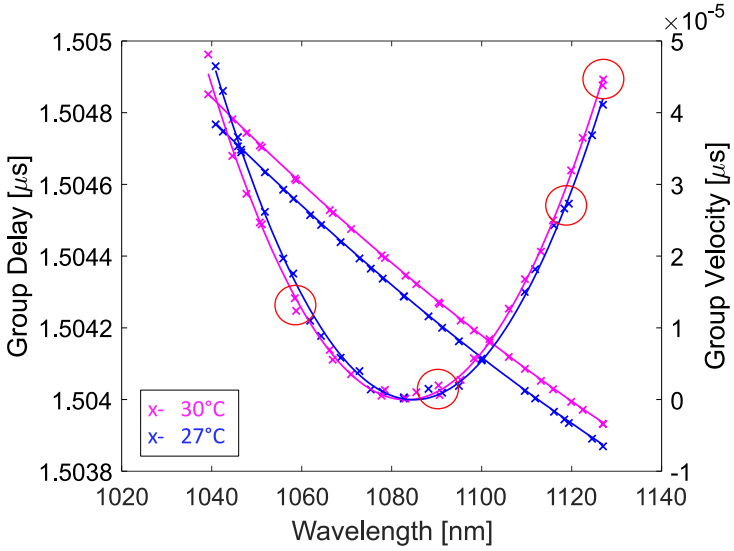

Figure 34. Representation of the 1st and 2nd order dispersion at 27°C and 30°C – backward and forward measurements. The red circles indicate a temperature shift during each series of measurements.

Five group delay measurements were taken at 2-minute intervals at the same wavelength to study the reliability of the setup. A standard deviation of 461 fs over the five measurements has been observed. Wavelength drifting and temperature changes can decrease the accuracy of each measurement and the data processing. Nonetheless, this result remains accurate enough to precisely determine the chromatic dispersion of medium-length optical fibers, from a few meters.

3.2.1.4. Cost effective solution

In view of a more cost-effective setup, lower frequency modulation has been used as well as lower performant equipment. The analog bandwidth of the DSO was reduced to 1 GHz and the sampling rate to 20 GS/s for this purpose (mimicking a more affordable oscilloscope), as shown in Table 4.

Table 4. 1st and 2nd order chromatic dispersion measured with 4 different modulation frequency, 4 GHz, 1 GHz, 400 MHz and 40 MHz. For the three lower frequencies, the acquisition frequency and sampling rate were reduced.

Frequency	4 GHz	1 GHz	400 MHz	40 MHz
STD	17 ps	16 ps	79 ps	4 ns
DSO frequency	63 GHz	1 GHz	1 GHz	1 GHz
DSO sampling rate	80 GS/s	20 GS/s	20 GS/s	20 GS/s
1st order	-34.5	-34.4	-32.9	-65.7
2nd order	0.081	0.075	0.19	-1.24

It has been observed that a 1 GHz modulation is precise enough to obtain the same standard deviation in regard to the 1st and 2nd-order dispersion with a group delay standard deviation of ± 1.227 ps. However, the accuracy is not high enough to recognize any 3rd-order dispersion as shown in Figure 35. Figure 35 also shows that at 400 MHz even the 2nd-order cannot be determined accurately, however, the precision of the time delay measurement is enough to have an approximation of the group delay with an accuracy of ± 15.262 ps.

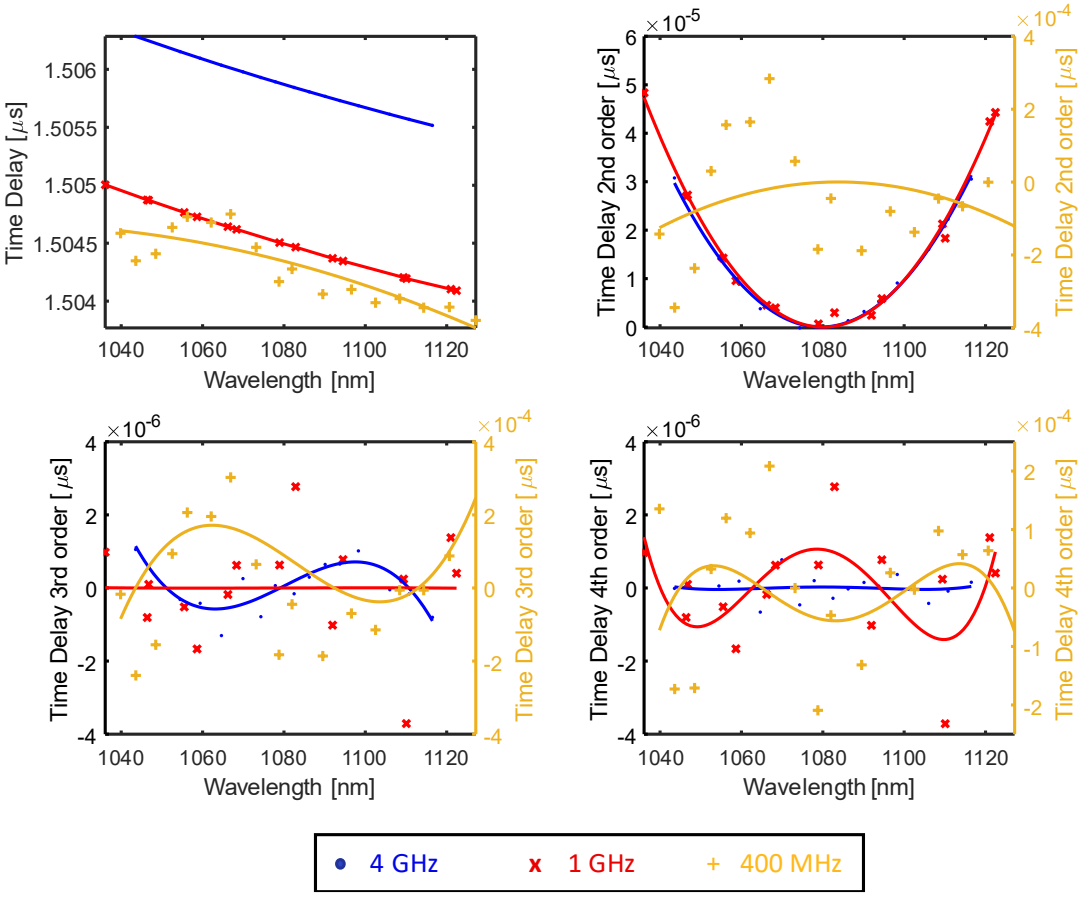

Figure 35. Dispersion measurements acquired with a 307 m Hi1060 fiber spool at 3 different frequency: 4 GHz, 1GHz and 400 MHz. The 1st, 2nd, 3rd and 4th order of dispersions are presented. The right y-axis, highlighted in yellow, is used to display the data acquired at a frequency of 400 MHz. This allows for a clearer comparison by plotting it alongside the other frequency data on the same graph, despite the differences in scale.

Regarding the 40 MHz sinewave modulation, different datasets have been acquired with two different photodiodes. Figure 36 shows 3 sets of data points, black (slow PD, 150 MHz PDB150C, Thorlabs), red (forward, fast PD, 350 MHz PDB130C Thorlabs) and blue (backward, fast PD). Data acquired with the fast photodiode can be separated into 3 different sets of data and fitted with three distinct green dotted lines, each separated by about 4.5 ns. The upper line grouping the more datasets presents a group delay standard deviation of 39.9 ps. Black points can also be fitted with two distinct orange full lines. The second fit gives a group delay standard deviation of 479 ps. The factor > 10 separating measurements done with fast and slow PD induces the necessity of using fast photodiodes for all measurements. Even though the modulation frequency is well below

the RF bandwidth of the photodiodes, employing faster photodiodes enhances information acquisition, leading to heightened accuracy in the cross-correlation step.

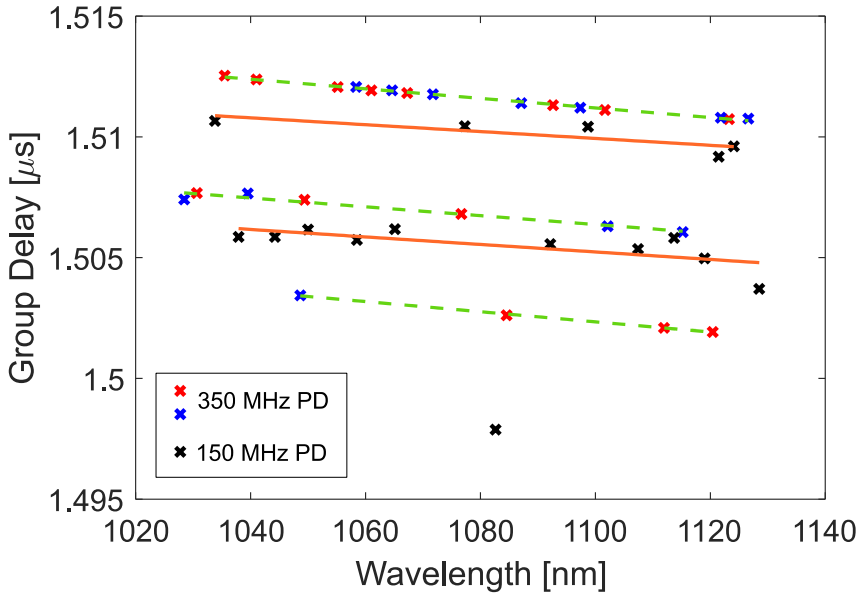

Figure 36. Three series of dispersion measurements were realized at 40 MHz with a 307 m FOI. The blue and red series were realized with the fast PDs. These two series show a shift of the time delay which can be separated by three different green dotted linear lines. The black series was measured with the slow PD. Each series includes forward and backward measurements.

3.2.1.5. Data processing robustness

Lastly, the robustness of the processing steps is evaluated. Therefore, the fiber of interest is replaced by a free space beam path to exclude the effects of chromatic dispersion and have an accurate method to change time delay values. The length of the free space was first changed in steps of 0.1 mm to see if the algorithm could detect them. An accuracy down to 385 fs is achieved with a slope of 3.238 ps/mm, as shown in Figure 37 right (red). A change of 0.1 mm in air should increase the time delay by 333 fs, here it is increasing by 323.8 fs. The difference of 10 fs corresponds to about 3 µm, which is a fair approximation when setting the delay by hand. The standard deviation almost doubles up to 663 fs when changing the steps by 1 mm, Figure 37 left (red). The accuracy of introducing the correct delay through free space decreases proportionally with greater distances, providing a possible explanation. Also, when having steps of 0.1 mm a total distance of 2 mm is covered when 15 mm is covered with steps of 1 mm. Any angle present in the stage will have more impact on the delay introduced when travelling longer distances.

When adding the fiber spool, used earlier for chromatic dispersion measurement, the standard deviation increases from 385 fs to 723 fs in case of the 0.1 mm steps, and from 663 fs to 855 fs from the 1 mm steps measurements, blue markers in Figure 37. These show the impacts of the length of the spool on the measurement. Temperature might be one of the most impacting factors along with a drift of the wavelength during one set of measurements. However, in both cases, the

software enables to detect a time shift introduced by a 0.1 mm delay with a femtosecond accuracy. Another phase-shift algorithm such as the Hilbert function could be tried to confirm the results.

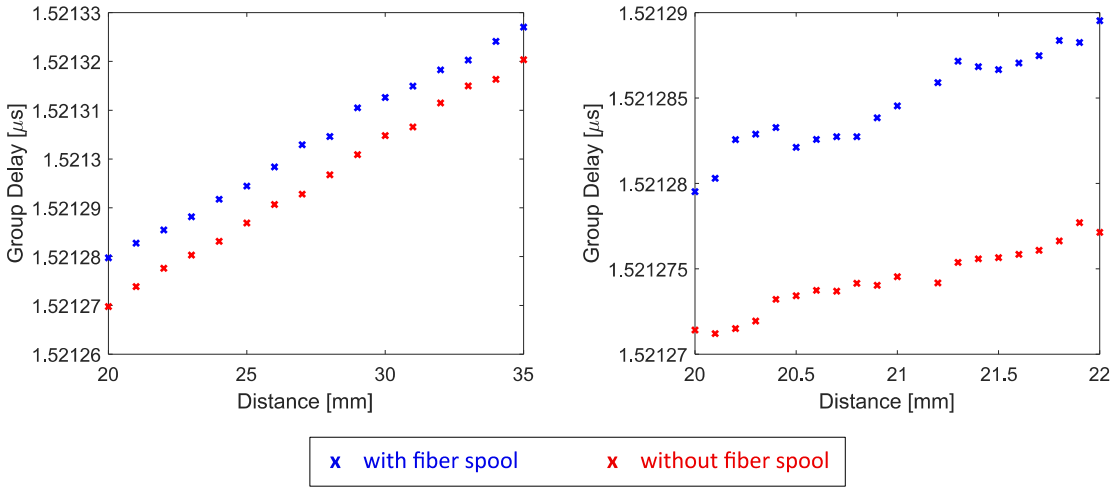

Figure 37. Accuracy measurements, measured on the left every 1 mm step and every 0.1 mm step on the right. The delay between both colors has been changed by a constant value to enable the plotting of both curve, with fiber spool (blue) and without (red) on the same plot.

On the other hand, the cross-correlation is highly impacted by the position of the cursors during post-processing. If the same data are processed twice with different marker positions, the results will not be identical. The behavior of the cross-correlation is even more interesting since the position of each cursor does not impact the data processing in the same way. Regarding the left cursor of the reference signal (green cursor in Figure 32), when moving it forward or backward rapport to the first pulse, for all wavelengths the same positive or negative shift of a few femtoseconds respectively is observed. Figure 38 shows this in both graphs. It highlights the differences between the post-processed data for the optimal cursor position and the same data post-processed with the shifted cursor positions. These data have been acquired using the 307 m Hi1060 fiber spool. If the cursor is placed a bit on the right of the pulse (after the peak of the pulse), the main delay measured with the markers will experience a decrease, and vice versa. The cross-correlation will try to compensate for it; however, it cannot compensate for all the different delays introduced by the wrong position of the markers. Another point can be discussed in Figure 38. During the post-processing, all three cursors are positioned on a reference dataset acquired at one wavelength. All other datasets are themselves post-processed with the position of these reference cursors. The two graphs in Figure 38 illustrate the impact of selecting the reference wavelength. The reference wavelength is on the left side, 1092.32 nm, and on the right, 1031.36 nm, as represented by two green markers. It is shown that from the point where the reference value is selected, the wavelength higher than this one will experience almost the same increase or decrease of delay. Data acquired at wavelengths lower than the reference experience higher fluctuation.

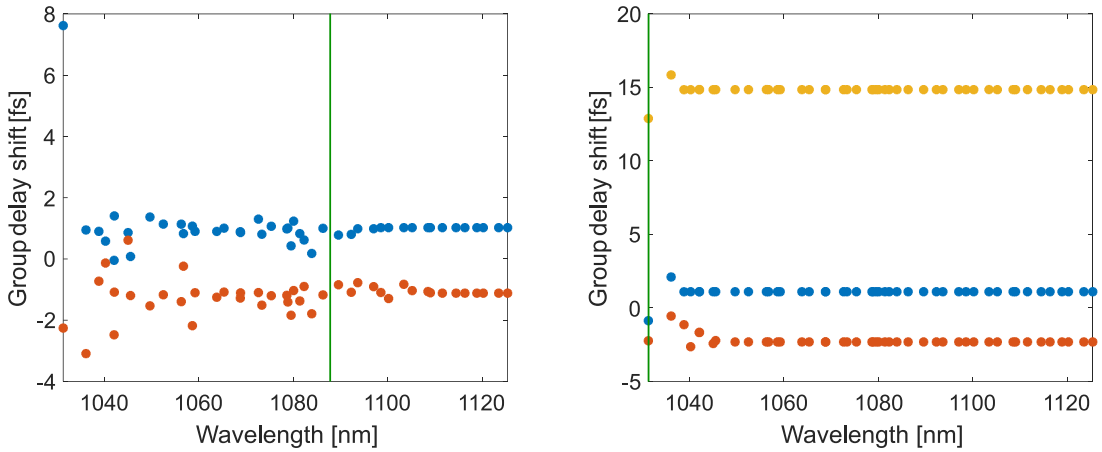

Figure 38. The left data have been post-processed with a reference wavelength of 1092.32 nm and the right data at 1031.36 nm, as indicated in both graphs by the green cursor. The five data sets represent the difference in group delay between a dataset processed with precise positioning of the reference left marker and the same dataset processed with different reference marker shifts, either before or after the first reference pulse of the modulation.

Both other cursors, the one placed on the pulse of the reference signal after the sinusoidal modulation and the one placed on the first pulse of the sample data impact the group delay at a picosecond level. This confirms that a modulation, composed of two pulses and the sine wave, is well thought out as the markers can be precisely positioned. The markers' position must then be as precisely set as possible for group delay measurements. However, when measuring chromatic dispersion in long fiber length, around 300 meters, the impact of the markers' position is minimal, only about 0.1%.

Combining a time-of-flight measurement with a cross-correlation algorithm enables high-accuracy chromatic dispersion measurement for optical fiber longer than 2 m. One of the most limiting factors is the wavelength measurement which is limited by the resolution of the OSA. Also, the temperature of the fiber must be controlled and stabilized precisely to exclude any impacts on the group delay measurements. Each of the mentioned issues does not directly impact the 1st and 2nd-order dispersion, but the combination of all may distort the results. Automating the entire process could speed up the measurement, reducing the temperature impact and leading to a less time-consuming measurement.

Moreover, depending on the accuracy required, the modulation frequency can be adapted to a certain point. A frequency of 400 MHz will provide enough accuracy to obtain a reliable 1st-order dispersion. Thus, more cost-effective equipment can be used. However, a 1 GHz modulation is the lower limit for an accurate group delay measurement. With increasing modulation frequency, a more precise estimation of chromatic dispersion can be achieved. In case dispersion measurements are carried out to obtain the necessary design parameters to custom manufacture cFBGs, a modulation of 4 GHz is advisable.

Despite the uncertainty mentioned above, the system shows improved accuracy compared to other methods presented in section 2.3.4 and can be easily adapted to different wavelengths. The

chromatic dispersion values gathered with the 850 ± 15 nm setup facilitated the ordering of three cFBGs for the future 850 nm FDML laser setup (section 3.3).

cFBGs are usually characterized by checking their bandwidth, reflection properties, and chromatic dispersion compensation. This was done with the previous 24 nm wide cFBGs but not with the 72 nm one due to the unavailability of the above-mentioned material during the project phase. Figure 39 shows the dispersion measurements carried out on a cFBG as a sample using a circulator in blue and a fiber spool of 480 m in red. The value acquired the closest to 840 nm has been set to zero to enable comparison on the same figure. The 1st and 2nd order are presented. The first order can be compensated precisely with a fiber spool of 480 m due to the close compensation. However, the second order won't be compensated for by this fiber length. The fact that the cFBG compensates for 480 m of fiber and not 500 m can be due to several factors. During this measurement, neither the cFBG nor the fiber spool were temperature controlled, which impacts slightly the measurement. In addition, there was no quality check performed by the manufacturer leading to potential undesired manufacturing uncertainties.

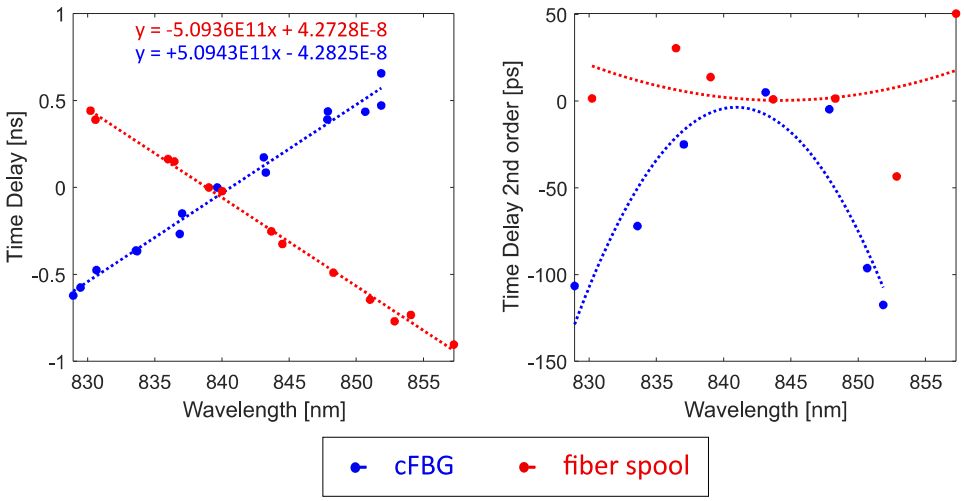

Figure 39. Dispersion measurements were realized around 850 nm on a cFBG (blue) and a fiber spool of 480 m (red). Their 1st and 2nd order are presented.

Once the characterization of the cFBG was done and the FDML built following Figure 29, another challenge arose. Circulators introduce a significant amount of PMD, observed as ripples in Figure 27 (A) and in Figure 28. Additionally, from these two figures, it can be seen that wider bandwidths make achieving a ripple-free spectrum more challenging, while higher gain lessens their impact. This challenge is addressed in the next section.

3.2.2. Study of the polarization mode dispersion in the laser

[The work presented in this section has already been published in 2023 at the Photonics West conference [158]. Most of the sentences, paragraphs and figures are taken from it.]

As mentioned earlier in the theory, light propagates in a single fundamental mode having two orthogonal polarizations states. If both travel at different speed due to birefringence, PMD occurs. For instance, a circularly polarized light in optical fiber can become elliptical. Here, the observed PMD is due to circulators. In circulators both axes of the light are split and recombined. If both paths experience a different length, PMD will be observed. It will introduce several phenomena in the laser, like polarization-dependent loss and ripples. On one hand, the polarization will deteriorate the output signal, not having the same amplification over the spectrum, on the other hand it might create ghost images while doing OCT. Therefore, the time delay between the fast and slow axis of the light must be compensated to achieve a PMD free spectrum, and OCT images.

In general, compensation should be possible, however, it is not clear to which degree PMD caused by circulators and cFBGs can be compensated for. To further investigate and quantify its contributions of the individual components in the FDML laser, a test system has been set up. Its layout and all results are presented in the following. Two techniques of PMD compensation are evaluated, starting with a custom designed polarization controller, followed by the use of polarization maintaining components.

3.2.2.1. Observation of the PMD

The system consists of an SOA used as light source, a circulator and a cFBG – which were spliced due to their use in the laser, a separation was not desirable – and a polarizer as shown in Figure 40. To quantify the polarization dependent path length differences of each device, the spectral separations of the modulation in the output spectrum were measured using an optical spectrum analyzer. The system on the left, (A), was used to study the circulator's PMD, and the one on the right, (B), the impact of the cFBG on the PMD introduced by the circulators.

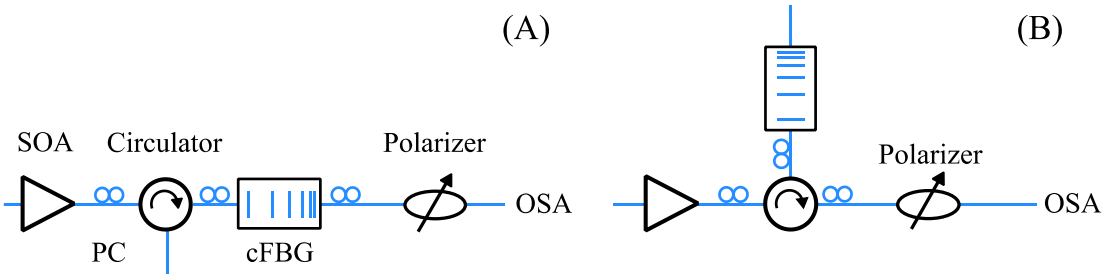

Figure 40. Diagrams of the PMD measurement setup with different devices under test. SOA: semiconductor optical amplifier, PC: Polarization controller, cFBG: chirped fiber Bragg grating, OSA: optical spectrum analyzer.

Figure 41 (A) shows the output of setup (A) in Figure 40. It shows that it is possible to approach the right polarization states to almost completely suppress the PMD of one pass through the circulator. This is achieved by aligning the almost linearly polarized emission of the SOA to one main axis of the birefringence crystal in the circulator using polarization controllers ahead of it.

It is not easily possible to measure the PMD of the light within the FDML cavity after each component as this would necessarily cause further losses by adding optical couplers. However, it

should be possible to compensate for the PMD introduced by individual passes through a circulator to a certain degree since the spectral modulation in Figure 41 (A) is similar for two additional circulators which are used in the final FDML cavity design later. Thus, additional polarization controllers are placed in the laser in front of each circulator's input, allowing to prevent or cancel out PMD contributions, as shown in Figure 29. A 50 nm wide spectrum has been acquired with this new conformation, as shown in Figure 41 (B). However, a hypothesis has been raised, that the PMD here is wavelength-dependent, and these could arise from the reflection of the cFBG. Indeed, the frequency and pattern of the PMD at the output of the laser differ along the spectrum despite the presence of polarization controllers. The setup present in Figure 40 (B) has then been built and results are presented in Figure 41 (C). When looking at the output of the cFBG, the orange graph is acquired. The orientation of the polarization controller is optimized to achieve this ripple-free spectrum. When the light is reflected by the cFBG and travelled a second time in the circulator, here the PMD cannot be fully compensated over the entire spectrum. Ripples can only be suppressed in a narrow ~3 nm section of the entire spectrum with increasing ripple intensity towards shorter and longer wavelengths. Each wavelength is reflected at the cFBG with a different polarization state which makes its compensation more complex. The part of the spectrum without ripples becomes narrower for every pass through each of the circulators. To achieve a ripple-free section in the output spectrum, each circulator pass must be polarization-optimized for the same spectral section which is not trivial. Ripples can be suppressed but will not vanish. Some PMD experiments presented in the next sections have been performed to achieve better PMD suppression.

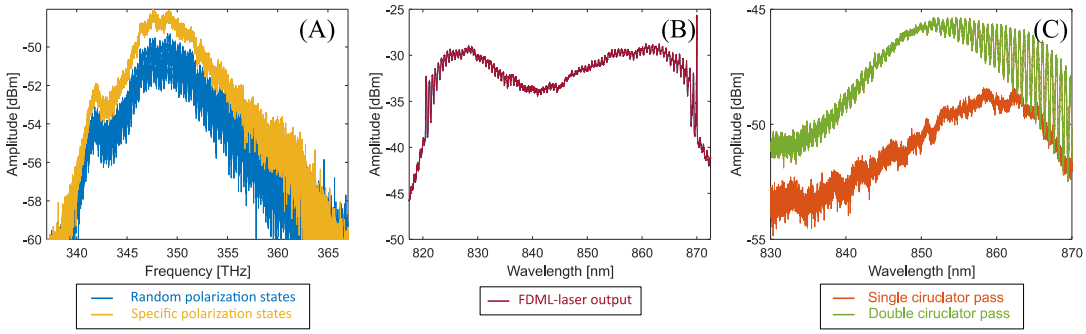

Figure 41. (A) PMD suppression using setup (A) in Figure 40, the yellow curve corresponds to an optimized polarization state while the blue one is non-optimized. (B) Output of the FDML laser having polarization controller at each input of the circulators. (C) PMD suppression using setup (B) in Figure 40, the orange curve corresponds to the output of the cFBG while the green one shows the output 3 of the circulator, after reflection in the cFBG.

3.2.2.2. Custom polarization controller

An option of compensation is to create a custom polarization controller, being able to compensate for the delay between the slow and the fast axis introduced by the circulators itself. According to Figure 43 (A), where high PMD is generated using the setup presented in Figure 40 (A), the frequency of the ripples average to 249 GHz which corresponds to a delay of 972 λ between fast and slow axis. The delay is calculated as shown in Figure 42.

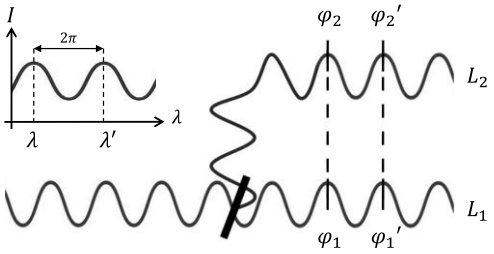

$$\varphi_2 - \varphi_1 = \frac{2\pi n}{\lambda}(L_2 - L_1) \quad \text{and} \quad \varphi_2' - \varphi_1' = \frac{2\pi n}{\lambda'}(L_2' - L_1')$$

Two successive maxima are separated by 2π, hence

$$\frac{2\pi n}{\lambda}(L_2 - L_1) - \frac{2\pi n}{\lambda'}(L_2' - L_1') = 2\pi$$

Where $\Delta L = L_2 - L_1 = L_2' - L_1'$

$$\Delta L = \frac{\lambda'}{n(\lambda' - \lambda)} \cdot \lambda \quad \Rightarrow \quad \boxed{\Delta L = 972 \cdot \lambda}$$

Figure 42. PMD delay calculation. Two successive maxima of the PMD ripples are separated by 2π, or 249 GHz in this case. They correspond to different wavelengths λ and λ'. A wave with a specific frequency is split into 2 paths with two different lengths: L_1 and L_2 creating a delay ΔL. At two different points, the wave has different phases φ as indicated on the left drawing. Using the formula of phase difference, the delay is calculated as shown on the right.

According to Equation (38), where Φ is the retardance, N the number of loops for a controller, *a* the constant for silica fiber: 0.133, d the fiber cladding diameter 125 µm, λ = 850 nm and D = 27 mm the size of the loop, a polarization controller of 3,403 loops of a diameter of 27 mm should help to partly compensate for this delay. Which corresponds to 288 meters of optical fiber.

$$\phi(Waves) = \frac{\pi\, a\, N\, d^2}{\lambda D} \tag{38}$$

However, to be able to compensate the PMD with one high order waveplate, the absolute retardance measured in optical path length should exhibit no wavelength dependence. This means that the fringe frequency must be constant over the spectrum. The frequency of the PMD is then determined in four regions of the spectrum, blue, orange, yellow and purple. Figure 43 (A) shows a difference of 3 GHz in the PMD frequency over the range, which corresponds to a phase shift of 0.07 rad which can be considered acceptable. However, the PMD highly becomes wavelength dependent when introducing a cFBG as shown in the previous section. A higher order waveplate has still been tried to see if it has any impact on the PMD. Plot Figure 43 (B) shows the output of the systems of Figure 40 (B), with the addition of a polarization controller having 20 and 5 loops with a diameter of 18 mm. This specific polarization controller has been added to the FDML laser between the circulator and the cFBG placed ahead of the SOA, as shown later in Figure 49. The spectrum in Figure 43 (C) has been acquired at the laser's output. PMD remains but its suppression is manageable, leading to a flatter spectrum compared to Figure 41 (B).

As illustrated in Figure 43 (C), it is possible to obtain a near top-hat spectrum of the 850 nm FDML laser output with a FWHM bandwidth of ~50 nm. Ensuring an almost perfect top-hat spectrum requires a minimum of one hour to calibrate the polarization controller, which is not practical. Another method using a PM-780 patch cord is described in the next section. The 20-loop and 5-loop polarization controller is kept in the system.

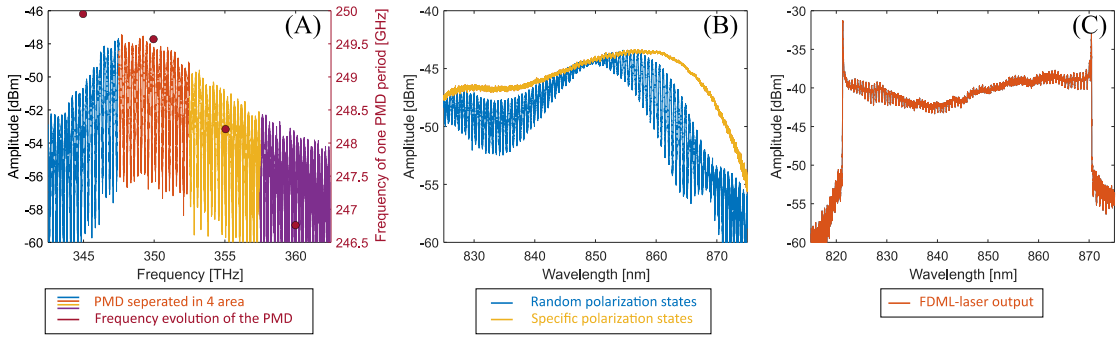

Figure 43. (A) Study of the PMD frequency evolution in four sections along the spectrum. (B) PMD suppression with the addition of a 20x5 polarization controller, showing a wavelength-dependency after the cFBG. (C) Output of the FDML laser having a 20x5 polarization controller added.

3.2.2.3. Addition of a polarization maintaining component

The first idea here was to introduce a polarizer, which would cancel one of the light axis, hence cancel all PMD. It was placed in the first hand before the SOA and on the second hand, it has been placed after the SOA. Unfortunately, in both cases no improvement was observed. It is mainly introducing losses in the laser which is not desirable due to the low gain of the SOA. Secondly, the beating frequency of the length of the PM fiber of the polarizer does not match the frequency of the PMD introduced by the circulator, which introduces another PMD frequency, which makes it even harder to compensate.

The second idea is then to match the beating frequency of a PM-Patchcord with the PMD frequency to compensate for it. For this, a 2.9 m PM-Patchcord has been added to the laser at the input of the SOA. Neither compensation nor amplification of the PMD was noticed, as shown in Figure 44 (A). Out of curiosity, a 4-meter patchcord has been added instead of the 2.9-meter one, results are in plot (B) below. The laser is still lasing, however, the presence of previously unseen intensity dips in the spectrum are a notable anomaly. It is conceivable that they may be attributed to variations in the frequency of PMD, resulting in unforeseen and erratic behavior that proves challenging to rectify.

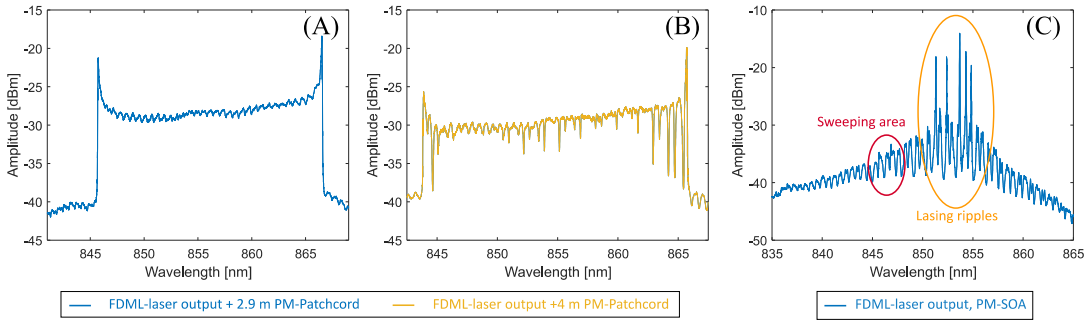

Figure 44. FDML laser output with (A) a 2.9-meter PM-Patchcord, (B) a 4-meter PM-Patchcord and, (C) using a PM-SOA.

Finally, a new SOA provided by Superlum Ltd. with PM-fiber has been tried out, Figure 44 (C). The losses incurred by employing a PM-SOA, coupled with the presence of ripples, hinder the attainment of a sweeping lasing spectrum. As depicted in Figure 44 (C), the sweeping range has

been shifted leftward to scrutinize the ripple patterns. It appears that the upper crests of the ripples initiate parasitic lasing, giving rise to these spikes. Concurrently, the segment intended for amplification within the sweeping range remains largely unaffected by the gain medium. Following exhaustive testing, it has been concluded that the incorporation of PM components is not advisable for this laser system. This is primarily due to the introduction of losses and the absence of effective PMD compensation. The same issue would be introduced by for instance using polarizing-fibers or PM-circulators. The PMD must vanish, but high losses might prevent lasing.

To conclude, polarization controllers placed in front of each circulators' input are the best option to prevent or cancel out PMD contributions. However, given that PMD is contingent on temperature and the laser lacked temperature control at this stage, daily adjustments to the polarization were imperative for achieving optimal performance. Finally, an elevated small signal gain would aid in diminishing PMD, owing to the reduced sensitivity of the SOA to ripples stemming from the heightened gain. This is evaluated in the following two sections.

3.2.3. Comparison of FDML laser noise at 1300 nm and 850 nm

In this section, the impact of a higher gain on the noise of the laser is presented using a 1300 nm FDML laser followed by the same experiment on the 850 nm FDML laser. The 1300 nm laser is selected for its ability to fully leverage the potential of its SOA, unhindered by its COD limitations. Additionally, it boasts a higher small signal gain than 850 nm, approximately 30 dB. For both lasers, the direct output signal using various driving currents of the SOAs is acquired. This enables the observation of how the noise evolves in relation to the amplification level.

For this, the direct output signal of the 1300 nm laser and the 850 nm laser are acquired using a 50 GHz (Finisar, XPDV2320R) and a 30 GHz (Thorlabs, DMX30AF), respectively. Both photodiodes are connected to an 80 GS/s DSO (Keysight, DSOZ634A). The 1300 nm FDML laser is driven at 418 480.79 Hz. A narrow sweeping range of 18 nm is used to mimic the narrow bandwidth of the first 850 nm laser developed, which is, in this case, 23 nm, limited by the used cFBG. The 850 nm FDML laser swept at a repetition rate of 411 782.97 Hz. Both lasers are not modulated, four forward and four backward sweeps can be observed in each subset of Figure 45.

The 850 nm laser shows high intensity noise over its entire spectrum. Also, a non-lasing zone at one turning point of the filter can be seen. This can also be observed in Figure 27 where the right part of the spectrum is not lasing due to the amplitude of the filter going further than the bandwidth of the cFBG. It can also be noticed that less noise is present at the other turning point, where the amplitude of the signal is the highest. This is due to the shape of the gain medium of the SOA, higher amplification is present around 820 nm. Figure 27 also shows this. Between the right and the left of the spectrum, the output of the laser presents a difference in power of at least 5 dB which impacts here the noise. The maximum current used here, 183.8 mA, is defined by the COD of the SOA. The maximum usable driving current of the SOA is in theory 200 mA.

The 1300 nm laser shows full lasing over its entire spectrum. However, like the 850 nm laser, one turning point has lower intensity compared to the other one at low current level. This difference is also noticeable at higher current levels even if it appears smaller because of the difference in scale. Measurements are carried out at low current levels, mimicking the behavior of the 850 nm, and at maximum current, 700 mA, for comparison.

Both lasers demonstrate a reduction in noise as the driving current of their SOAs increases. While some noise persists near the filter's turning point, the linear region operates at sweet spot. Additionally, although the 1300 nm laser exhibits some holes, they are significantly fewer than those in the 850 nm laser.

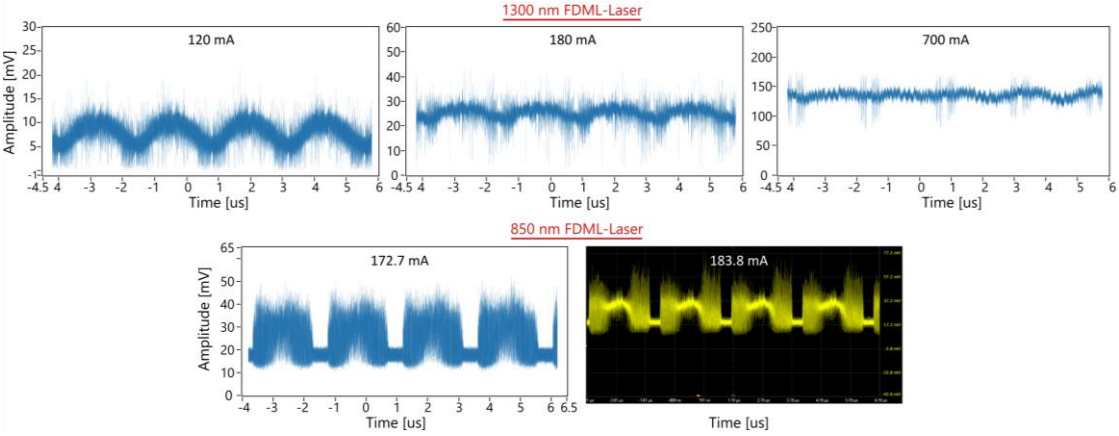

Figure 45. Direct output signal from a 1300 nm FDML laser and the 850 nm FDML laser. Different SOA currents are being used for both lasers.

This experiment shows that higher gain helps reaching sweet spot operation. For this purpose, a dual amplification FDML laser has been set up to achieve higher gain in the laser.

3.2.4. Dual amplification FDML laser

In view of increasing the gain in the laser, the FDML layout has been changed to achieve dual amplification in one round trip. The new laser is now composed of a ring on one side of the SOA, where the light will propagate through, be filtered and come back to the SOA. On the other side the light propagates through one fiber, is reflected by a cFBG and comes back by the same fiber to the SOA. The SOA is modulated with a duty cycle of 62.5 % so that when the sweep is coming back from the inside ring, the SOA is switched on for an initial amplification. The second amplification happens when the sweep is reflected by the cFBG (on the right side of the scheme in Figure 46 part 1), the SOA is switched on again. Inversely, it is switched off to prevent any parasitic lasing. Each length of fiber spools (FS) in area 1, 2 and 3 have been precisely calculated to obtain a round-trip time of about 2.4 µs with a sweep duty cycle of 25 % to allow a potential future optical buffering which would lead to a frequency of 1.6 MHz.

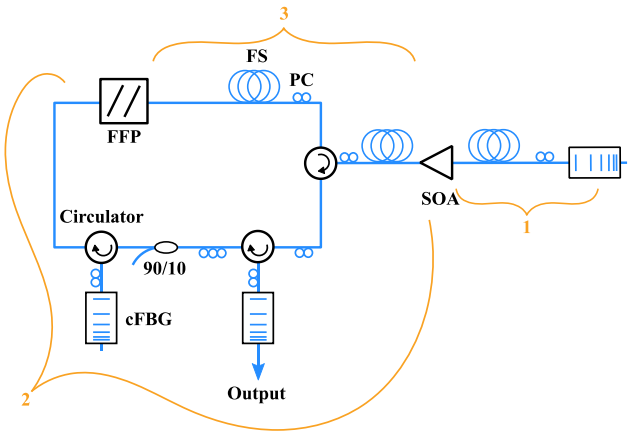

Figure 46. Dual amplification FDML laser setup. The SOA is modulated by 62.5 %. The length of part 1,2 and 3 are precisely calculated to achieve the amplification of the sweep at the right time while avoiding parasitic lasing. SOA: Semiconductor optical amplifier, cFBG: chirped fiber Bragg grating, FFP: fiber Fabry-Pérot, FS: fiber spool, PC: polarization controller.

One challenge with this configuration lies in identifying which segment of the filter sweep is being amplified. To isolate the linear portion of the sweep, various approaches can be employed. Initially, one can utilize the distinctive features, the edges with higher intensity present in a typical FDML laser output spectrum. The phase relationship between the SOA modulation and the sinewave driving the filter is fine-tuned, first towards the shorter wavelength edge and subsequently towards the longer one. Averaging these phases is likely to yield to the amplification of the linear portion of the sweep. Another viable method involves obtaining an interference pattern using, for instance, a MZI, and observing the phase evolution. If the phase exhibits symmetry and approaches linearity, it indicates that the phase selection is accurate. Also, when increasing the fringes frequency, if the sweep is linear, the modulation should vanish evenly over the entire spectrum when reaching the maximum bandwidth of the detector. If not linear, it will be more pronounced on one side. With these methods it can also be known which sweep, backward or forward are being amplified.

The bandwidth of the spectrum is restricted to 20 nm due to the COD threshold of the SOA. The gain decreases on the sides which does not enable lasing on a broader range. The spectrum in Figure 47 (A) has been achieved at less than half of the maximum current applicable, 90 mA, but the internal power was perilously close to the COD limit, 20 mW. The spectrum also shows a ripples-free-area over 15 nm, which confirms that higher gain enabled to cancel PMD introduced by circulators. The remaining chromatic dispersion in the laser is introducing noise on the shorter wavelength of the spectrum, where the frequency of the FFP is not adjusted for, as shown in Figure 47 (B), which degrades the SNR to 35 dB as shown in Figure 47 (C). Ripples due to PMD are also noticeable. Despite the last two, the dual-pass SOA FDML laser has a sensitivity roll-off of 6 dB at more than 1 cm delay as shown in Figure 47 (C). The roll-off and time trace of the laser were acquired using a Wieserlabs custom made balanced 600 MHz Silicon photodiode.

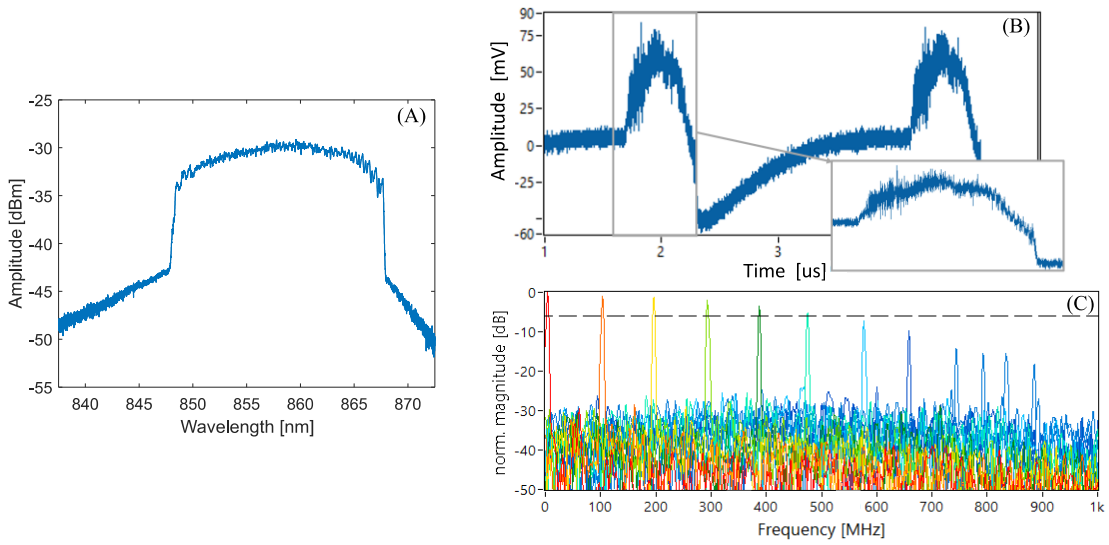

Figure 47. (A) Output spectrum of the dual-pass SOA FDML laser sweeping over 20 nm. (B) Time trace of 2 sweeps at the output of the laser, inset: zoom into the noise evolution along one sweep. (C) Sensitivity roll-off of more than 1 cm at -6 dB, steps of 2 mm for the first 8 peaks, followed by 1 mm steps.

The bandwidth of the spectrum is said to be limited by the COD because the gain spectrum of the SOA is narrower at a lower current. If the current is increased, the ASE widens, especially in the shorter wavelength, thanks to one sub-band starting to emit at around 130 mA. However, the current cannot be turned up due to the dual amplification, which brings the internal power close to the COD. The issue might be solved by modulating the current of the SOA. A higher current would be set when the shorter wavelength of the sweep comes to the SOA and would later be decreased for the 860 nm range, where the gain is higher and does not require a higher current.

Owing to a higher gain-loss ratio in this dual amplification FDML laser, a low noise regime, sweet spot [113] seems to appear, which will enable a more accurate dispersion compensation than in the 3 cFBGs configuration. Adjusting the length of the fiber in the laser will imply a higher SNR and longer roll-off. However, due to a lack of balanced photodiode around 850 nm with bandwidth above 1 GHz, a group delay compensation achieving less than 200 fs like in 1300 nm FDML laser [46] will not be achievable.

3.2.5. Balanced photodiodes for 850 nm

Since the 850 nm wavelength is at the edge of usability for InGaAs photodiodes intended for 1550 nm, 1300 nm, and 1060 nm, it is essential to explore different photodiode options. The responsivity of four photodiodes from different manufacturers is evaluated and detailed in Table 5 below.

Silicon, highlighted in green in the table, is particularly sensitive around 850 nm, with a peak responsivity of about 0.4 A/W. A custom-made photodiode from Wieserlabs GmbH is compared with one from Newport Co., both featuring a similar electrical bandwidth of around 600 MHz. Additionally, the responsivity of two InGaAs photodiodes is examined, one from Thorlabs and

one from Optilab. Although they offer faster RF bandwidths than silicon, their responsivity at 850 nm is expected to be around 0.2 A/W, which is lower than silicon.

To practice these experiments, the 850 nm FDML laser is modulated by 25%. A peak power around ~280 µW is applied to the photodiode and a voltage is measured on a 20 GHz oscilloscope at 40 GS/s (Lecroy Teledyne, Wavemaster 820Zi-b). From the voltage and the transimpedance gain of each photodiode, the responsivity is calculated back.

Table 5. Comparative table of the different balanced photodiodes tested with the 850 nm FDML laser

Photodiode	Type	Average input power (µW)	Voltage (mV_{pp})	Trans-im-pedance gain (V/A)	Calculated Responsivity (A/W)	RF bandi-wdth (GHz)
Thorlabs PDB480C-AC	InGaAs	70	300	30 000	0.052	1.6
Optilab BPR-23-M	InGaAs	70	200	4 000	0.18	20
Wieserlabs Custom-made	Silicon	70.8	200	3 500	0.19	0.600
Newport 1607-AC-FC	Silicon	51	50	700	0.41	0.650

Table 5 highlights the photodiode from Newport Co., which boasts high responsivity. However, its transimpedance gain of 700 V/A means the signal is not adequately amplified, so the option is not selected. As for the Thorlabs photodiode, although it offers high gain, its responsivity remains too low, potentially leading to increased electronic noise compared to the optical signal. Hence, this diode is also rejected. The Optilab and Wieserlabs photodiodes show comparable responsivity and gain but differ significantly in frequency. The manufacturer suggests higher responsivity for both photodiodes used in the Wieserlabs balanced photodiode (0.3 A/W). Additionally, an RF bandwidth of 20 GHz in unnecessary and can even be problematic, as it may introduce unwanted high-frequency noise. The 600 MHz RF bandwidth of the Wieserlabs detector is more than sufficient for retinal imaging, as the sample is relatively thin, making it the preferred choice for OCT applications. However, if roll-off or phase stability need to be measured, the Optilab balanced photodiode would be preferable due to its higher RF bandwidth, providing more insight into the light source. Figure 48 offer an overview of all acquired signals. All signals have been low pass filtered at 2 GHz in post processing to offer a more uncluttered view of all signals together. The Wieserlabs and Newport diodes exhibit reduced noise thanks to their narrower electricals bandwidth. The Wieserlabs' photodiode stands out with a distinctive electrical signal compared to the other four. This divergence stems from its unique electronic architecture. While all four diodes

are AC coupled, in the case of Wieserlabs, the capacitor employed to block DC components charges and discharges in response to detected light, resulting in potential variations that shape the signal. This difference will not be seen when used in the balanced way.

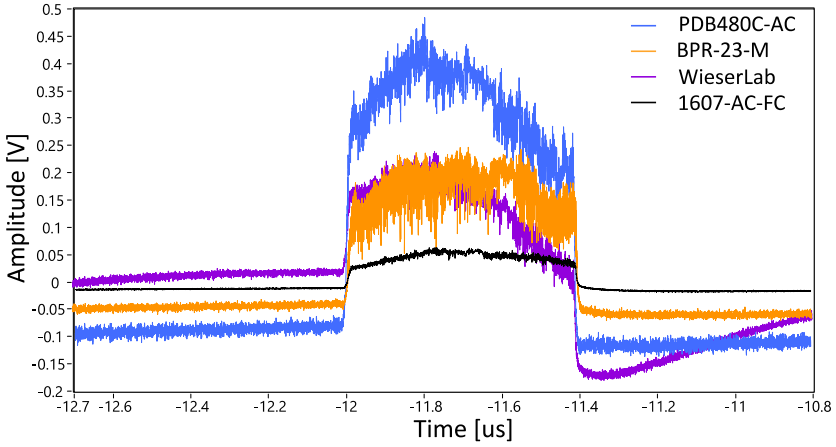

Figure 48. Amplitude of the output of the laser measured with 4 different photodiodes over time. All signals are post-processed with a low pass filter of 2 GHz.

As shown from the five preceding subsections, a multitude of challenges were encountered in achieving a high-performance light source. These ranged from combating high chromatic dispersion and PMD to addressing issues like low gain. Various experiments were devised to mitigate and gradually ameliorate each drawback associated with lower wavelengths. The subsequent chapter will delve into the performance analysis of the finalized 850 nm FDML laser.

3.3. Performances and characterization of the 850 nm FDML laser

This subsection provides a comprehensive characterization of the laser across various stages of its development. Certain characterizations were conducted during periods when the laser lacked adequate dispersion compensation and temperature control. Both pre- and post-improvement experiments were carried out to facilitate comparison.

The draft of the 850 nm FDML presented earlier in Figure 29 is updated to the one shown below in Figure 49. The initial cFBG is strategically placed immediately following the SOA to optimize the extraction of maximum output power. Additionally, an isolator has been incorporated before the SOA input. Experimental observations have revealed that the circulator's isolation performance was inadequate, allowing laser emissions from the SOA (presented in 3.1.2) to propagate towards the cFBG, resulting in unintended back-reflection and consequential anomalous behavior. The cFBGs used here have a bandwidth of 72 nm and a reflectivity of ~80% (Teraxion, PSR-840-72(+D16.77-0.035)-0S1-0R). The output spectrum is depicted alongside the achieved output

power in the following subsection. An in-depth examination is also given to the laser's noise characteristics, with particular emphasis on phase stability and identification of its sweet spot.

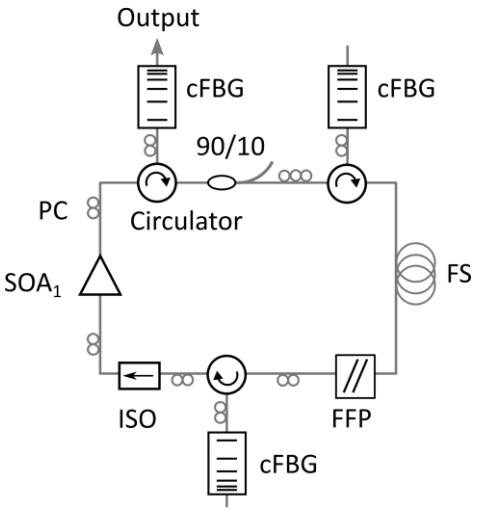

Figure 49. Final 850 nm FDML laser design. SOA: semiconductor optical amplifier, PC: polarization controller, cFBG: chirped fiber Bragg grating, FS: Fiber spool, FFP: fiber Fabry-Pérot, ISO: isolator.

3.3.1. Optical bandwidth

The output of the laser is acquired with an OSA (Yokogawa, AQ6370) set on 0.02 nm resolution and on "HIGH 1" sensitivity setting. In Figure 50, the left panel illustrates the laser output without modulation, while the right panel depicts the output with a 25 % duty cycle modulation. These spectra showcase the best performance achievable from the laser. Through careful optimization of the polarization controllers during experimental procedures for characterization or imaging, it is consistently tried to achieve this level of performance. The non-modulated laser shows a top-hat bandwidth of 40 nm centered around 845 nm yielding to an axial resolution in air of 10.7 µm. In this scenario, prioritizing a high-quality spectrum over a wide one is preferable. While it is feasible to sweep wider than 50 nm, it would result in increased ripples at the spectrum's edges. Moreover, amplification would decrease in some parts of the spectrum, leading to a less uniform spectrum that could potentially compromise resolution. The narrower bandwidth observed in the modulation mode is attributed to careful use of the FFP-TF. Since 75% of the spectrum is cut by modulation, the amplitude of the filter must be increased to reach a similar bandwidth when no modulation is applied. A 30 nm bandwidth has been achieved yielding to an axial resolution of 14.4 µm.

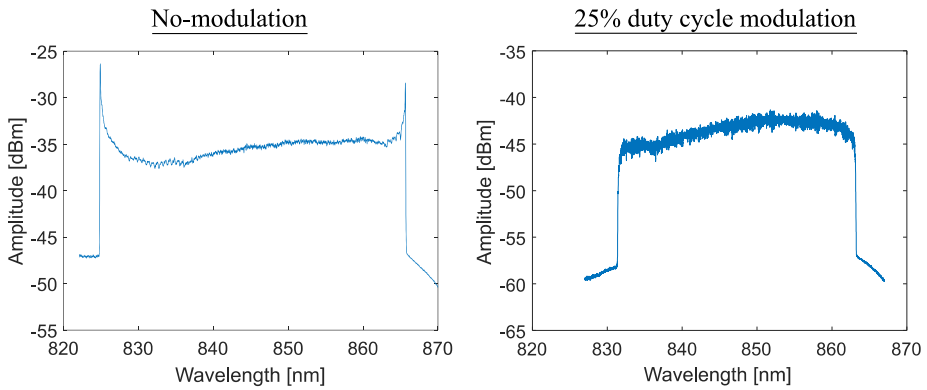

Figure 50. Output spectrum of the 850 nm FDML laser, non-modulated and modulated with a duty cycle of 25%.

Higher noise levels are evident in the modulated laser spectrum compared to the non-modulated one. This occurs when the laser operates at its optimal "sweet spot". Both spectra were obtained following meticulous chromatic dispersion compensation and laser temperature control. However, as discussed later in section 3.3.2, some dispersion remains uncompensated. When modulated, the laser tends to operate closer to its optimal sweet spot due to utilizing a more linear segment of its tuning curve. This closer proximity to the sweet spot facilitates better mode locking and higher amplification. The observed noise may be attributed to lower-frequency fluctuations in the laser light, discernible on the OSA. Similar behavior is illustrated in the left graph, where the laser exhibits a slight increased noise levels between 840 nm and 860 nm, indicating closer alignment with the sweet spot.

3.3.2. Chromatic dispersion compensation

All measurements presented in this section were conducted with the laser under temperature-controlled conditions. The fiber spool temperature was regulated at 30°C using four Peltier elements positioned beneath it. This temperature was selected to match the conditions under which the previous dispersion measurements were performed to define the cFBG. The FFP-TF was similarly temperature-controlled and maintained at 20°C to remain close to ambient conditions. All components were housed inside an aluminum enclosure, insulated on the sides with polystyrene. To facilitate manual adjustment of the polarization controllers, they were mounted externally on the case. While this arrangement resulted in less-than-ideal temperature stabilization, it minimally impacted dispersion, as only about 1.6 meters of fiber were exposed. Although the laser exhibited minor drift over time, the effect was negligible. The most noticeable consequence of imperfect temperature insulation was observed in the laser's PMD. When restarting the laser after several hours of inactivity, a slight reset of the polarization controllers is required. However, it remained stable throughout the day, provided there were no significant temperature fluctuations in the room. With the laser temperature stabilized, chromatic dispersion measurements could commence, facilitating the subsequent compensation process.

To ensure precise chromatic dispersion compensation in FDML lasers, our research group utilizes a specialized LabVIEW based software that has been developed in the past. To use this software,

high frequency fringes are generated utilizing a MZI. These fringes must have a high enough frequency so that the photodiode used to acquire them cannot detect them, i.e. the RF bandwidth of the photodiode is lower than the frequency of the fringe. Thanks to this, the sweet spot of the laser can be observed and detected with low-cost (i.e. low analog detection bandwidth) devices, as detailed in [160]. In fact, intensity dips, which cannot directly be detected with these devices due to their too high frequency, generate lower frequency disturbances in the interference signal visible on a slow oscilloscope. As the laser approaches a sweet spot behavior, these disturbances reduce, and the signal drops to 0 V as the fringe frequency exceeds the analog detection bandwidth of the detector. Figure 51 shows this phenomenon, high frequency fringes are generated and acquired with a 600 MHz Wieserlabs photodiode on a 1 GHz oscilloscope (Tektronix, DPO5104). The oscilloscope is set to Digital Phosphor Technology (X) (DPX) mode. This mode captures and processes multiple waveforms over time and generates a composite display that facilitates the observation of the sweet spot. Events that occur frequently are displayed in red, gradually transitioning to purple for less frequent occurrences. This color map effectively visualizes the frequency of events over time. On the left part, the laser is sweeping at a frequency of about 414 kHz (backward sweep) and shows a narrow sweet spot which moves right or left depending on the frequency. There is a difference of 0.392 Hz between each dataset. The sweet spot moves with frequency because chromatic dispersion is still present. If no chromatic dispersion were observed, the sweet spot would be present over the entire spectrum for one frequency. Here it moves through the wavelengths because all of them are not travelling at the same speed.

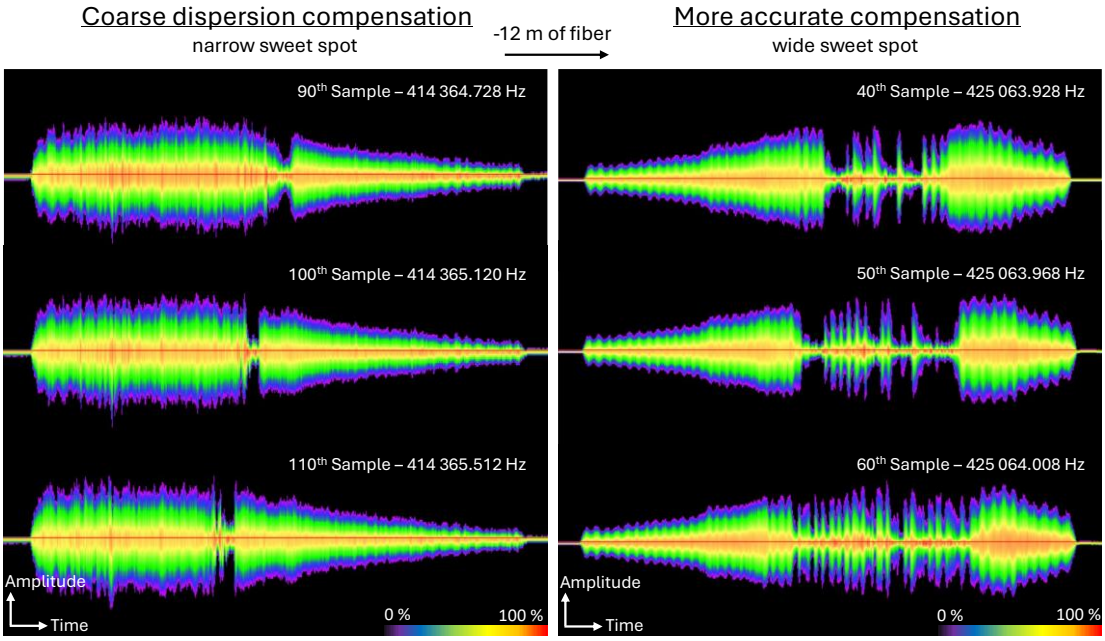

Figure 51. Observation of the laser's sweet spot at different frequencies with a first coarse dispersion compensation on the left and a more accurate one on the right. High frequency fringes are generated using on the left a backward sweep and on the right a forward sweep after a removal of 12 meters of fiber. Data are visualized with the DPX mode of a 1 GHz oscilloscope.

Once a sweet spot is observed in the DPX mode, the filter is driven through a range of frequencies and DPX datasets are acquired at these different frequencies. 200 samples are acquired at 200 different frequencies. This method enables to retrieve the amount of dispersion remaining in the laser by first summing, for each 200 datasets, all rows in each column to generate 200 individual 1D vectors. These vectors are then transposed to form a new 2D matrix, where each column corresponds to one sample (i.e. frequency). Finally, the center of gravity is calculated for each row (i.e. wavelength) in this matrix, yielding detailed information about the dispersion. In Figure 52, a first evaluation of the remaining chromatic dispersion present in the laser is measured. The laser is set so that the output spectrum is ~27 nm, with a 25 % duty cycle. (A) shows that the software is only able to work in the middle wavelength, where the sweet spot is better defined. This can also be seen in (B) where the center of the output spectrum of the laser is indented, highlighted by two black markers. The small set of data that can be worked with is fitted with a 1st order polynomial as shown in the inset of (A). The linear coefficient gives information on how much optical fiber must be added or removed to the laser. Here, since Hi780 fiber with a dispersion of -100 ps/nm/km is used, and the coefficient being -1.35 ps/nm, 13.5 meters of Hi780 fiber must be removed. Figure 51 right shows the new laser performances after removing ~12 meters of Hi780 fiber. A wider sweet spot is achieved which proves a reduced chromatic dispersion. A difference of 40 mHz separates each DPX trace.

When the laser was operated in a non-modulated state, the forward sweep exhibited a slightly better performance. As a result, all images acquired during this phase, at the university of Kent were captured using the forward sweep. For consistency, the forward sweep is selected again for precise dispersion compensation. It is important to choose one sweep direction before optimization, as slight variations can occur between forward and backward sweeps.

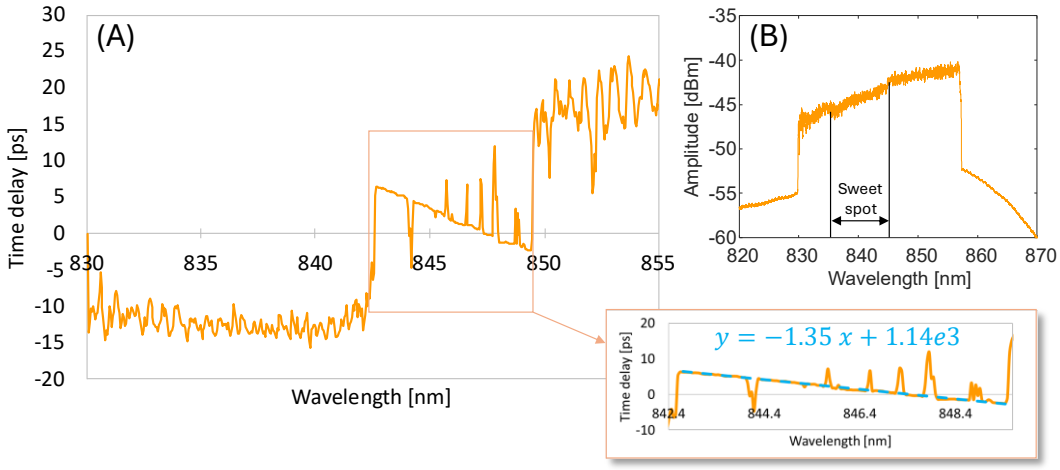

Figure 52. First evaluation of the remaining chromatic dispersion in the laser. (A) represents the time delay remaining between wavelengths in the laser. The inset shows a slope of -1.35 ps/nm. Data outside the inset are unusable. (B) Output spectrum of the laser when measuring the remaining dispersion in (A). It shows a sweet spot behavior around 840 nm.

After removing these 12 meters of fiber, the laser exhibited a time delay that varied with wavelength, fitting a second-order polynomial curve. This pattern indicates that significant second-order chromatic dispersion persists in the laser. Compensating for this type of dispersion typically involves using a combination of fibers, such as Hi1060 and SMF28, particularly for lasers operating at longer wavelengths. However, at around 850 nm, options are limited primarily to Hi780 fiber or similar alternatives. To address the dispersion, we attempted to compensate by applying a uniform temperature gradient across each of the three cFBGs (the gradient is the same for the three cFBG). This method aims to manipulate the refractive index gradients and thus mitigate the dispersion effects. Results are shown in Figure 53. Each end of the cFBG is subjected to a specific temperature, designated as cFBG+ and cFBG-, respectively. The temperatures are precisely controlled using thermoelectric controller (TEC) controllers (TEC1020T, Thorlabs) connected to Peltier elements. After setting the temperatures, a stabilization period of 15 minutes is observed before initiating the dispersion measurements. The experimental results are presented in Figure 53, where each curve within the region of interest, marked by a black arrow, is fitted with a 2nd order polynomial. Above 20 different temperature settings were tested and analyzed. The analysis reveals that a too high gradient between both ends of cFBG increases chromatic dispersion. Another analysis showed that the warmer the cFBG+ side of the cFBG is the more 2nd order chromatic dispersion. Optimal temperatures of 25°C for cFBG+ and 20°C for cFBG- have been identified for future use in the laser system, as they demonstrate the best performance characteristics. Indeed, the 2nd order coefficient is the lowest in the case of the pink curve, $-0.0140\ ps/nm^2$. Since the 2nd order chromatic dispersion of Hi780 fiber has been previously measured to be $0.209\ ps/nm^2/km$, it would mean that 67 meters of fiber must be removed to achieve a null second order. However, this is not desirable since it would worsen the 1st order dispersion remaining in the laser. This second-order dispersion error may originate from the cFBG manufacturer. According to their datasheet, this parameter is listed as 'not measurable.' While they produce cFBG to the best of their ability based on the specifications given to them, they are unable to verify post-manufacturing whether the final products meet exact requirements. It might also originate from the measurement setup developed here and detailed earlier in the thesis, see 3.2.1. Temperature shift during the measurement or currently in the actual laser might influence this result.

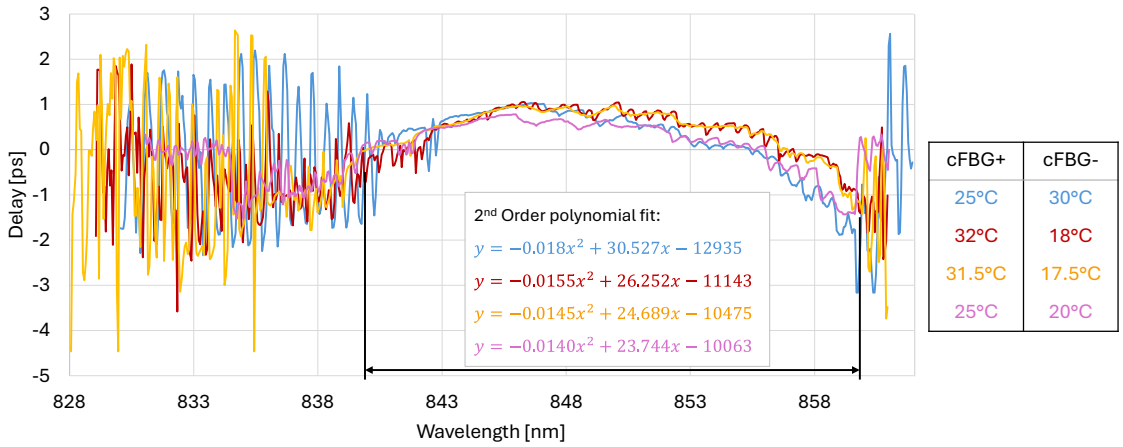

Figure 53. Second evaluation of the remaining delay between each wavelength in the laser. Each plot gives the remaining chromatic dispersion for four different temperatures applied to the cFBG.

It should also be noted that the usable data region for chromatic dispersion calculation is broader than in previous measurements as shown in Figure 53 and Figure 52, which had > 20 nm and < 10 nm respectively.

The limited laser power and increased noise at the edges of the laser spectrum prevent the software from accurately calculating dispersion outside the optimal range, as illustrated at the edges of Figure 53. While the first-order dispersion is successfully reduced, compensating for second-order dispersion at wavelengths around 850 nm proves to be considerably more complex. The limited availability of optical fibers designed for operation near 850 nm leaves the formation of a gradient in the cFBG as the only viable solution for addressing the residual second-order dispersion. This approach may be suitable for certain applications, but in cases where second-order dispersion is excessively prominent, it becomes impractical.

3.3.3. Phase stability

[The work presented in this section has already been presented and published in a peer-reviewed journal [31]. Most of the sentences, paragraphs and figures are taken from it.]

As mentioned in section 2.2.2, swept sources must present low phase noise. The phase from one sweep to another must be as similar as possible. If a laser presents high phase stability, it can be used in different fields of OCT, like phase sensitive OCT, or dynamic OCT.

Here, the phase stability is measured at the direct output of the laser over 1,000 consecutive forward sweeps. It is important to note that at the stage of this measurement, the laser was not presenting any temperature control and was having a narrow sweet spot at a sweeping frequency of ~ 2 x 414 kHz. Also, all sweep calibrations were done following the CMS methods since these measurements were performed at the university of Kent where the CMS is mostly used for OCT.

Interferences are generated in a common path configuration using a glass plate thickness of 235 µm introduced halfway through in the reference path, as presented in Ref. [161]. Two

different glass thicknesses are used before the measurement to create the masks used for signal processing [38, 39]. A 20 GHz oscilloscope (Lecroy Teledyne, Wavemaster 820Zi-b) was used to acquire 1,000 sweeps with 80 GS/s in a single acquisition. A trigger phase-locked with the filter frequency/waveform of the FDML is saved in the meantime and used in post-processing to separate each sweep. Such a strategy is employed here to avoid a jitter noise that the trigger from the acquisition card could generate. Once all forward sweeps are cropped, the CMS protocol is performed, the interference noise is removed, and an iFFT (inverse Fast Fourier transform) is used to obtain the linearized signal. The phase is then computed using a Hilbert transform (Figure 54 (A)). The standard deviation of each point over the sweep is calculated following the method in [161]. As shown in Figure 54 (B), the laser has an average standard deviation of 14 mrad over 1,000 sweeps. Due to an optimization of the filter frequency to approach sweet spot operation in the middle of the sweep, the phase instability is lower in this region.

The phase stability of the laser having a standard deviation of time jitter of 25 ps over 1,000 sweeps makes it usable for phase-resolved techniques, such as OCT angiography [162], which has already been shown with a 1060 nm FDML laser in [163]. Also, as demonstrated in the preceding section, enhancing the dispersion compensation broadens the laser's sweet spot, which suggests improved phase stability because of better mode locking.

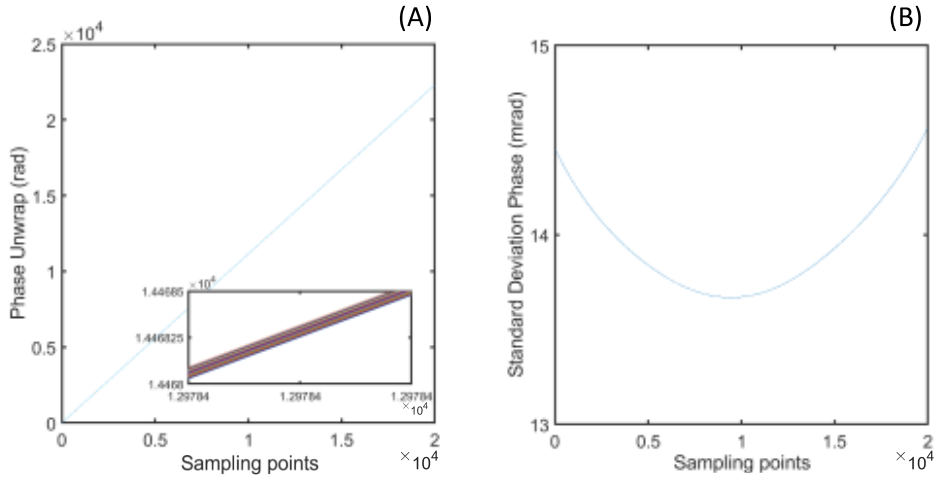

Figure 54. Phase stability of the 850 nm FDML laser. (A) Spectral phase for 1,000 forward sweeps, inset: zoom into its fluctuation. (B) Standard deviation for variation of phase among all 1,000 sweeps.

3.3.4. Noise characterization

Another interesting objective when doing ophthalmic imaging, apart from imaging the retina and the choroid, is to image both, the front of the eye (the lens) and the back (the retina) at the same time. Although the retinal area that can be imaged is limited, as the scanners' pivot point must be placed outside the eye, in front of the lens, it can bring more information to physicians. Achieving this “double” imaging requires a laser with a long coherence length, above 2 cm. In this section, the laser noise is characterized by studying the direct output of the laser. The sensitivity roll-off

is measured using a MZI and the stability of the laser over a period of 30 min is investigated. All data acquired in this section are using forwards' sweep.

Firstly, the roll-off and the power spectrum of the laser are studied. The power spectrums represent the direct output of the laser detected by a photodiode on an oscilloscope. The first dataset in Figure 55 was acquired using a 23 GHz balanced photodetector (Optilab, BPR-23-M) and a 40 GS/s, 20 GHz oscilloscope (Lecroy Teledyne, Wavemaster 820Zi-b). The fringes for roll-off measurements were acquired using both inputs of the photodiode, most of the common-noise of the laser is canceled out by the balancing. The second and third sets were acquired using a 30 GHz photodetector (Thorlabs, DMX30AF), non-balanced, and an 80 GS/s, 63 GHz real time DSO (Keysight, DSOZ634A).

Figure 55 summarizes the experimental results, comprising three sets of data. The top set was acquired before accurate dispersion compensation was performed. Initially, precise chromatic dispersion measurements were not conducted during the first phase of laser development, as the SOA used had lower gain, preventing the measurement described in section 3.3.2. Once a new, higher-gain SOA became available, the measurements were completed, allowing for improved chromatic dispersion compensation. The first top roll-off (left) and power spectrum (right) correspond to the narrow sweet spot shown in Figure 51 (left), though without modulation here. This state was consistently maintained at the University of Kent. All results, images and data in the following sections obtained at this university, reflect this roll-off result. The frequency of the first dataset do not exactly match the one in Figure 51 (left) because the laser is not modulated here so the frequency might have been set to another point in the sweep. Also, it is not temperature stabilized, causing significant drift in the optimal operating frequency from day to day. Additionally, the polarization required at least an hour of adjustment after several hours of inactivity. Nevertheless, despite the noisy laser output visible in the power spectrum, the laser shows a sensitivity roll-off of 6 dB at more than 1.2 cm delay, corresponding to > 6 mm OCT imaging depth (return path).

Both other sets of measurements were realized with the same laser configuration, same dispersion compensation (length of fiber), duty cycle of 25 % and a bandwidth of ~30 nm. Only the driving frequency of the filter is different, apart from 190 mHz. The data acquired at 425 061.801 Hz was chosen for its wide sweet spot, from 230 ns to ~520 ns. The noise is highly reduced in this area compared to the side of the spectrum. FDML holes, also called 'intensity dips', as detailed in section 2.3.1 can also be observed in this low noise region, as shown with both insets. Each hole is about 120 ps long. They are due to, as mentioned in 2.3.1, imperfect dispersion compensation. Certain wavelengths in the spectrum are not subject to direct amplification like others. For example, a particular wavelength may arrive at the filter with a delay caused by dispersion, preventing it from passing through. Instead, it is reconstructed from spontaneous emission, which explains the resulting drop in intensity followed by an overshoot. Outside this low noise region, the noise on the edges is due to GHz oscillations, as explained in 2.3.1. In the second and third data sets,

the oscillations show a frequency around 1-1.5 GHz. When working with a forward sweep, for the same deviation from the sweet spot frequency, the laser exhibits lower noise levels when operating at a positive deviation compared to a negative one. Both, GHz oscillations and holes can be observed in the same graph due to the remaining quadratic dispersion, as shown in 3.3.2. Here as the frequency increases – from the bottom dataset to the middle dataset – the low noise region widens, leading to an increase in the number of holes. In the meantime, the GHz oscillations at the edges decrease, which is in theory beneficial for FDML lasers. However, here, the longer sensitivity roll-off is achieved with a narrower sweet spot, bottom graph.

The last set of measurements was acquired at 425 061.611 Hz. In this case, a fast Fourier transform (FFT) was generated live on the oscilloscope. The frequency was optimized to obtain the most discernible point spread function at about 1.5 GHz frequency. By adjusting the frequency of the FFP, the noise floor fluctuates, raising or lowering. The same impact is observed regarding the peak amplitude. Once set, the roll-off measurements were realized. As it can be seen in the bottom right graph of Figure 55, even though the OCT imaging depth is reduced by 6 dB at about ~15 mm, which is the longer measured with this laser, the power spectrum shows a narrower sweet spot compared to the middle measurement. These measurements underscore the importance of setting the filter frequency based not on power spectrum analysis or the OSA but rather on the point spread function on an oscilloscope. The most effective approach to adjust the laser frequency is by directly observing noise in the OCT live image. By fine-tuning the settings to minimize noise within the live image, the optimal frequency for high-quality imaging can be achieved.

Figure 55 shows the laser's dynamic range at different depths. At frequencies below 1 GHz, the last two datasets demonstrate a dynamic range of 35 dB. For biological tissue imaging – the primary goal here – a peak signal around 55 dB is expected, resulting in a sensitivity of 90 dB. This sensitivity is higher than the anticipated value calculated in the next chapter. The first dataset shows a higher dynamic range, 40 dB but only up to 500 MHz. Notably, the dynamic range decreases significantly beyond these limits, dropping to as low as 15 dB, which could reduce image quality.

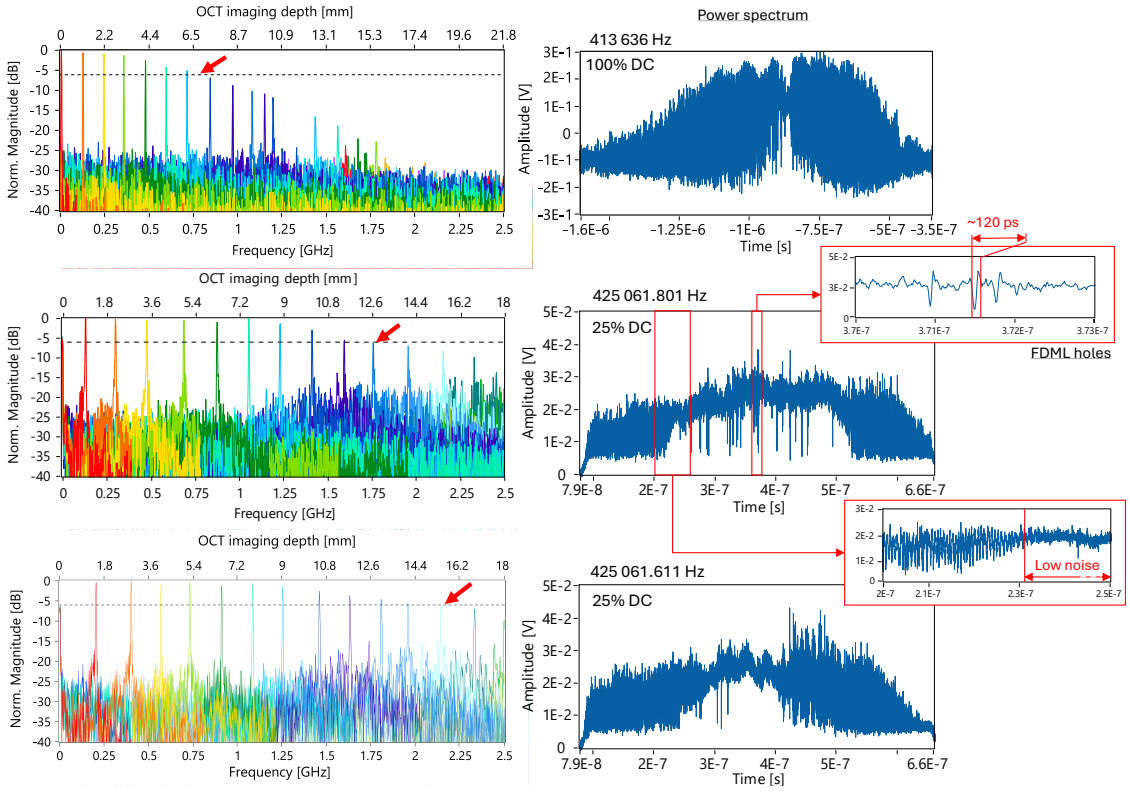

Figure 55. Sensitivity roll-off and power spectrum of three datasets at three different frequencies using forward sweeps. The first dataset, acquired at 413,636 Hz with 100% duty cycle (DC), exhibits a noisy laser output and rolls off by 6 dB at approximately 0.8 GHz. The other two datasets, obtained after precise chromatic dispersion compensation, demonstrate extended roll-offs, reaching 12.6 mm and ~15 mm at 425,061.801 Hz and 425,061.611 Hz respectively, as indicated by the red arrows. The power spectra for both frequencies show regions of low noise as highlighted in the insets.

Previous studies suggest that backward sweeps offer better dynamic range in FDML lasers at high speeds [164]. However, initial tests conducted at the University of Kent showed better performance with the forward sweep as mentioned previously, so this sweep direction was chosen for imaging. As new dispersion compensation measurements began, the forward sweep was retained to maintain consistency and allow for comparative analysis. Thus, dispersion compensation was optimized for forward sweeps, which were subsequently used in all following experiments.

Overall, these measurements highlight the critical importance of dispersion compensation in the laser system. Dispersion compensation improved the laser's roll-off performance by more than twofold. Additionally, this emphasizes the need for precise frequency control – down to a few tens of millihertz – even though the laser's dispersion is compensated only to within a few picoseconds rather than to the ideal <200 femtoseconds. Temperature control is equally essential; a frequency shift of 190 mHz corresponds to a temperature change of just 5.5×10^{-2} °C across 500 meters of fiber which would reduce the roll-off by 6 mm.

Achieving this level of precise control is, however, challenging, since portions of the fiber extend outside the laser system. Consequently, while the laser may experience minor frequency drift and might not always operate at peak performance as studied in the following, this is sufficient for

retinal imaging, where extreme roll-off is not critical. Nonetheless, maximum stability across all components to ensure optimal performance along one imaging session is tried to be maintained.

To assess the stability of the laser during a typical 30-minute OCT imaging session following calibration, the laser's spectrum and a representation of the "sweet spot" are recorded at t = 0 min and at t = 30 min, as shown in Figure 56. The sweet spot is observed by generating an interference signal with a MZI having a higher frequency than the electrical bandwidth of the photodiode used (Wieserlabs, custom-made 600 MHz Si), as explained in 3.3.2. The resulting signal is acquired with the DPX mode of a 1 GHz oscilloscope (Tektronix, DPO5104). The laser optical bandwidth is observed using an OSA (Yokogawa, AQ6370). Settings and characterization of the laser are given on the right in the corresponding figure. The optical bandwidth and the driving current of the SOA are the same in both cases, ~31.7 nm and 152 mA respectively. In case of A), the frequency of the laser is optimized to obtain a wide sweet spot. It can be observed on the left by sudden drops in amplitude in the center part of the signal. An average output power of $0.420\ \mathrm{mW} \cdot 4 = 1.68\ mW$ is achieved. The measured output power shows 0.420 mW because the laser is modulated by 25 %. The power meter shows an average output power, to obtain the peak power (power of the sweep), it must be multiplied by 4. In B), the frequency is optimized to reach the highest output power, in this case $0.460 \cdot 4 = 1.84\ mW$. The frequencies A) 425,124.121 Hz and B) 425,124.483 Hz differ by only 362 mHz – a small variation that nonetheless results in a significant power change of 0.16 mW, approximately 10% of the total output power. However, by tuning the frequency to the sweet spot, version A), the SOA current can be increased to achieve the same output power as B), as the output power is ultimately limited by the SOA's COD threshold rather than its gain.

In Figure 56, panel A) left shows that over 30 minutes, the laser temperature has drifted, shifting the sweet spot shape and nearly moving it out of the optimal range. However, the optical bandwidth of the laser, presented on the right, remains stable in wavelength, with only amplitude differences observed. At t = 0 min, the ASE is slightly lower than at t = 30 min, which correlates with the amplified spectrum being more intense around 850 nm at t = 0 min. In panel B), a minor wavelength shift of approximately 1 nm is evident. Assessing the temperature's impact on the left is challenging since the system is no longer at the sweet spot, making differences in the spectra less straightforward to interpret. However, on the left side, a noticeable edge drift to the left, marked by two white arrows, provides a clear indication of this shift.

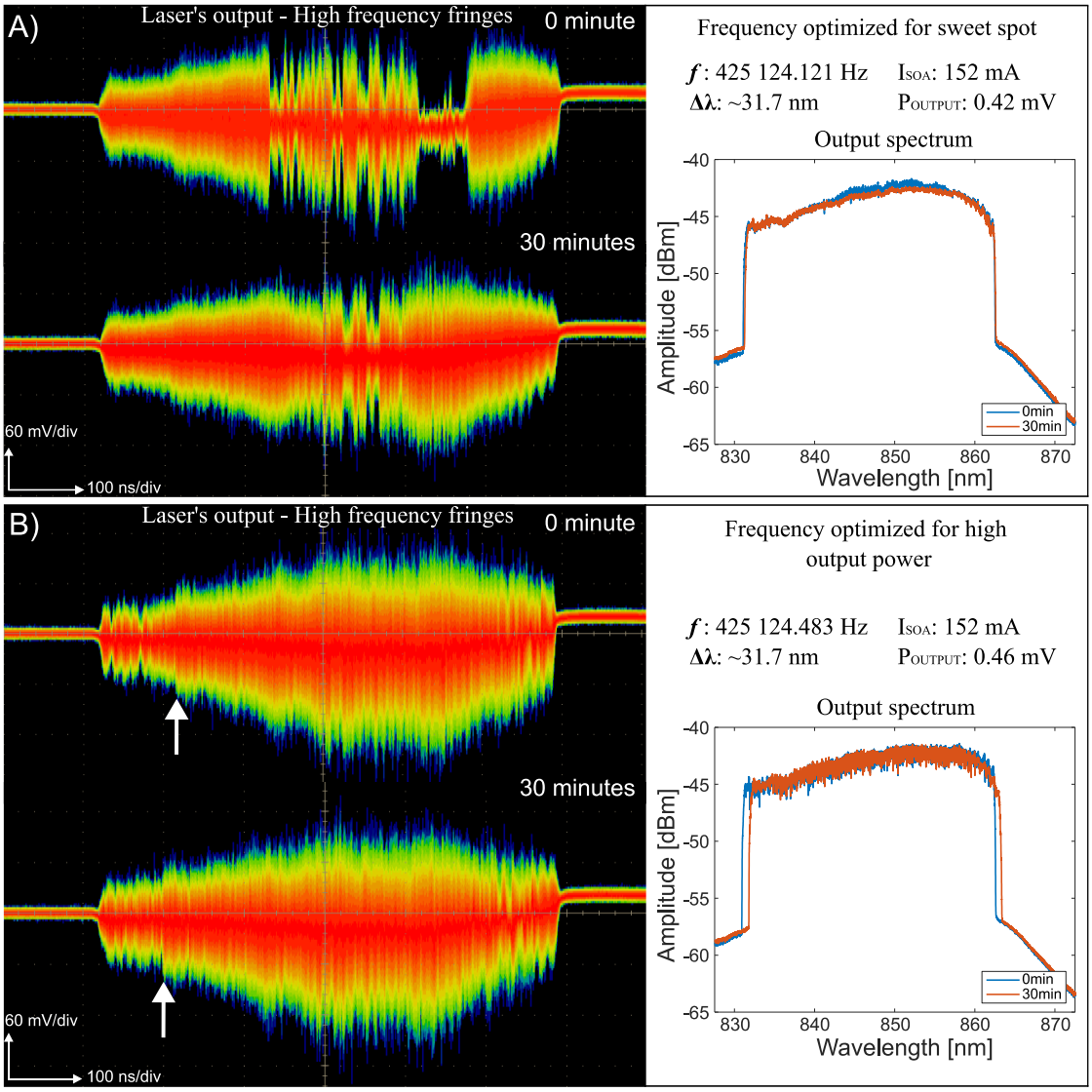

Figure 56. Investigation of the stability of the laser's spectrum and output power over time at two different frequencies, A) at 425 124.121 Hz and B) at 425 124.483 Hz. On the left side, fringes with frequency higher than the photodiode's electrical bandwidth are generated using a MZI and are observed with the DPX mode of an oscilloscope. On the right, the optical bandwidth of the laser is shown. All data are taken at t = 0 min and t = 30 min. Two arrows in B) shows a drift in laser temperature. f: frequency, Δλ: optical bandwidth, ISOA: current of the SOA, POUTPUT. Output power.

Comparing the optical spectra of Figure 56 A) and B), the top of the spectrum in configuration B) appears noisier than in A). As previously mentioned, this noise occurs near the sweet spot. In both configurations – A), centered on the sweet spot, and B), offset by only a few hundred millihertz – noise is present, though more pronounced in B). This heightened noise in B) may stem from the slight offset from the sweet spot and the higher output power.

Additionally, it was observed that when the laser is set to the sweet spot in configuration A), the output power fluctuates by approximately 12 µW. In contrast, configuration B) demonstrates highly stable output power with virtually no variation. This intensity instability arises from the presence of transient intensity dips (holes) in the laser output. Near the sweet spot, these holes appear and disappear, leading to fluctuations in output power. Outside the sweet spot, this effect

is still present but the overall noise contribution to the power is more significant resulting in a more stable output power.

In conclusion, the laser continues to show some instabilities in temperature control, gradually impacting its performance. Nonetheless, it remains sufficiently reliable for retinal imaging. To optimize performance, the laser frequency should be carefully set before system calibration. A frequency closed-loop feedback control could also be implemented to maintain the laser at sweet spot. Initially, the frequency is adjusted close to the sweet spot by observing the output spectrum on an OSA and power on a power meter. Once the laser is prepared for imaging, ~30 nm bandwidth reach, close to COD operation and minimized ripples, the frequency is fine-tuned based on noise levels in the OCT image. After identifying the optimal frequency, the SOA current is adjusted – either increased or decreased – to achieve an output power just below the COD threshold. If frequency drift occurs, it can be reset via software – a straightforward adjustment, though it may require a new background acquisition during imaging due to potential power fluctuations. Besides moving out of the sweet spot, another concern is wavelength drift, which can affect calibration accuracy and degrade image quality. If the wavelength drift exceeds 5 nm, lasing may cease in certain areas, though a simple adjustment to the filter offset will typically recenter it. A more complex challenge with temperature drift is the potential appearance of ripples or PMD. When PMD reappears, it disrupts imaging sessions since polarization controllers of the laser need to be reset which might require time and will necessitate recalibration. Overall, despite the challenges with temperature control, the laser delivers impressive performance, allowing for retinal imaging for at least 30 minutes without any issues. If the room temperature is maintained relatively constant, imaging sessions can be extended even further, ensuring excellent results and reliability throughout the process.

3.4. Conclusion and outlook

Section 3 shows that **chromatic dispersion** significantly impacts the performance of FDML lasers, influencing factors such as achievable optical bandwidth, as well as phase and intensity noise impacting its coherence length and mode-locking. For lower-wavelength lasers, such as the 850 nm-centered laser developed here, chromatic dispersion increases, introducing additional challenges that make it more difficult to achieve performance levels comparable to a 1300 nm laser.

Due to the high chromatic dispersion at 850 nm, the FDML laser design has been modified to include three cFBGs, unlike standard setups that use only one. This new configuration allows bandwidths exceeding the 24 nm limit, due to the mask size to manufacture cFBGs. With this setup, a **40 nm bandwidth** has been achieved at a repetition rate of **~414 kHz**. When using a 25% duty cycle, the repetition rate reaches **1.7 MHz** through optical buffering (detailed in the next chapter). Previous swept sources developed around 850 nm have shown much slower repetition

rates, below 50 kHz, with bandwidths not exceeding 42 nm. These results represent a significant improvement over published swept sources used for flying spot retinal imaging.

The use of cFBGs requires optical circulators, which unfortunately can introduce PMD at shorter wavelengths. The combination of PMD and cFBG poses challenges due to the resulting **wavelength-dependent PMD**, which complicates system setting. To mitigate this, polarization controllers are placed before each circulator input. Additionally, SOAs at 850 nm provide **lower gain** than 1300 nm SOAs, which degrades FDML laser performance. A higher SOA gain would help counteract PMD since they are less sensitive to polarization. The three cFBGs design, however, does result in higher optical losses due to the added cFBGs and circulators, although the laser still achieves the desired wide spectral output. A **dual amplification** setup, where the sweep is amplified twice in one round trip, was tested to further boost gain, but the limited SOA **COD threshold** constrains the bandwidth. Modulating SOA current relative to wavelength could improve performance by maintaining levels below the COD threshold, but this technique has not yet been tested due to potential risks to the SOA.

Another key challenge at 850 nm is **photodiode responsivity**. Silicon photodiodes have a lower responsivity (0.5 A/W) compared to InGaAs at 1300 nm (0.9 A/W), which represents almost a 3 dB sensitivity reduction in OCT systems.

In terms of other performance characteristics, chromatic dispersion has been compensated for, leaving only a residual second-order dispersion of $-0.0140\ ps/nm^2$, though further improvement is limited by quadratic dispersion, which is difficult to offset without specialized fiber types around 850 nm. Phase stability is promising, with a time jitter standard deviation below 25 ps over 1,000 forward sweeps, though it could be further enhanced by improved chromatic dispersion management which would improve the laser's mode-locking. A more stable interferometer design with effective temperature control would further enhance our analysis of the laser's phase stability. Despite the current open configuration, which may allow some external influences to affect measurements, the laser still demonstrates impressive performance for **phase-resolved techniques**. Its noise characteristics are highly favorable for retinal imaging, achieving over **15 mm of OCT imaging depth** at sweet spot. However, this depth is still insufficient to simultaneously image both the front and back of the eye, as a depth of approximately 2 cm is required.

While minor temperature fluctuations can cause some laser drift and introduce noise, FDML lasers generally deliver excellent stability and **ease of control**. Although PMD may occasionally require calibration, the system maintains consistent performance throughout a **30-minute imaging session** without the need for frequent adjustments. These results are very promising and underscore the potential for MHz retinal OCT imaging around 850 nm.

The frequency of the laser still requires daily adjustment, as small variations occur depending on the ambient temperature. This suggests that there is room for improvement in the laser's thermal

control; ideally, a perfectly temperature-controlled laser would maintain consistent frequency, stable to within millihertz precision, from day to day.

New components are planned for testing in the laser, with the aim of achieving even better results. First, all circulators could be replaced with **PM circulators**. These PM circulators, constructed with both PM780 and Hi780 fibers, are designed to block one axis of polarization, which would eliminate PMD—a significant improvement. However, blocking one polarization axis may introduce additional losses, so this approach will be tested soon to assess its impact on laser performance.

The second component under consideration is a **new FFP-TF**. Throughout this thesis, only one filter has been used, but higher-performance filters with greater amplitude and reduced loss are now available and will be evaluated. These filters could provide a laser with a wider bandwidth and an improved gain/loss ratio, potentially resulting in lower-noise output, as observed in 1300 nm lasers.

4. IMAGING

To evaluate the performance of the laser for potential future applications, OCT was conducted. Two image generation techniques were used during the PhD, allowing a comparison of their effectiveness with this specific laser. These techniques, complex master-slave interferometry and single-*k*-calibration were introduced earlier in section 2.1.2. For both methods, the OCT setups and performances, such as sensitivity and resolution, are discussed, along with corresponding OCT images. *In-vivo* retinal images demonstrate the laser's capabilities, and the two methods are compared. A final comparison will be made between retinal images taken with the 850 nm FDML laser and images obtained previously in our research group with a 1060 nm FDML laser. The chapter concludes with an evaluation of the laser's performance and outlook.

It is important to note here that the two imaging techniques were done at different stages of the laser's development. The complex master-slave technique was used when the laser did not have temperature control and was lacking some dispersion compensation of -1.35 ps/nm, its optimal performance was difficult to achieve. The single-*k*-calibration technique, on the other hand, was used when the laser was performing at its best. These differences likely affected the results of both techniques. Additionally, the optical bandwidth, the A-Scan rate and the power applied to the sample was not the same in both imaging sessions, which also influenced the laser's resolution and sensitivity. These differences will be discussed in detail in the following sections where both techniques will be compared.

4.1. Complex master-slave imaging technique

[The work presented in this section has already been published in 2023 in the journal Biomedical Optics Express [31]. Most of the sentences, paragraphs and figures are extracted from it.]

4.1.1. Setup

In Figure 57, a schematic diagram of the OCT instrument equipped with the FDML source is depicted. Light from the FDML laser is amplified by SOA_2 and isolated from the OCT setup by using an isolator. It is then directed towards an 80/20 fiber directional coupler, where 20% of the optical power is conveyed toward the sample arm. The light is then coupled to free space using a fiber collimator (F220APC-850, Thorlabs). It is deflected by two galvanometer scanner mirrors (Cambridge Technology, 6210H) and directed towards a telescope whose output is a 1.5 mm diameter collimated beam. The other 80% of the light is directed towards the reference arm of the interferometer. The splitting ratio of the coupler ensures a safe power level on the retina while more efficient collection of light from the sample, i.e. 80%. The backscattered light from the sample and reference arm interfering at the 50/50 coupler is detected by a custom-designed balanced silicon photodetector from Wieserlabs. Each photodiode has a responsivity estimated to be

~0.33 A/W at 850 nm. The balanced photodetector has an electrical bandwidth of 600 MHz. A 12-bit waveform digitizer board then acquires the signals at a rate of 4 GS/s (AlazarTech, ATS9373) before using the CMS procedure to generate images [38, 39]. For calibration purposes (computation of the functions describing the unbalanced dispersion in the interferometer as well as the sweeping non-linearity), a model eye including a 19 mm focal length lens (AC127-019-B-ML, Thorlabs) and a flat metallic mirror were employed. The optics of the sample arm are mounted on a motorized stage enabling pupil tracking using two cameras. The length of the sample arm can be adjusted via the computerized stage to change the focal point through the layers of the retina.

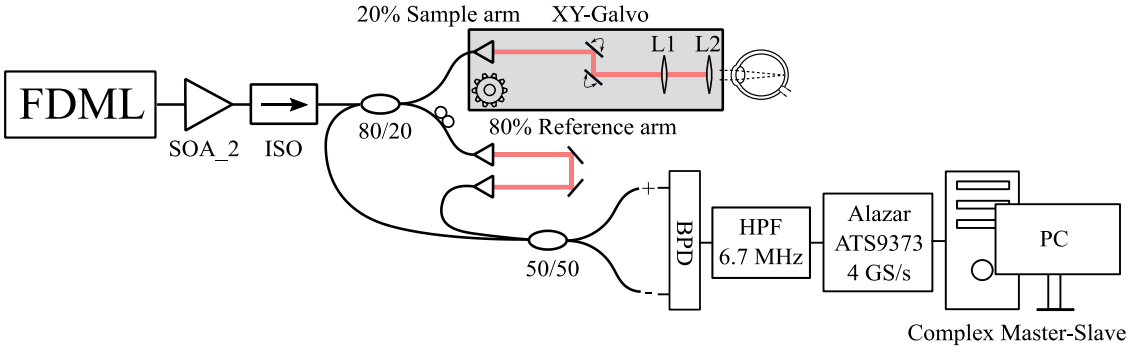

Figure 57. Schematic of the imaging set-up. The light at the output of the FDML is boosted by SOA_2. It then passes through an isolator that isolates the laser from the optical setup. The light enters finally the sample and reference arms which are split by an 80/20 coupler. They are then recombined by a 50/50 coupler and detected by a balanced photodetector (BPD). BPD: balanced photodiode, ISO: isolator, HPF: high pass filter, PC: personal computer.

During the initial imaging sessions in Kent, which marked the first tests of the laser, it was operated exclusively at a 100% duty cycle without any modulation. Subsequent sessions explored different duty cycles. However, to achieve a higher speed than the repetition rate of the laser, 414 kHz, both sweep directions of the laser can still be used. By doing this, the imaging speed can be doubled and reach 828 kHz. Before performing bidirectional imaging utilizing both sweep direction, forward and backward, it must be ensured that the calibration is adapted. For this, both sweeps' phases have been compared and a custom calibration has been developed.

Figure 58 (A) presents the superposition of both phase evolutions, expressed by g, along the forward and backward sweep. For both curves, coefficients of determination obtained by using linear fits are above 0.9983. These coefficients could increase towards 1.0 by modulating the laser and selecting a narrower, more linear part of the driving signal of the FFP-TF. The g functions are being compared, and the results are shown in Figure 58 (B). It is clear that both sweeps can be used for imaging due to their similar power level and phase behavior; however, for correct imaging in depth, separate masks need to be employed on each sweep. As a demonstration, Figure 58 (C) shows A-Scans in which correct masks are used for two forward sweeps, where good axial resolution is achieved, as well as forward masks employed for two backward sweeps, leading to a degradation in terms of axial resolution and height of the peaks.

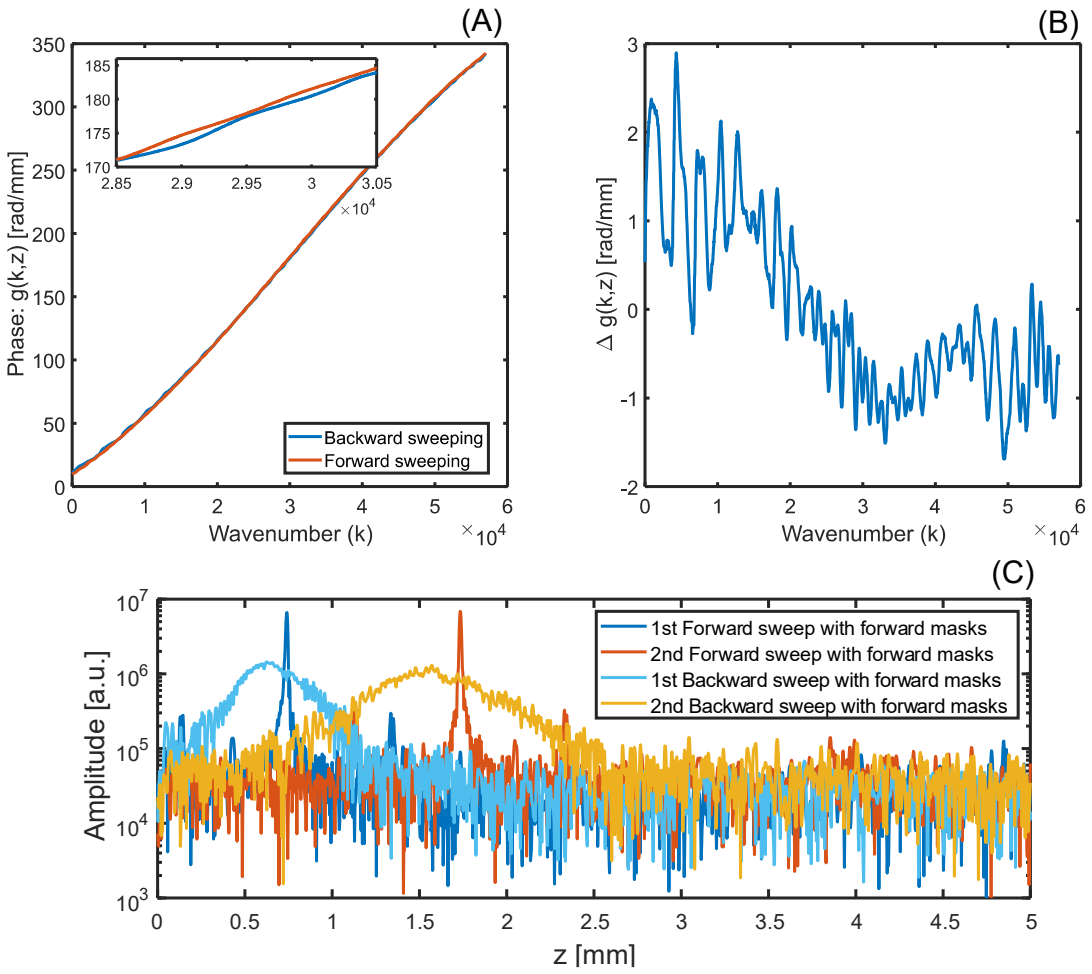

Figure 58. (A) comparison of the phase obtained from the g matrix, used for calibration of the forward and backward sweep. (B) shows the g variation between the forward and backward sweep phases in (A). (C) Four A-Scans were acquired using either a forward or a backward sweep. Each A-Scans acquired with a backward sweep have been multiplied with a theoretical forward mask, while each A-Scans acquired with a forward sweep have been multiplied with the corresponding mask (i.e., theoretical forward masks).

It is important to note that, due to the lack of temperature control, the laser exhibited drift in response to changes in room temperature. As a result, frequent calibrations were required during imaging sessions. When the room temperature was kept as stable as possible, calibration was needed approximately every hour. The laser drift could be compensated for by adjusting the frequency of the FFP-TP. However, since the PMD is also temperature-sensitive, periodic calibration was necessary. Adjusting the filter frequency had a minimal impact on OCT performance, but polarization adjustments were avoided, as they are more complex and difficult to perform.

4.1.2. Performances

As mentioned previously, the forward sweep demonstrated superior performance, hence all characterizations of the OCT setup and all unidirectional imaging were conducted using these sweeps.

The sensitivity of the interferometer used in the FDML-driven OCT imaging system was determined by analyzing the direct interference pattern. A mirror was positioned in the sample arm, and the interference from both arms was detected by the photodiode. Its amplitude, measured in

volts, and the height of the resulting A-Scan peak, measured on a linear scale, were recorded. Next, the sample mirror was deliberately misaligned to achieve approximately 15 dB of attenuation. The interference amplitude and peak height were measured again. The STD of the background noise was determined by blocking the sample arm.

The sensitivity was calculated by multiplying the unattenuated interference amplitude by the linear amplitude of the misaligned peak, then dividing this product by the attenuated interference amplitude multiplied by the STD of the background noise. The result was converted to a logarithmic scale, and the attenuation loss from the misalignment was added to yield the sensitivity value.

The sensitivity was measured with different reference arm power levels. As demonstrated in Figure 59, the sensitivity shows a plateau at ~84.6 dB around 200 µW. This plateau (instead of a distinct maximum) indicates shot noise limited performance as explained in [47]. The calculation following [8] gives a theoretical sensitivity of 86.9 dB, with a responsivity of the silicon detector at 850 nm of 0.3 A/W and a power on the sample of 1.2 mW, which was the value used for imaging. The 2.3 dB difference between the measured sensitivity value and the theoretical sensitivity might be due to inaccurate power measurements, inaccuracy in the assumed RF detection bandwidth, or to the fact that the signal is detected using dual balancing with two separate photodetectors. The maximum permissible exposure (MPE) value for a stationary, collimated beam on the cornea calculated using IEC 60825-1 and ANSI 136.1 is 0.720 mW for 850 nm [73, 74]; however, this is considering a non-scanning system. Due to continuous scanning without interruptions during an examination, the retina can be exposed with the higher average power of 1.2 mW.

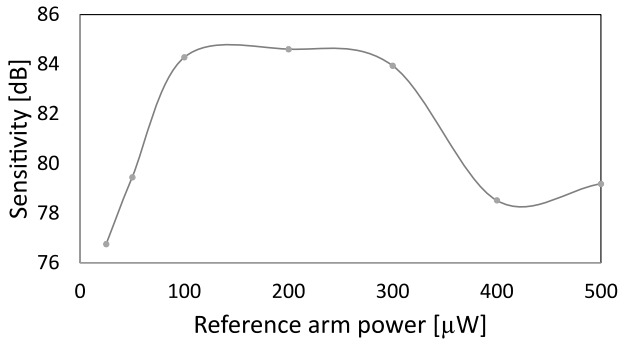

Figure 59. Sensitivity of the laser measured with different reference arm power levels. The sensitivity shows a plateau between 100 µW and 300 µW indicating a shot noise behavior.

Axial and lateral resolution have also been measured and compared with theoretical values. The axial resolution was experimentally measured when imaging the model eye, composed of a lens and a mirror as detailed in the previous sub-section. 7 B-Scans are acquired by altering the length of the reference arm by 0.5 mm optical path difference between each. The processed data was mapped from linear scale to grey scale. Figure 60 shows all peaks at different depths and a Gaussian fit of the first and last one that gives an evolution of the axial resolution from 12.8 µm to 12.5 µm. An average of 13.16 µm for all peaks is obtained over the entire range. The calculation

gives an axial resolution of 10.58 µm in air for a top-hat optical spectral shape around 840 ± 20 nm following [40]. The difference of ~2.5 µm might come from the fact that a Hanning window is used in the data processing, which will worsen the axial resolution.

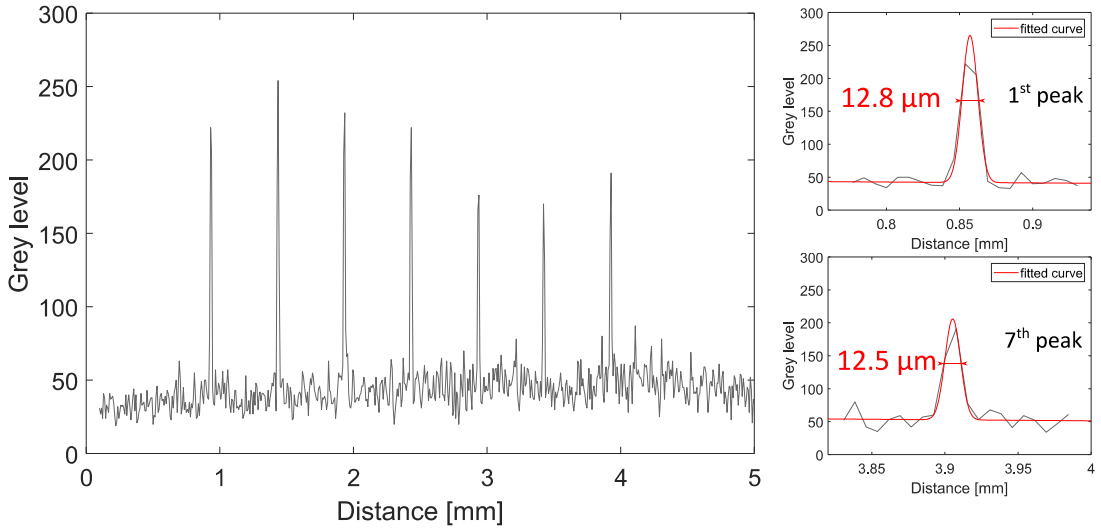

Figure 60. Axial resolution measured for 7 different depths plotted together on the same graph, showing a quasi-constant ~12.8 µm resolution over the range. An average of 13.16 µm is calculated for all depths.

A lateral resolution of 17.54 µm was measured by imaging a 1951 USAF Resolution Target (Thorlabs, R1DS1P). Please note that this measurement does not fully reflect the actual lateral resolution achievable on the retina due to aberrations introduced by the eye's lens. The effective lateral resolution is calculated to be 15 µm, given that the beam diameter at the cornea is 1.5 mm, the eye's focal length is approximately 17 mm, and M^2 is estimated at 1.2 [165]. However, this result does not account for aberrations. Considering these effects, the lateral resolution is estimated to be 25 µm.

Also, in this thesis, the oversampling parameter is defined based on the lateral resolution achieved with each system. Calculating this parameter in advance is crucial to optimizing the X-Y galvanometer scanner settings for capturing high-quality images. The lateral resolution can be measured using a USAF resolution target or estimated from the waist diameter of the collimated beam and the focal length of each lens. However, as noted previously, this calculated resolution may not fully represent the actual lateral resolution on the retina due to aberrations introduced by the eye's lens. The lateral resolution varies with the beam diameter at the cornea. Here, oversampling is defined as follows: if the field of view is 10 mm with 1,000 sampling points, each point is spaced 10 µm apart. If the system's resolution is 25 µm, the oversampling factor is defined as 2.5.

4.1.3. Images

Retinal images acquired with the 850 nm FDML laser are presented here; all imaging settings are shown in Table 6. All images were acquired on the same healthy volunteer with an optical power of 1.2 mW at the cornea. All imaging experiments presented in this sub-section were performed

at the University of Kent, where the ethical approval to image the human retina *in-vivo* was obtained. Two galvanometer scanners are used to acquire B-Scans and volumes (set-up in Figure 57).

Table 6. Acquisition settings of the OCT setup used for each figure presented in this sub-section. FOV: field of view.

Figure n°	Sweep acquisition	Oversampling	FOV (mm)	Volume rate
Figure 61 (A-B-C)	Unidirectional	2	12	n/a
Figure 62 (A-B)	Unidirectional	1.6	15.5	n/a
Figure 62 (C-D)	Bidirectional	1	12	n/a
Figure 63 (A)	Unidirectional	2	7.8	1 Hz
Figure 63 (B)	Unidirectional	1	5	10 Hz
Figure 63 (C)	Unidirectional	5	3.2	1 Hz
Figure 63 (D)	Unidirectional	2.5	4	1 Hz

Figure 61 shows the macula region of the subject acquired using the unidirectional forward sweeping of the FDML laser, which corresponds to a rate of 414,000 axial scans per second. A field of view of 12 mm with 1,000 points was captured, leading to an oversampling factor of ~2. 20 consecutive frames have been used for averaging in (A) and 5 in (C). All three brighter layers under the external limiting membrane are visible in the non-averaged image (B). Although the layers are distinguishable without averaging, a 20 times average helps to obtain a better contrast on the ganglion cell layer from the IPL and to see the external limiting membrane, as shown in Figure 61 (A).

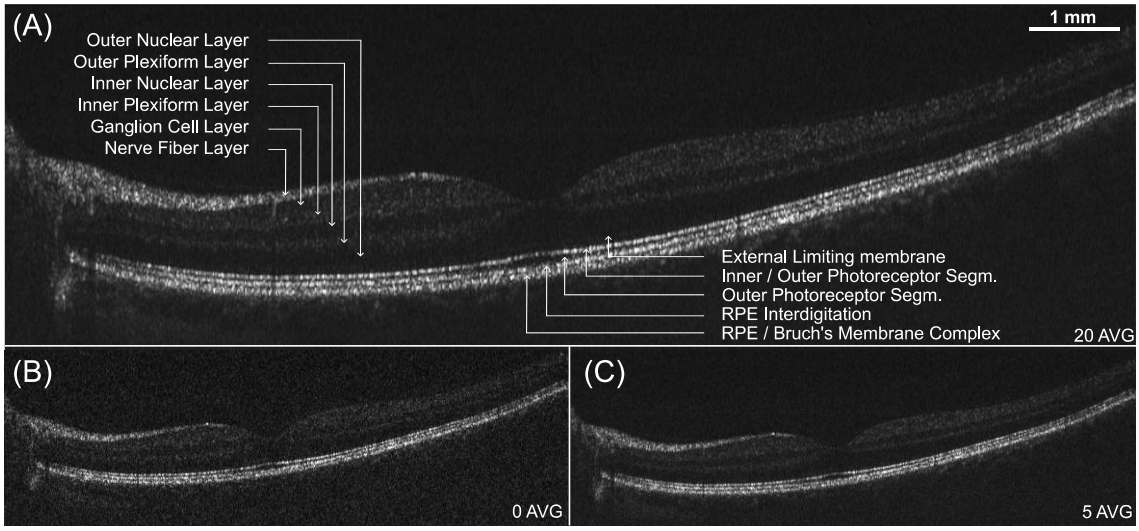

Figure 61. Retinal OCT imaging focused on the macula. (A) is 20 times averaged, (B) is obtained without average, and (C) is 5 times averaged. RPE: retinal pigment epithelium.

Wider B-Scans have been acquired by increasing the galvanometer scanner amplitude, the oversampling is hence reduced to 1.6, and the acquisition time is 5 ms. The fovea and the optic nerve

now fit within the same B-Scan image, as shown in Figure 62. Figure 62 (B) is an unaveraged frame of the averaged image stack in (A). The three brighter layers under the external limiting membrane can again be appreciated, as well as the choroid. Figure 62 (C) and (D) are acquired using the bidirectional sweeping of the filter, which corresponds to 2 × 414 kHz, resulting in an A-Scan rate of 828,000 per second. All layers depicted in the previous imaging can still be seen at this higher repetition rate. However, as mentioned in section 4.1.1, two sets of *g* and *h* were used, one for each sweep. This led to a slight frequency shift between the forward and backward A-Scan. A correction of 3 pixels is applied to each backward sweep, leading to the images (D) in Figure 62. Image correction has such a small impact on the visibility of layers that it is not discernible.

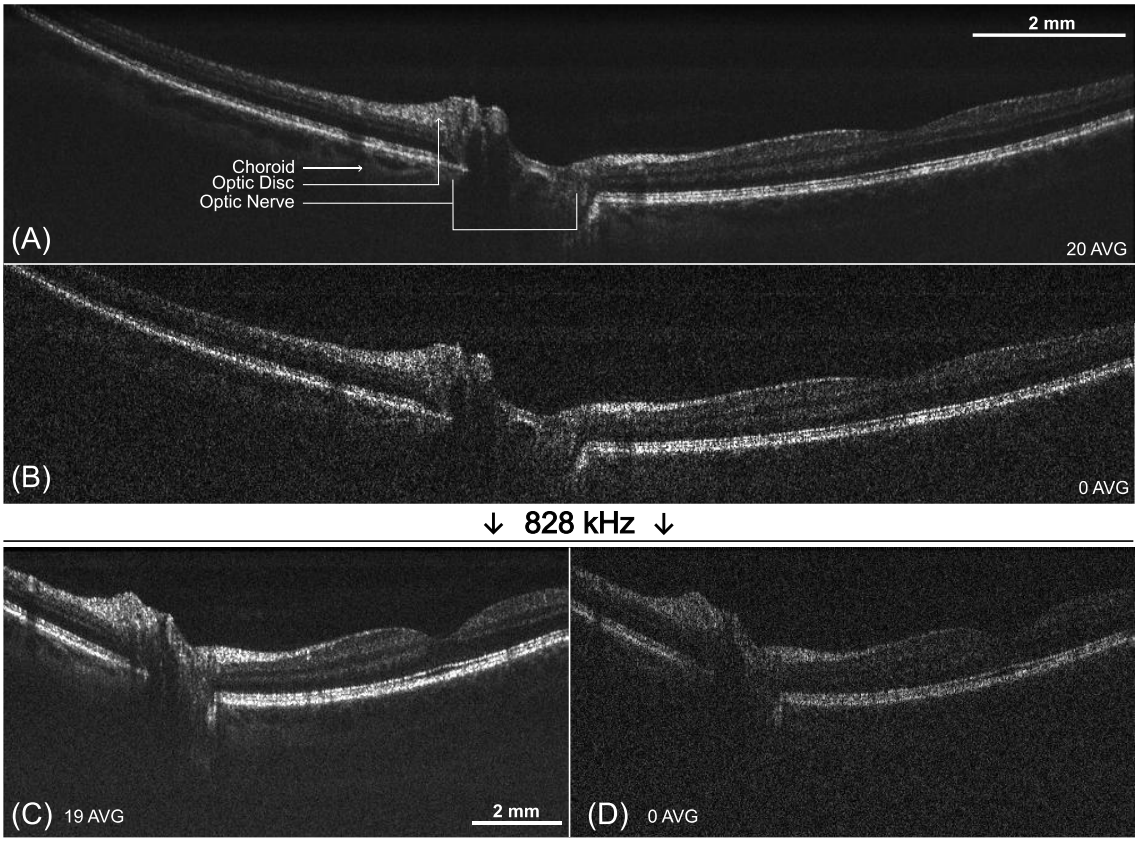

Figure 62. Widefield retinal images of the optic nerve and the fovea. (A) and (B) are acquired at a rate of 414,000 axial scans per second, 20 times average and non-average, respectively. (C) and (D) are acquired using the laser's bidirectional sweeping, leading to a rate of 818,000 axial scans per second. (C) is 19 times averaged, and (D) is non-averaged.

En-face OCT, similar to confocal or fundus images and 3D images, are presented in Figure 63. The fundus images are obtained by averaging all *en-face* OCT images together [166]. In (A), an average of 8 such equivalent confocal images obtained from 8 distinct volumes show the optic nerve and the macula. Each of the 8 volumes took 1 s, and the fast and slow scanners were driven at 200 Hz (triangular) and 1 Hz (sawtooth) frequency, respectively. The CMS approach employed here allowed for *en-face* OCT and confocal images to be displayed in real-time. For instance, Figure 63 (B) has been acquired in 100 ms. The volume (B) and (D) have been flattened in post-

processing for a better rendering. They are presented with three *en-face* images separated each by 10 frames. In each image, vessels can be seen, as well as smaller capillaries.

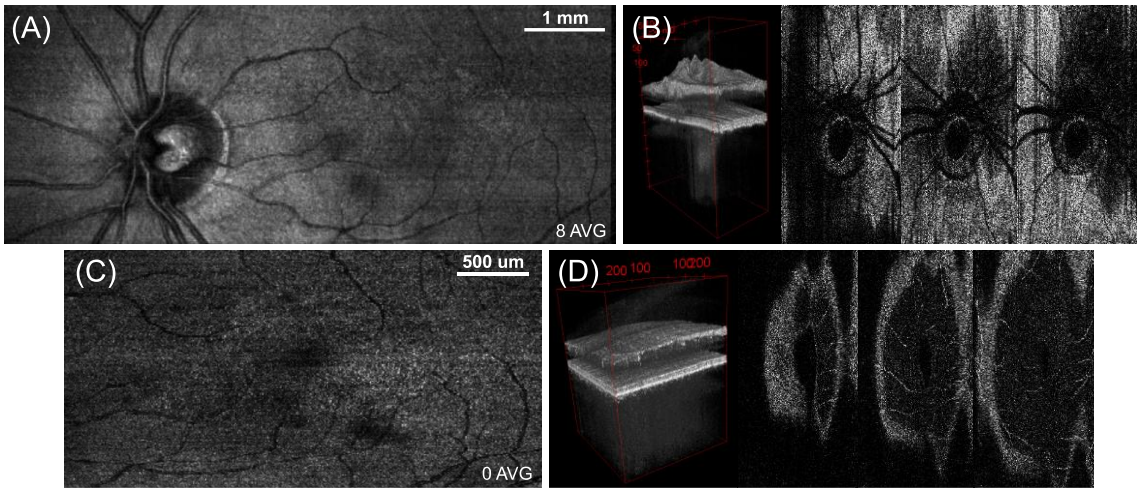

Figure 63. En-face OCT and confocal images of the optic nerve and the macula regions acquired at a rate of 414,000 axial scans per second. (A) 8 times averaging of confocal images of the optic nerve and the macula. (B) flattened 3D of the optic nerve with 3 corresponding en-face spaced by 10 frames. (C) confocal images of the macula. (D) flattened 3D of the macula with 3 corresponding en-face spaced by 10 frames.

4.2. Single-*k*-calibration imaging technique

A detailed description of this calibration technique to practice OCT can be found in 2.1.2. All following experiments have been taking place at the university of Lübeck where this calibration technique is mostly used.

4.2.1. Setup

Before starting an imaging session with the single-*k*-calibration technique, the laser has been temperature controlled, and dispersion compensated. The temperature control of each component is detailed in 3.3.2. This ensures better stability of the laser over time and does not require several calibrations over an imaging session as indicated in 3.3.4. The dispersion compensation attained by this stage of the laser can be seen in Figure 51 right. The frequency of the FFP-TF is set by reducing the noise in the OCT imaging preview software.

The output from the laser is entering a booster stage that includes a bufferstage enabling a sweep repetition rate of 1.7 MHz. A circulator is employed here as an isolation component to protect the laser from back reflections. This specific circulator was chosen for its ability to block light along one axis, providing greater control over PMD. Notably, the output signal from the laser can be significantly degraded by PMD effects in the booster stage, and this circulator helps mitigate that issue. It features a PM780 fiber at the input and an Hi780 fiber at the output.

The buffer stage consists of two sections, 4x and 2x. The first section copies each main sweep exiting the laser immediately after it. The original sweep lasts 588.148 ns, while the copied sweep is delayed by 588.37 ns – an adequate delay, though it exceeds the ideal 588.148 ns by 0.222 ns, equivalents to an exceeding amount of fiber in the 4x stage of 4.6 cm. This delay creates a small

gap between each sweep, avoiding overlap, but without a delay so large that it causes misalignment with subsequent sweeps. Each stage must have enough space to accommodate all copied sweeps without interference. In the second stage, the 2x, the delay exceeds the ideal by 0.496 ns, equivalent to 10.2 cm of fiber. This second stage prevents any sweep overlap. Also, during development several fiber length adjustments of the laser cavity were performed resulting in different fundamental frequencies making a perfect buffer length impossible. However, as the number of stages increases – such as with a five-stage configuration to buffer 32 copies – the required precision in fiber cutting becomes significantly greater. Another technique modulating slightly under the duty cycle one wants to reach, for instance 23% could also be used to avoid overlapping.

Polarization controllers are placed before each fiber spool in every stage to ensure uniform polarization across all copied sweeps. This is essential, as all sweeps will subsequently be amplified by a booster (SOA_2, Superlum Ltd., SOA-372-SM), which is polarization-dependent. The booster raises the light intensity to achieve a sample power of 720 µW, consistent with IEC 60825-1:2014 standards. The system is classified as a Group 1 ophthalmic instrument in accordance with DIN EN ISO 15004-2:2007 Section 5.2 (c), presenting no potential light hazard. Ethical approval for *in-vivo* retinal imaging in human subjects was obtained from the University of Lübeck for this sample power level.

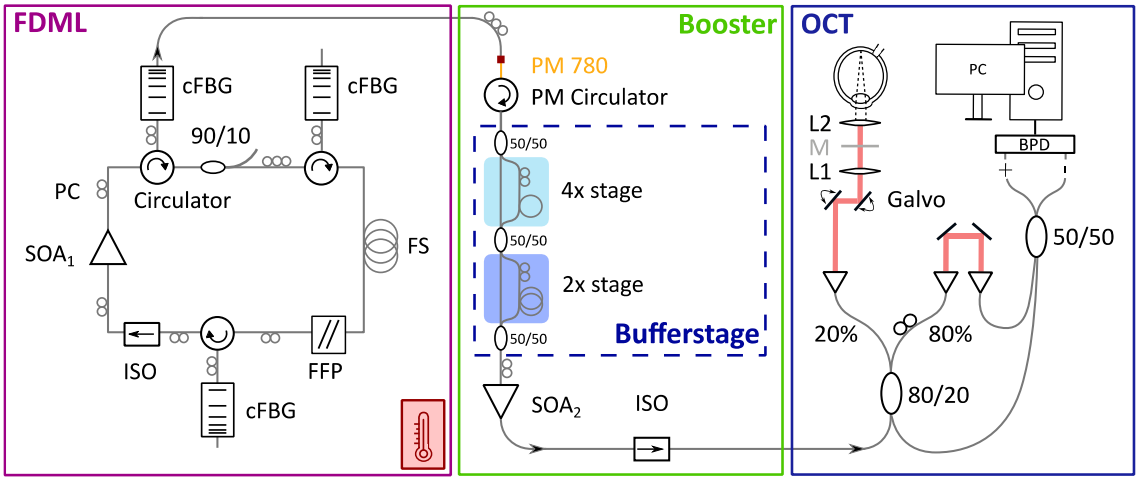

Figure 64. Schematic of the experimental setup, from the FDML laser to the imaging system. The FDML laser is temperature controlled (indicated by the red thermometer icon). A PM circulator isolates the laser from the booster stage. The buffer stage (two sections: 4x and 2x) increases the laser repetition rate to 1.7 MHz, given its 25% duty cycle. Each 50/50 coupler splits and then recombines sweeps, with fiber spools for sweeps delays and polarization controllers to align polarization. SOA_2 boosts the power to 720 µW on the sample, while an isolator further protects the booster from back reflections. The amplified output is directed into sample and reference arms, split by an 80/20 coupler, recombined by a 50/50 coupler, and detected by a balanced photodetector (BPD).

The OCT setup is comparable to the one developed at the University of Kent as shown in Figure 64. The same fiber collimator and photodiode are used. Both galvanometer scanner mirrors are also from Cambridge Technology but are from a slightly different model: 6215H. The position of the pivot point and the focus can be adapted by manual mechanical stages, no pupil tracking is used here. As shown in Figure 65, the 4 mm beam diameter of the collimator is reduced to a 2 mm

beam diameter using two spherical lens systems, each consisting of four individual lenses. The collimated beam is initially deflected by galvanometer scanners, then focused by the first lens, L1 (focal length of 75 mm), onto a gold mirror, labeled M in Figure 64 and Figure 65. The beam undergoes a 90° reflection off the mirror – this angle is not shown in the schematic for simplicity. After reflection, the beam is recollimated by lens L2, which has a focal length of 37.5 mm, producing a final beam diameter of 2 mm at the cornea [167, 168]. The spot size on the retina depends on the choice of the subsequent focusing lens, such as the human eye lens or a simple focusing lens. For instance, with a 17 mm focal length lens corresponding to the lens of the human eye, the spot size on the retina with a $M^2 = 1.2$ would be 11 µm. However, considering the aberrations in the eye, the lateral resolution is estimated to be 20 µm.

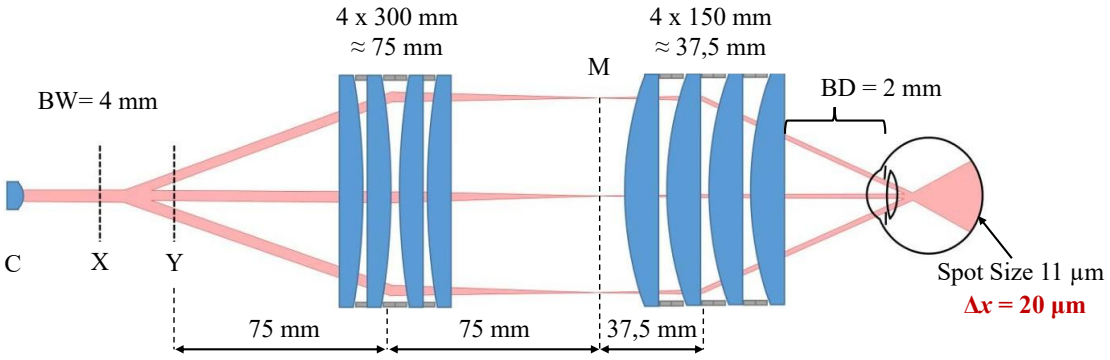

Figure 65. Optical setup of the OCT sample arm, updated from [42]. Each spherical lens is composed by four individual lenses. C: collimator, X, Y: galvanometer scanner, BW: beam waist, M: mirror, BD: beam diameter, Δx: estimated lateral resolution.

The ADC card's sampling rate was set to 2 GHz due to the narrow bandwidth of the laser output, making higher rates like 4 GHz unnecessary. This results in a Nyquist frequency of 1 GHz, which is lower than the typical RF bandwidth (1.6 GHz) of photodiodes used in OCT systems. To prevent high-frequency components, such as RIN, from aliasing back into the signal, a 780 MHz low-pass filter is placed between the balanced photodetector and the acquisition card. Although the photodetector in this setup has an RF bandwidth of 600 MHz - making the filter potentially redundant - it is retained as a precautionary measure.

For calibration, a model eye is used, consisting of a 50 mm focal length lens (LA1131-B, Thorlabs) and a flat gold mirror. After system calibration with the mirror, a sample eye, referred to as the 'EVA eye,' was employed. This model includes a lens, silicone, and a retina-mimicking sample (Modell-Augen Manufaktur), designed to closely replicate the properties of a human eye. To assess system performance, both *in-vivo* and *ex-vivo* images were acquired with two volunteers and using the EVA eye respectively. Both results are presented in subsequent sections.

4.2.2. Performances

In Section 4.1.2, the sensitivity of the system was measured using a slightly modified technique. The method used here is illustrated in Figure 66. All A-Scans within a B-Scan are averaged in

linear space, and the averaged background, calculated across all B-Scans, is subtracted from this averaged A-Scan. The resulting data is then converted to decibels (dB), and the index *i* of the highest peak in this graph is identified. Using this peak index, the biased sensitivity is calculated by dividing the averaged A-Scan, after background subtraction, by the standard deviation of the background noise. To determine the sensitivity, the system's initial attenuation (used to prevent saturation during measurement, optical density (OD) of the filter used) is subtracted from the calculated SNR. This provides the sensitivity in dB, representing the system's ability to detect faint signals.

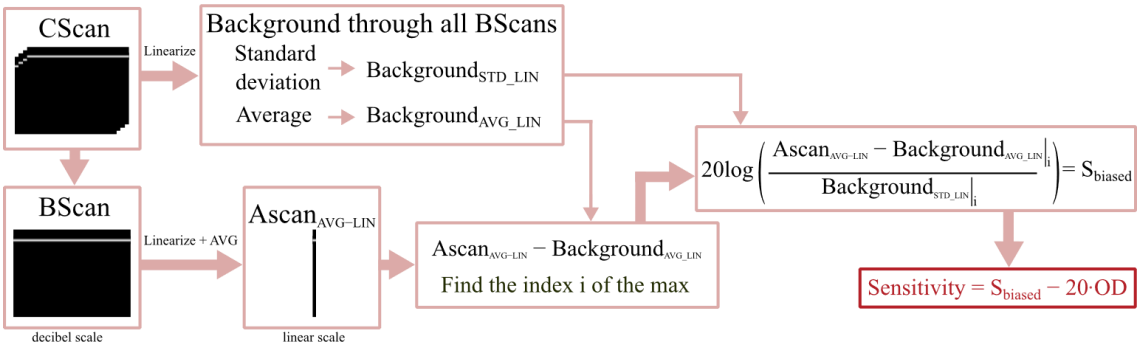

Figure 66. Sensitivity calculation. From a C-Scan acquisition, a unique A-Scan is extracted by averaging all A-Scans of a single B-Scan. The average of the background is subtracted from this A-Scan. On another side, the standard deviation of the background is calculated. The sensitivity is finally obtained by dividing both terms and by subtracting the attenuation of the optical density (OD) filter.

To perform the sensitivity measurement, the current of the booster amplifier following the laser is adjusted so that the sample mirror receives 720 µW of power, resulting in approximately 100 µW of power on the photodiode from the sample arm. At its maximum, the reference arm delivers ~400 µW of power to the photodiode. To avoid saturation, an 0.8 OD filter is placed all along in the sample arm, reducing the power by 22.5% each way (as the light travels along the same path twice). For each measurement set, after optimizing the power in the reference arm, a calibration spectrum and a background measurement are taken. Once the system is calibrated, a sensitivity measurement is conducted.

To measure the sensitivity at several reference arm powers, the sample arm is shuttered allowing only the power from the reference to be measured with a power meter. The measurement is done using the port normally going to the balanced photodiode. The power level of the reference arm is adjusted by manipulating an iris positioned in the free-space beam path of the reference arm to analyze which power level provides the highest sensitivity. After adjusting the power, the measuring port is carefully reconnected to the balanced photodiode to obtain a flat signal, indicating proper balancing of the system. A background measurement is then acquired. A supplementary OD filter of 1.3 (transmission of 8%) is placed in the sample arm and the sensitivity can be measured after opening of the sample arm. It is important to acquire a new background for each power level since the intensity noise will change accordingly, however most of it can be compensated by the background subtraction.

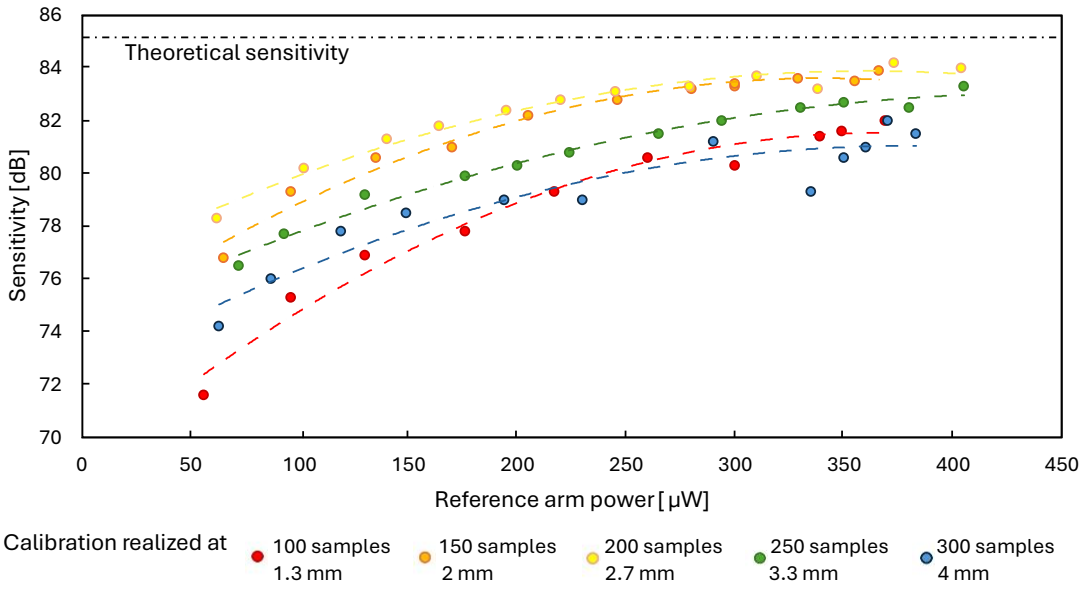

Figure 67. Sensitivity measured with different reference arm powers with a calibration realized at 5 different depths.

Figure 67 shows that the highest sensitivity is achieved consistently when the reference arm power is between 300 µW and 400 µW. The figure also indicates that the calibration position has a strong influence on the achieved sensitivity. When calibration is performed either too close to zero frequency (at 100 samples) or too far away (beyond 250 samples), the maximum sensitivity decreases from the shot-noise-limited value of 84 dB (measured at 150 and 200 samples) to around 80 dB.

The theoretical value of the sensitivity has also been calculated following [8]. With a sample power of 720 µW, a sweep repetition rate of 1.7 MHz, and a photodiode responsivity of 0.3 A/W, the sensitivity is calculated to be 85.2 dB. The 1.2 dB difference between the theoretical and experimental values may be attributed to the fact that the signal is detected using dual balancing with two separate photodetectors as mentioned previously.

The lateral resolution has been measured using a 1951 USAF target and a focusing lens of 50 mm focal length. Since group 5, element 6 have been resolved, this led to a lateral resolution of 17.54 µm, as measured at the university of Kent. As mentioned previously, note again that this does not fully reflect the actual lateral resolution achievable on the retina due to aberrations introduced by the eye's lens. For simplicity in calculation, Δx is estimated to be 20 µm.

The axial resolution was determined by imaging a gold mirror positioned behind a 50 mm focal length lens. A single B-Scan was acquired at five distinct depths, separated by 1 mm intervals. The first 50 A-Scans from each B-Scan are fitted with a Gaussian fit to measure the FWHM, meaning the axial resolution, for each peak. The average of the 50 FWHM values at each depth is taken and displayed alongside a single A-Scan at each corresponding depth in matching colors, as shown in Figure 68.

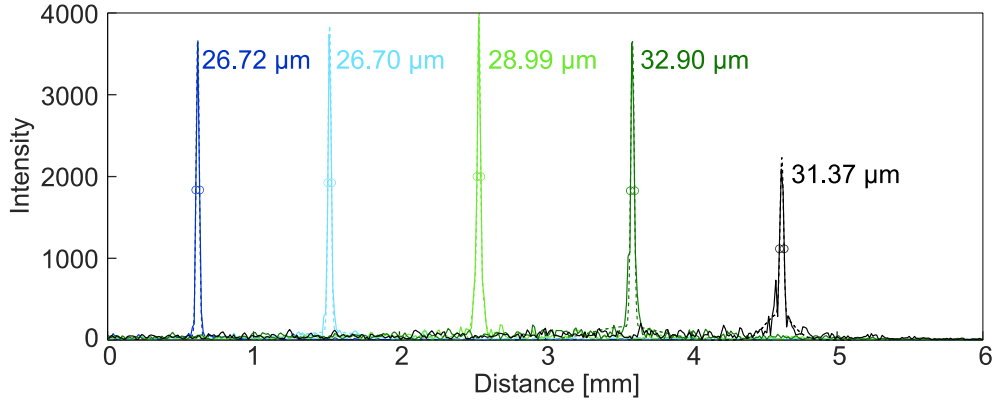

Figure 68. Axial resolution measured at five different depths, with an average resolution of 29.34 µm across the whole range. Each peak is fitted with Gaussian fits shown as dashed lines in matching colors. Each axial resolution number given at each depth is the results of an average over 50 A-Scans.

Figure 68 demonstrates an average axial resolution of 29.34 µm over a range of 5 mm. The measured laser bandwidth is 30 nm, which, according to equation (9), would typically correspond to a resolution of 14.45 µm. However, this theoretical value assumes the maximum bandwidth occurs within the -3 dB region. Due to the shape of the ASE of the SOA (Figure 25), it is challenging to achieve the full 30 nm bandwidth within this 3 dB range. With the current resolution of 29.34 µm, this would equate to a bandwidth of 14.78 nm at 3 dB, which does not fully align with the laser's output spectrum presented in Figure 50 right. Additionally, the use of a Hanning window in data processing, the calibration method and the presence of ripple could also contribute to the reduced resolution. While this non-ideal axial resolution may limit the sharpness of retinal images, as observed at the University of Kent, most retinal layers remain clearly visible. The images showcasing these layers are presented in the following section.

4.2.3. Images

Retinal images presented in this section have been acquired with the 1.7 MHz 850 nm FDML laser. All imaging experiments presented in this sub-section were performed at the University of Lübeck, where an ethical approval to image the human retina in-vivo was obtained for an optical power of 0.720 mW at the cornea. All images were acquired on two healthy volunteers and on a sample eye called EVA. As mentioned in 4.2.1, the lateral resolution is estimated to be around 20 µm. This factor is used here to calculate the oversampling parameter. All imaging settings for each image are shown in Table 7, the oversampling parameter, the field of view (FOV) and the volume rate in the case of the presentation of a volume data.

Table 7. Acquisition settings of the OCT setup used for each figure presented of this sub-section. FOV: field of view.

Figure n°	Sample	Oversampling	FOV (mm)	Volume rate
Figure 69 (A-D)	EVA	5	24	n/a
Figure 69 (E-F)		2	16	
Figure 70 (A-E)	Subject 1	4	17 x 8	0.4 Hz
Figure 71 (A-B)		6	4.8	n/a
Figure 71 (C)		5	5 x 5	1 Hz
Figure 71 (D-E)		5	22	n/a
Figure 72 (A-E)	Subject 2	2.8	11 x 7	1.2 Hz

Figure 69 presents images acquired on EVA, using two different power levels. A power level of 1.22 mW matching the setting used previously in Section 4.1.3 at the University of Kent, while 0.720 mW corresponding to the maximum *in-vivo* power level utilized at the University of Lübeck. For each power setting, a volume was acquired, at two specific regions within the volume shown below: one focused on the macula and the other displaying an alternate retinal region, highlighting different structural features. Each region includes a 10-frame averaged image (A, C, E, G), alongside a single frame from each volume (B, D, F, H) positioned below.

These images – both single frames and averaged frames – allow for the observation of multiple layers within the sample eye. Averaging enhances the visibility of each layer, although with higher power levels, all structures visible in the averaged images are also discernible in single frames. For the lower power setting, however, deeper layers are challenging to distinguish without averaging. Additionally, the higher power dataset reveals deeper structures, demonstrating the advantage of increased power on the sample: the higher the power, the more details become easily visible.

Figure 69 (E) and (F) show a reflection above the retina in the top right corner of each image. This reflection results from the silicone layer in the EVA model, which mimics the vitreous humor between the lens and the retina. Since silicon and retina are not fully in contact, an ultrasound gel should be applied at their interface to ensure index matching. Without adequate gel, a significant portion of the signal reflects off this layer instead of reaching the retina. In this instance, a lack of gel at that position caused the reflection, though it had minimal impact on the retinal imaging. Additionally, the optical focus must be adjusted precisely on the retina, not the silicon.

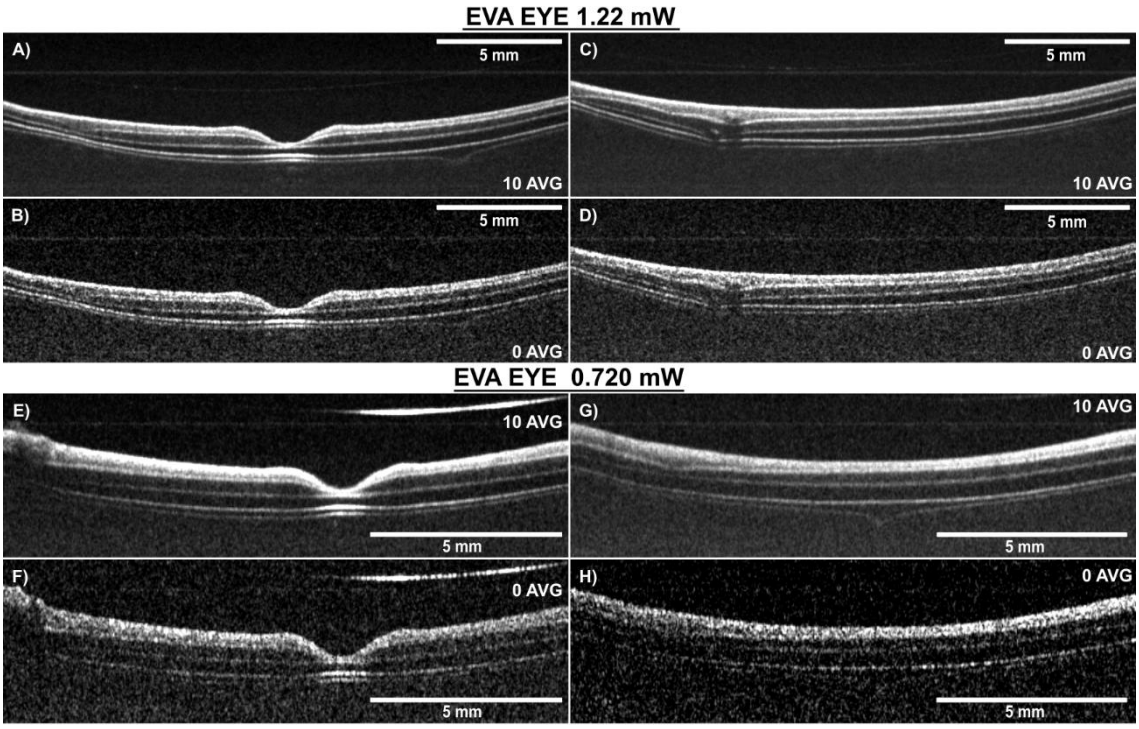

Figure 69. Retinal OCT imaging of the sample eye EVA across two sessions with varying optical power settings. (A-D) show images obtained at 1.22 mW at the cornea, while the bottom row (E-H) represents imaging at 0.720 mW, aligned with MPE for in-vivo imaging. In each session, two regions were extracted from the same volume: one centered on the fovea and another isolated view of the retina. For each region, both a 10-frame average and a single B-Scan are displayed.

Figure 70 displays *in-vivo* retinal OCT images from a single volume, presented as a 3D rendering in D). Panel A) shows a single frame extracted from the 5-frame average in B), both of which highlight the fovea and optic nerve of Subject 1. Several retinal layers are visible, though the image appears relatively dim, with limited axial resolution that prevents clear observation of the three layers of the RPE. Panel C) presents a 10-frame average at a slightly different position than A) and B), demonstrating that additional averaging does not significantly enhance or reveal more details of the sample. This volume was acquired in 2.5 seconds, which explains the slight eye movement, especially noticeable along the slow axis in D), where ripples caused by subject motion are evident. By halving the oversampling rate, the volume could be acquired twice as fast, reducing sensitivity to patient motion with minimal impact on lateral resolution. However, when viewing the *en-face* image – calculated using the standard deviation between each horizontal frame – minimal patient motion artifacts are discernible, as shown in E). Also, E) highlights by a blue dotted circle a black spot. This could initially be interpreted as an anomaly in the subject's retina. However, in Figure 71 C), which corresponds to the orange dotted frame in Figure 70 E), the same black spot is visible, though at a different position within the same retina. Additionally, the black spot is visible in Figure 72 A), top right, corresponding to another subject, and has also been observed in the sample eye, though not shown here. This suggests that the black spot may be due to debris on the optics, possibly on one of the mirrors or lenses.

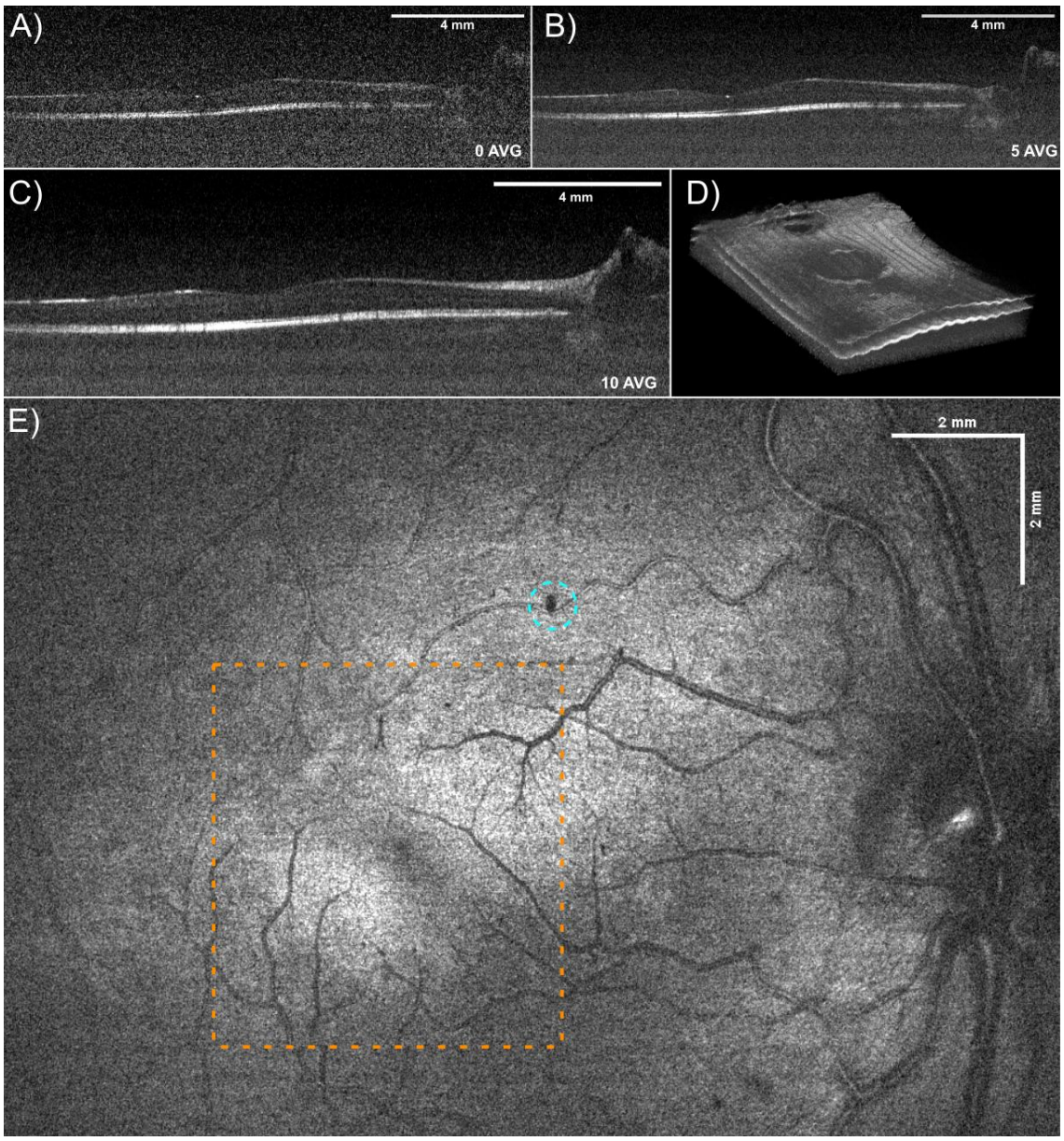

Figure 70. Retinal images from the volume shown in D). B) displays a 5 times average B-Scan, where both the fovea and optic nerve are visible. A) is a single frame from B). C) presents a 10-frame average. E) provides an en-face view of volume D) calculated using the standard deviation between frames. The blue dotted circle marks an anomaly on the retina, while the orange dotted frame corresponds to the area highlighted in Figure 71.

Figure 71 presents additional retinal images of Subject 1. These images are narrower and focus either on the fovea or the optic nerve. In panels A) and D), a 20-frame average reveals the IPL and Outer Plexiform Layer (OPL) more clearly than in Figure 70. These layers are also visible in panel B), a single frame extracted from A). For panels A) and B), the Y-scanner was switched off to scan the same position repeatedly, aiming to improve contrast through averaging. This adjustment resulted in enhanced contrast in the IPL and OPL. In panel D), a portion of the choroid is visible adjacent to the optic nerve. Panel C) shows an *en-face* image of a volume centered on the fovea highlighting the black spot.

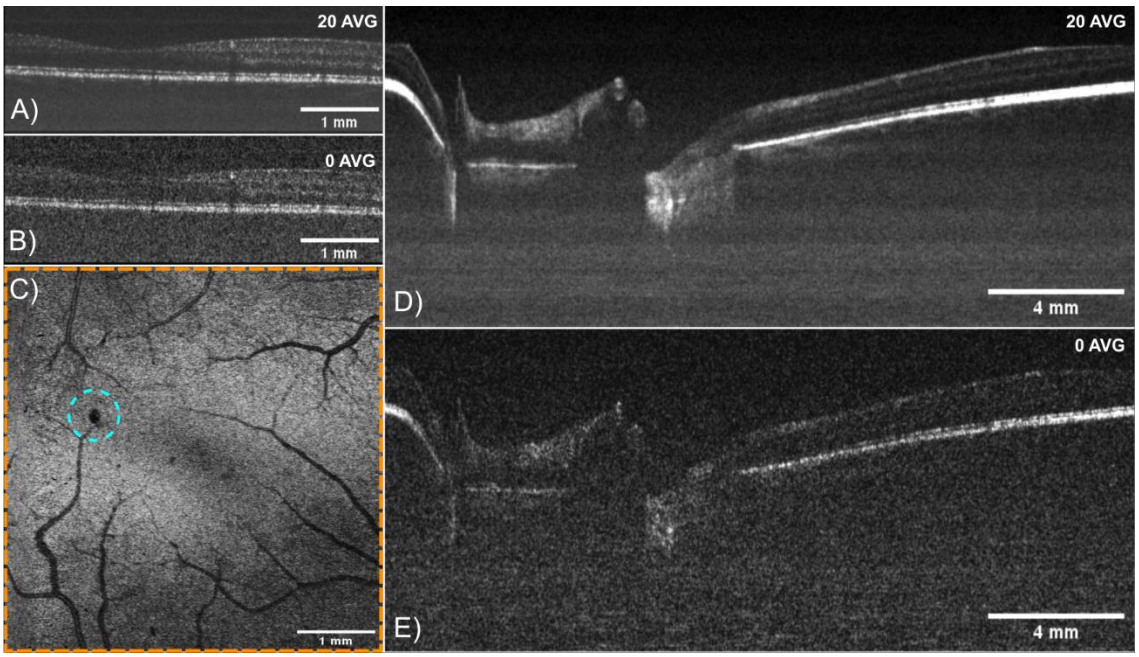

Figure 71. Close-up images focusing on either the fovea or the optic nerve. (A) shows a 20-frame average, with (B) displaying a single frame from (A). (C) represents the en-face (calculated by standard deviation between each frame) of a different volume, identifiable in Figure 70 by the blood vessel patterns. (D) is a 20-frame average, while (E) presents a single frame from (D). The same blue dotted circle marks an anomaly on the retina at another position.

The final imaging session, shown in Figure 72, presents a volume acquired from Subject 2. Two 3D renderings are displayed in panels D) and E). Panel A) shows the *en-face* image calculated using the STD. Panels B) and C) display orthogonal views of the volume, with the orange markers indicating positions in A). Panel B), corresponding to the slow scanning axis, reveals some subject motion, as the retina appears less smooth than in C). However, the movement observed is less pronounced than the ripple seen in Figure 70 D). This volume was acquired in less than one second, which likely explains the reduced motion artifacts. The stability of the images also varies depending on the subject. To minimize motion artifacts, faster scanning would be beneficial, which goes in hand with even faster lasers. While subject motion can be corrected during post-processing, the movements in this case are minimal enough that the entire volume can still be appreciated without correction in real-time imaging.

However, the volume quality might be impacted by the quality of the calibration. In this dataset, two lines are visible in panels B) and C), which result from this calibration. The characteristics of the laser can vary from day to day, potentially affecting the imaging quality. It is likely that increased ripple in the system could disrupt the calibration, leading to the appearance of these lines. In B-Scan renderings, the lines are not particularly problematic. However, in the 3D rendering, since the lines are positioned above the volume, they may obscure retinal features beneath, as shown in panel (D), where the lines, corresponding to planes in volumes, cover nearly the entire volume.

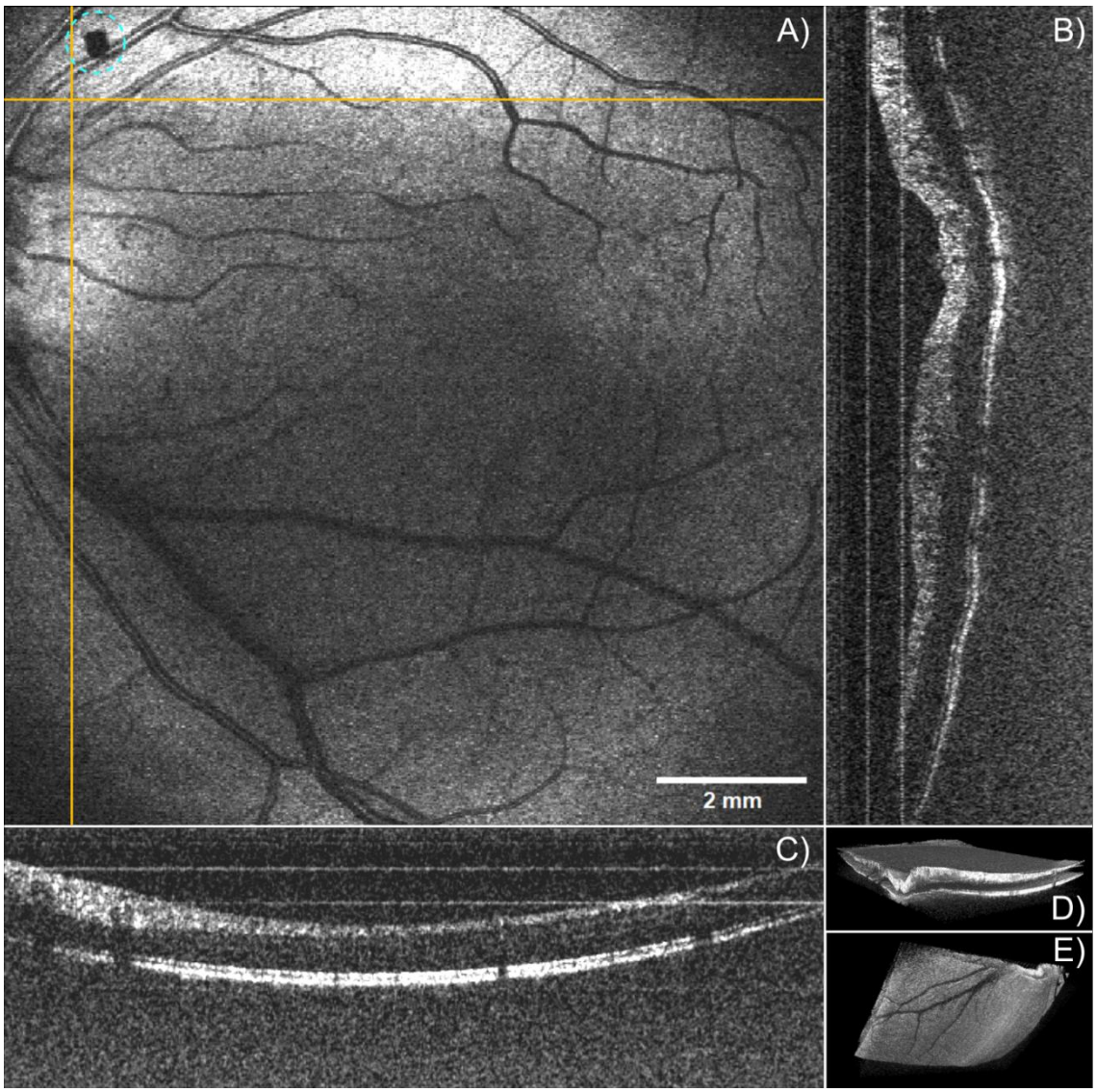

Figure 72. Retinal OCT imaging showing the fovea and the blood vessels of the retina of subject 2. A) shows the en-face of the volume, calculated by standard deviation. Orthogonal views are presented in B) and C). D) and E) show a 3D volume of the acquired data. The same blue dotted circle in A) marks an anomaly on the retina at another position.

4.3. Imaging comparison

This section compares different ophthalmic SS-OCT imaging results. First, it compares the results obtained in this thesis, the one from the University of Kent and from the University of Lübeck. Both sets of results were acquired using the same laser but at different stages of development, which led to varying characteristics, except the center wavelength which remains ~850 nm. Additionally, the two institutions used different calibration methods, which will also be discussed.

The second part of the section focuses on a comparison of retinal imaging at two different wavelengths: 850 nm and 1060 nm. For this comparison, only images obtained with FDML lasers are considered, which includes the images presented in the chapter 4 for 850 nm and results from previous group members at the University of Lübeck, who used and developed 1060 nm FDML lasers. A conclusion on the imaging potential and outlook is then given.

4.3.1. Comparison of 850 nm SS-OCT with FDML laser

In this section, both systems from the University of Kent and the University of Lübeck are compared, from their setups to the images obtained. As detailed in previous sections, the laser was at different stages of development at each location. In Kent, the setup lacked temperature control, sweet-spot tuning, and used coarse chromatic dispersion compensation. It could image with an axial scan rate of 414 kHz or 828 kHz in bidirectional OCT. In Lübeck, the laser was more advanced, with precise temperature control, a sweet spot over half the bandwidth, and an axial scan rate of 1.7 MHz. However, the bandwidth was reduced by 10 nm due to modulation requirements. Since modulation was set to 25%, filter amplitude was increased by ~30% – while limiting this increase to protect the filter – resulting in a final bandwidth of 30 nm.

In both systems, the laser output passes through a secondary SOA to boost the power to levels sufficient for the sample, 1.2 mW for Kent and 0.720 mW for Lübeck. However, in the case of the Lübeck setup, the laser output also passes through a bufferstage before reaching the booster SOA, which increases the optical losses. It then reduces the optical power before amplification, meaning that the SOA may not operate in saturation in this setup. Nonetheless, any noise introduced by the SOA should be effectively compensated by the dual-balanced detection system, which helps to maintain a high signal-to-noise ratio and minimize the impact of the noise from amplifiers.

Once the signal is amplified, it enters the OCT setup, which is comparable in both systems. The same couplers, reference arm, and photodiode are used in each case. The only difference lies in the sample arm configuration, which affects system sensitivity due to varying levels of optical loss between the two setups.

Two key factors that influence image quality are the laser's sweep repetition rate and its bandwidth. The laser used at the University of Kent features a wider bandwidth and a slower sweep rate, which contributes to a better axial resolution and higher sensitivity, as demonstrated in Table 8.

Table 8. Parameter summary of both imaging setup at the university of Kent and Lübeck.

Parameter	**Kent**		**Lübeck**	
Repetition rate	414 kHz	828 kHz	1.7 MHz	
Calibration method	CMS		Single-*k*-calibration	
Power on sample (mW)	1.2		0.720	1.22 (EVA)
Sensitivity (dB)	84.6		84	
Axial resolution (µm)	12.8		29.34	
Lateral resolution (µm)	17.54		17.54	

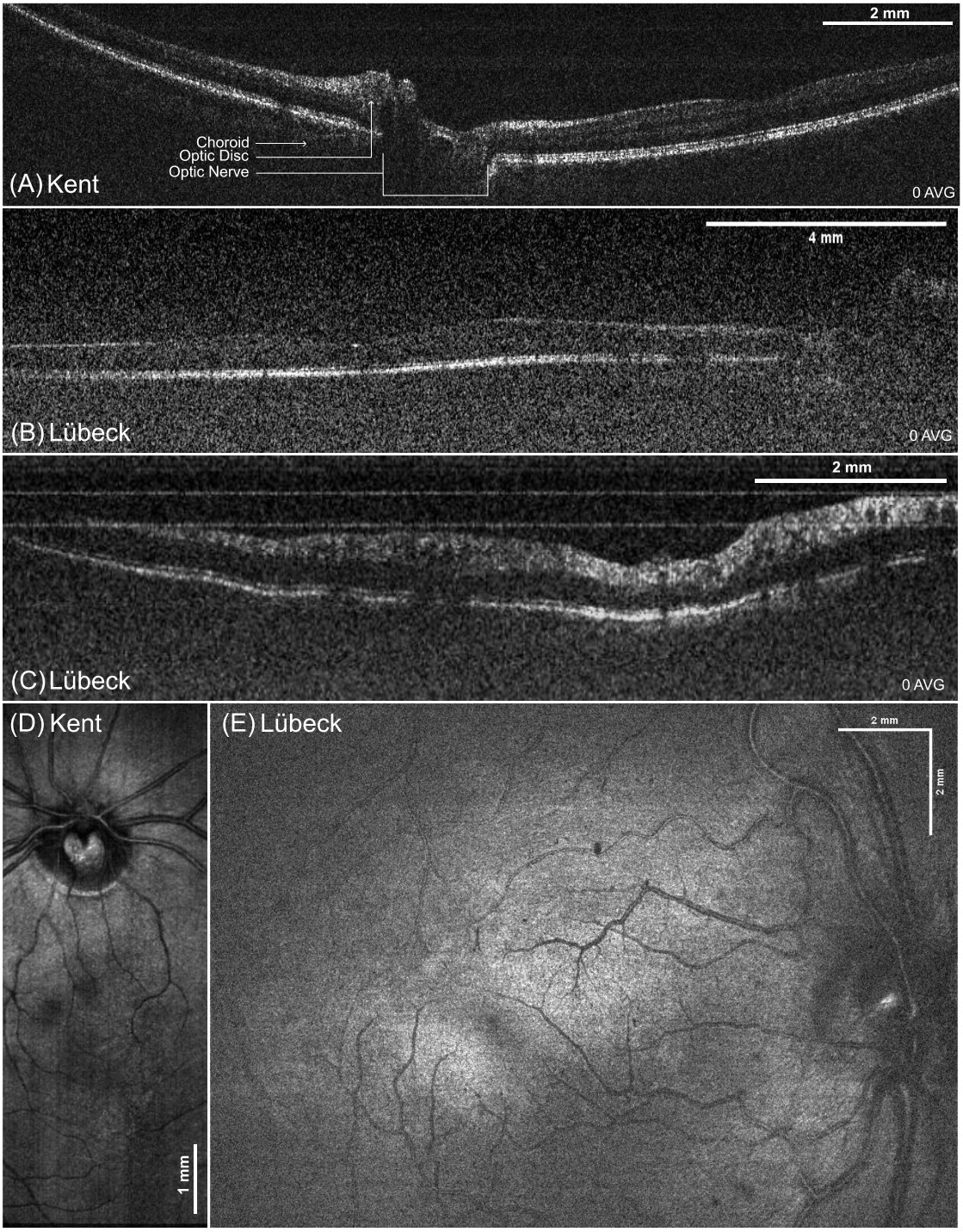

Figure 73. Comparison of retinal images obtained at the University of Kent (A, D) and the University of Lübeck of subject 1 (B, E) and of subject 2 (C). Panels (A) and (B) display the optic nerve and fovea without averaging, while (C) present an orthogonal view displaying an area close to the optic nerve. Panels (D) and (F) present en-face images of the optic nerve and fovea.

These improvements in axial resolution and sensitivity are evident in Figure 73 (A), where finer details and enhanced contrast in the retinal layers are more distinct compared to (B) and (C). These last two images (B) and (C), although acquired using the same setup and power, exhibit noticeably different contrasts. This may be due to better focus in image (C). Additionally, the images capture different subjects, which could influence the results. Despite this, both images display similar axial and lateral resolution. It is important to note that a higher power level was

used in the Kent system, which contributes to increased sensitivity. A comparison conducted at the University of Lübeck on the EVA eye, using power levels of 0.720 mW and 1.22 mW comparable to the one used in Kent, demonstrated that higher power enhances the visibility of deeper structures and makes the upper layers more distinguishable – advantages that are reflected in the results from the University of Kent, shown in the images below. Nevertheless, the power level does not affect axial resolution, which is notably superior in the Kent system.

The complex Master-Slave calibration method demonstrates superior performance in achieving more accurate calibration, resulting in consistent axial resolution across depth compared to the single-*k*-calibration. This approach is particularly beneficial for noisy lasers, where precise calibration is critical. On the other hand, the single-*k*-calibration remains highly effective for commercial or, in general, ultra-low noise FDML lasers.

To compare the *en-face* images in Figure 73, image (C) was acquired at a volume rate of 1 Hz, while image (D) was captured at a slower rate of 0.4 Hz. The longer acquisition time for image (D) is due to its wider FOV and higher oversampling. In the Lübeck setup, the faster laser operating at 1.7 MHz enables rapid image acquisition, but the increased oversampling and larger scan area slowed the process. Both images show similar lateral resolution, resolving the same types of vessels. To fully leverage the speed advantage of the laser, oversampling should be optimized to balance detail and efficiency, ideally not exceeding three times. Additionally, the faster acquisition speed makes the imaging process less sensitive to patient motion.

4.3.2. Comparison of 1060 nm and 850 nm SS-OCT with FDML laser

To start, there are notable technical differences between the two wavelengths used for SS-OCT imaging. A significant challenge with the 850 nm wavelength is that the scanning line becomes clearly visible to the eye during imaging. This bright line can cause the eye to instinctively follow the moving scan, leading to increased eye movement and motion artifacts. In contrast, the 1060 nm wavelength either produces no visible line or a faint green line (due to two-photon absorption), minimizing this issue and reducing eye movement during scanning.

The second challenge lies in the choice of photodetectors. At 1060 nm, InGaAs photodetectors are employed, offering significantly higher responsivity, 0.72 A/W, compared to silicon photodetectors used at 850 nm. While some silicon detectors with responsivity as high as 0.5 A/W are available, they often come with a considerable tradeoff: a significantly reduced electrical bandwidth, 200 MHz, or low transimpedance gain, 700 V/A. This creates a balance between achieving higher responsivity and maintaining sufficient bandwidth for optimal imaging performance. This reduced responsivity limits the sensitivity of systems at 850 nm by almost 3. Also, the maximum permissible power for a static beam is higher at 1060 nm, allowing up to ~1.6 mW, compared to only 0.720 mW at 850 nm.

Figure 74 shows retinal OCT images acquired with two FDML lasers sweeping around 1060 nm. The first study by Kolb et al. [9] presents wide-field OCT images acquired at 1.68 MHz with an axial resolution of 14 µm in air. It also includes images acquired at 0.84 MHz for a 100° FOV, though these results are not shown here. The second study, presented by Klein et al. [8], demonstrates retinal OCT images with the same axial resolution and same sensitivity, ~90 dB, but at an axial scan rate of 3.35 MHz. Both articles feature *en-face* projections illustrating the FOV: 85° in the first case and 44° in the second. The first study shows images averaged over six frames, while the second provides single B-frames. This comparison highlights the level of detail visible in both cases, averaged or not.

In both articles, megahertz repetition rate lasers are used to enable fast scanning without under sampling. Achieving a high sampling point is critical to not miss feature in the sample. Scanning more slowly would increase sampling; however it would make the process more sensitive to patient motion, which is undesirable.

Kolb et al. Ultra-widefield retinal MHz-OCT imaging with up to 100 degrees viewing angle (2015).

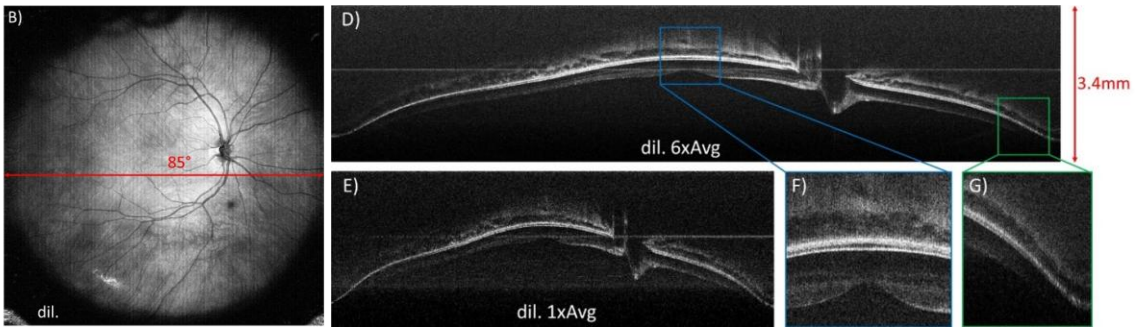

Klein et al. Multi-MHz retinal OCT (2013).

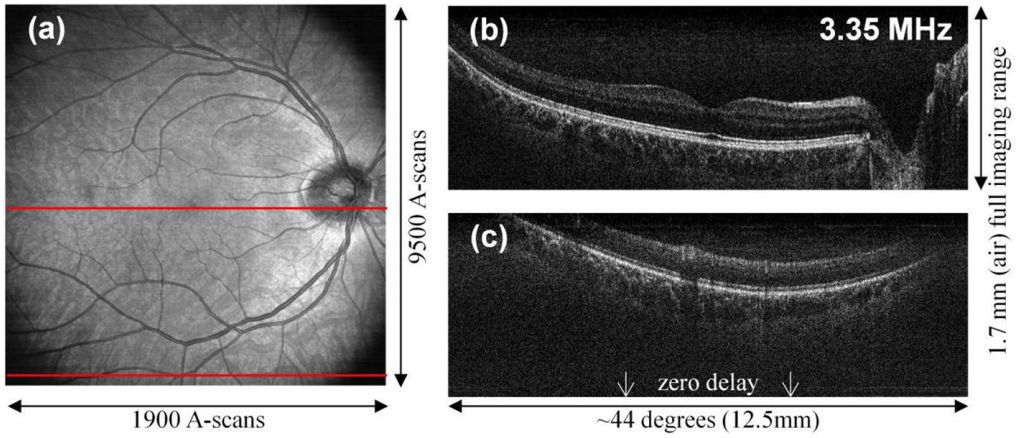

Figure 74. Retinal OCT imaging at 1060 nm, as presented in two articles. The top images, sources from [9], display an en-face projection of the retina with an 85° field of view. Next to it, the panel features a B-Scan averaged six times accompanied by two subfigures providing detailed zoomed-in views. Additionally, E) shows a single, non-averaged frame corresponding to D). The bottom images are extracted from [8]. They display a field of view of 44°. An en-face projection is given on the left with two red horizontal bars indicating the position of the single B-Scan (b) and (c).

Regarding tissue imaging, biological tissues scatter less at longer wavelengths, allowing for deeper penetration at 1060 nm compared to 850 nm. This is clearly demonstrated in Figure 74, where many features of the choroid beneath the retina are visible. In contrast, at 850 nm, it is

difficult to observe structures below the RPE unless higher power is used. However, we still observe some on the left side of Figure 73 (A).

At 850 nm, a smaller lateral resolution can be achieved due to the optical properties at this wavelength, offering certain advantages for imaging fine structures. Furthermore, the axial resolution at 850 nm can be extended below 10 µm since it is not constrained by water absorption, as demonstrated in the higher axial resolution images from Kent compared to those obtained with the 1060 nm laser presented here. In terms of speed, the 850 nm system can achieve comparable performance to the first article by Kolb et al. and may even approach rates of 3.35 MHz in the near future. However, at this current stage, the laser suffers from poor axial resolution, limiting its performance. Despite these potential advantages, imaging at 850 nm provides significantly lower contrast in the choroid compared to 1060 nm, as previously discussed, which diminishes its overall utility for deeper tissue visualization. Besides, the performance of these systems depends on the development of components such as balanced photodetectors. Therefore, it is challenging to bring the 850 nm system up to the same level of performance as the 1060 nm system without access to comparable components.

4.4. Summary and outlook

Retinal imaging has been successfully performed using the newly developed 850 nm FDML laser. For the first time, retinal images were acquired at 850 nm using swept-source flying spot technology, with a scanning speed surpassing 50 kHz. Furthermore, we significantly advanced this capability, achieving an unprecedented imaging rate of **1.7 MHz** – more than 30 times faster. This remarkable increase in speed provides an undeniable advantage in reducing the impact of microsaccades and patient motion during imaging, opening up potential applications in phase-sensitive imaging.

Images acquired at the University of Kent demonstrate an axial resolution of **9.89 µm** in water, enabling clear **distinction of individual layers within the RPE**. These images exhibit high axial resolution with a **sensitivity of 84.6 dB**, providing sufficient contrast to distinguish most retinal layers. While most images were captured at a sweep repetition rate of 414 kHz, imaging at 828 kHz was also achieved by utilizing both the forward and backward sweeps of the laser. To ensure high-quality imaging in this bidirectional mode, each sweep required calibration with specific masks – forward sweeps with forward masks and backward sweeps with backward masks. This approach successfully maintained axial resolution, as no degradation in image quality was observed.

While the laser at the University of Kent demonstrated good axial resolution, its capability for a faster repetition rate was showcased at the University of Lübeck, reaching 1.7 MHz. This speed was achieved through the implementation of optical buffering, allowing the main sweep to be copied four times. The high repetition rate enables the acquisition of a wider field of view without

compromising sampling density. The imaging software developed at the University of Lübeck also offers a **live preview** of the volume during acquisition, providing a highly convenient tool for real-time sample analysis.

Despite the laser's 30 nm output spectrum centered around 850 nm at the university of Lübeck, which theoretically provides an axial resolution of 15 µm in air, the measured resolution using the acquisition software is approximately 29 µm. This discrepancy arises because the spectrum does not fully reside within the -3 dB region, which defines the theoretical model. A flatter spectrum or one entirely within this region would yield results much closer to theory. However, achieving this is challenging due to the shape of the ASE of the SOA used in the laser. Moreover, the slight worsening of axial resolution with depth, which does not occur in the Kent system, suggests that the calibration method affects the axial resolution. The use of CMS calibration proved advantageous, achieving measured axial resolutions closer to the theoretical limit and remains constant over depth, compared to single-*k*-calibration. **CMS demonstrated superior performance** for this laser system, optimizing its imaging potential.

Both university systems exhibit shot noise behavior and achieve comparable lateral resolution. Their sensitivity is also similar, despite differences in optical power at the cornea. The study on the EVA eye showed that increasing the power from 0.720 mW to 1.2 mW significantly enhances imaging performance. Notably, the 0.720 mW power limit is calculated for a static beam; if calculated for a scanning beam, as is standard in commercial systems, imaging quality would improve substantially. Sensitivity levels could approach those of 1060 nm FDML lasers, reaching approximately 90 dB. This distinction is crucial when comparing imaging from medical devices and research setups, as **safety constraints** in research devices often result in lower contrast images. Additionally, faster lasers permit quicker scanning, allowing for higher permissible power levels to be applied to the sample.

While imaging performance at 850 nm does not yet match the capabilities of 1060 nm systems, there is significant potential for improvement. Achieving the full promise of this wavelength will require advancements in key components, such as developing SOAs with higher gain and optimized silicon detectors. Implementing new filters in the laser to enhance the laser performance and support a broader bandwidth. These enhancements could enable both better sensitivity and wider bandwidth, which are crucial for high-quality imaging.

This study demonstrates that 850 nm systems can achieve fast imaging speeds while maintaining good axial resolution, a critical step towards bridging the gap with 1060 nm systems. One limitation at 850 nm lies in penetration depth, as tissues scatter less at longer wavelengths, giving 1060 nm an inherent advantage in visualizing deeper structures. However, the ability to combine fast imaging with improved axial resolution at 850 nm indicates that comparable performance

could be achieved with further development. Moreover, there is substantial room to increase imaging power safely as mentioned above.

By addressing these limitations and optimizing power usage, 850 nm imaging could rival the performance of 1060 nm systems in many applications, providing fast, high-resolution imaging while maintaining safety standards.

GENERAL DISCUSSION AND FUTURE PERSPECTIVES

In this work, a novel 850 nm swept-source was developed, achieving remarkable advancements compared to existing systems operating at the same wavelength. This marks the first-ever Fourier domain mode-locked laser at 850 nm. Despite the technical challenges associated with this wavelength, the laser achieved an exceptional sweep rate of 1.7 MHz – 30 times faster than previously reported 850 nm sources used for retinal imaging. The innovative design specifically tailored for this system enabled an axial resolution of approximately 10 µm. Additionally, the laser demonstrated a long coherence length, supporting an OCT imaging depth of 15 mm, which enables retinal imaging. The laser also showed high phase stability through 1,000 consecutive forward sweeps which shows potential for phase-resolved techniques such as OCT angiography. A further advantage of this laser is its ease of transport, as it successfully enabled OCT imaging in two different countries.

The laser's performance was validated through *in-vivo* retinal imaging, which successfully visualized most retinal cellular layers. Two calibration methods were tested and proved compatible with the laser, highlighting their adaptability to its unique characteristics. The quality of the resulting images depended on several factors including the laser itself, its sweep repetition rate, the chosen calibration method, and the applied power on sample. The resolution achieved with the CMS calibration technique allowed the clear distinction of the three layers of the RPE, while the high speed facilitated wide *en-face* views of the optic nerve and macula with sufficient oversampling and live volume preview with the single-*k*-calibration. However, information from the choroid was consistently absent due to high scattering in the upper retinal layers, a limitation that highlights the inherent trade-offs of using 850 nm compared to 1060 nm, which provides better choroidal imaging.

Despite this limitation, commercial SD-OCT systems frequently utilize 850 nm light for imaging, demonstrating its feasibility to also image the choroid. Enhanced penetration and contrast could be achieved by increasing the laser's power, provided adequate safety mechanisms are implemented. Additional engineering improvements would further unlock the laser's potential. For instance, more robust temperature control is required to ensure long-term stability, and polarization controllers should be automated and integrated into the system for optimal performance. A frequency-control mechanism would also help stabilize operation over extended periods by regulating the frequency of the laser to remain at sweet spot. Despite engineering improvement, addressing chromatic dispersion presents another opportunity for refinement, however it is more challenging. The introduction of a new customized cFBG, or chirped mirror compensating for the remaining dispersion would enhance the laser's performance. However, this would introduce additional losses and PMD due to the potential addition of one more circulator. Testing circulators

with a blocked light axis might mitigate ripples but would increase the losses necessitate a higher-gain SOA or the reintroduction of dual-amplification with current modulation. Combining these innovations, dual-amplification, one axis circulator and better chromatic dispersion compensation could extend the laser's roll-off beyond 17 mm, enabling full eye imaging. The latter might be limited by the balanced photodetector's low electrical bandwidth. In addition, incorporating a newly developed FFP-TF with enhanced performance – such as reduced loss and greater tolerant to high amplitudes – would enable a wider bandwidth, resulting in improved axial resolution, or support higher sweep speeds, potentially reaching 3.4 MHz.

Finally, the laser's unique capabilities open the door to exploring novel imaging modalities within OCT. Its high sweep repetition rate, phase stability, and rapid volumetric acquisition make it suitable for dynamic OCT on small volumes. Additionally, its 850 nm wavelength lends itself to optical coherence microscopy, potentially offering improved transverse resolution. Coherent averaging could also enhance the quality of acquired B-Scans. Together, these possibilities highlight the broader potential of the laser in addressing various OCT research frontiers and advancing the field with its unique combination of speed, stability, and resolution.

PUBLICATIONS

Conference proceedings

[1] **Klufts, M.**, Lotz, S., Bashir, M., Karpf, S. and Huber, R., "Ultra-high-accuracy chromatic dispersion measurement in optical fibers," in *Proc.SPIE*(2022), p. 119970L.

[2] **Klufts, M.**, Lotz, S., Bashir, M. A., Pfeiffer, T., Mlynek, A., Wieser, W., Chamorovskiy, A., Shidlovski, V. and Huber, R., "850 nm FDML: performance and challenges," in *Proc.SPIE*(2023), p. 1236705.

[3] Bashir, M., Lotz, S., **Klufts, M.**, Krestnikov, I., Jirauschek, C. and Huber, R., *1190 nm Fourier domain mode locked (FDML) laser for optical coherence tomography (OCT)* (SPIE, 2023).

[4] **Klufts, M.**, Lotz, S., Bashir, M. A., Pfeiffer, T., Mlynek, A., Wieser, W., Chamorovskiy, A., Shidlovski, V., Podoleanu, A. and Huber, R., "Dual Amplification 850 nm FDML Laser," in *2023 Conference on Lasers and Electro-Optics Europe & European Quantum Electronics Conference (CLEO/Europe-EQEC)*(2023), pp. 1-1.

[5] Bashir, M. A., Lotz, S., **Klufts, M.**, Jirauschek, C. and Huber, R., "1190 nm FDML laser: Challenges and Strategies," in *Conference on Lasers and Electro-Optics/Europe (CLEO/Europe 2023) and European Quantum Electronics Conference (EQEC 2023)*(Optica Publishing Group, Munich, 2023), p. cl_8_3.

Peer-reviewed articles

[1] **Klufts, M.**, Jiménez, A. M., Lotz, S., Bashir, M. A., Pfeiffer, T., Mlynek, A., Wieser, W., Chamorovskiy, A., Bradu, A., Podoleanu, A. and Huber, R., "828 kHz retinal imaging with an 840 nm Fourier domain mode locked laser," Biomed Opt Express **14**, 6493-6508 (2023).

[2] Riha, R., Jimenez, A. M., Venugopal, G., **Klufts, M.**, Huber, R. and Podoleanu, A., "Dispersion-Tuned Mode-Locked Laser for Swept Source OCT at 850 nm Using a cFBG and the Pulse Modulation Technique," IEEE Photonics Journal **16**, 1-5 (2024).

REFERENCES

1. G. Karunamuni, S. Gu, M. Ford, L. Peterson, P. Ma, Y. Wang, A. Rollins, M. Jenkins, and M. Watanabe, "Capturing structure and function in an embryonic heart with Biophotonic tools," Frontiers in physiology **5**, 351 (2014).
2. A. Thampi, "Optical coherence tomography and machine learning applied to biological samples," (University of Auckland, 2022).
3. R. Huber, M. Wojtkowski, and J. G. Fujimoto, "Fourier Domain Mode Locking (FDML): A new laser operating regime and applications for optical coherence tomography," Optics Express **14**, 3225-3237 (2006).
4. J. P. Kolb, T. Pfeiffer, M. Eibl, H. Hakert, and R. Huber, "High-resolution retinal swept source optical coherence tomography with an ultra-wideband Fourier-domain mode-locked laser at MHz A-scan rates," Biomedical Optics Express **9**, 120-130 (2018).
5. C. Grill, T. Blömker, M. Schmidt, D. Kastner, T. Pfeiffer, J. P. Kolb, W. Draxinger, S. Karpf, C. Jirauschek, and R. Huber, "Towards phase-stabilized Fourier domain mode-locked frequency combs," Communications Physics **5**, 212 (2022).
6. T. Klein, R. André, W. Wieser, T. Pfeiffer, and R. Huber, "Joint aperture detection for speckle reduction and increased collection efficiency in ophthalmic MHz OCT," Biomedical Optics Express **4**, 619-634 (2013).
7. T. Klein, W. Wieser, C. M. Eigenwillig, B. R. Biedermann, and R. Huber, "Megahertz OCT for ultrawide-field retinal imaging with a 1050nm Fourier domain mode-locked laser," Optics Express **19**, 3044-3062 (2011).
8. T. Klein, W. Wieser, L. Reznicek, A. Neubauer, A. Kampik, and R. Huber, "Multi-MHz retinal OCT," Biomedical Optics Express **4**, 1890-1908 (2013).
9. J. P. Kolb, T. Klein, C. L. Kufner, W. Wieser, A. S. Neubauer, and R. Huber, "Ultra-widefield retinal MHz-OCT imaging with up to 100 degrees viewing angle," Biomedical Optics Express **6**, 1534-1552 (2015).
10. M. Göb, S. Lotz, L. Ha-Wissel, S. Burhan, S. Böttger, F. Ernst, J. Hundt, and R. Huber, "Large area robotically assisted optical coherence tomography (LARA-OCT) for skin imaging with MHz-OCT surface tracking," in *Proc.SPIE*(2023), p. 123670C.
11. S. Karpf, M. Eibl, W. Wieser, T. Klein, and R. Huber, "FDML Raman: High Speed, High Resolution Stimulated Raman Spectroscopy with Rapidly Wavelength Swept Lasers," in *CLEO* (Optica Publishing Group, San Jose, California, 2013).
12. S. Karpf, M. Eibl, W. Wieser, T. Klein, and R. Huber, "A Time-Encoded Technique for fibre-based hyperspectral broadband stimulated Raman microscopy," Nature communications **6**, 6784 (2015).
13. B. Schulte, M. Göb, A. P. Singh, S. Lotz, W. Draxinger, M. Heimke, M. Pieper, T. Heinze, T. Wedel, M. Rahlves, R. Huber, and M. Ellrichmann, "High-resolution rectoscopy using MHz optical coherence tomography: a step towards real time 3D endoscopy," Sci Rep **14**, 4672 (2024).
14. W. W. Tianshi Wang, Geert Springeling, Robert Beurskens, Charles T. Lancee, Tom Pfeiffer, Antonius F. W. van der Steen, Robert Huber, and Gijs van Soest, "Intravascular optical coherence tomography imaging at 3200 frames per second," Optics letters **38**, 1715 (2013).
15. D. C. Adler, W. Wieser, F. Trepanier, J. M. Schmitt, and R. A. Huber, "Extended coherence length Fourier domain mode locked lasers at 1310 nm," Optics Express **19**, 20930-20939 (2011).
16. T. Wang, T. Pfeiffer, E. Regar, W. Wieser, H. van Beusekom, C. T. Lancee, G. Springeling, I. Krabbendam, A. F. W. van der Steen, R. Huber, and G. van Soest, "Heartbeat OCT: in vivo intravascular megahertz-optical coherence tomography," Biomedical Optics Express **6**, 5021-5032 (2015).
17. S. Burhan, N. Detrez, K. Rewerts, M. Göb, C. Hagel, M. M. Bonsanto, D. Theisen-Kunde, R. Huber, and R. Brinkmann, "Characterization of brain tumor tissue by time-resolved, phase-sensitive optical coherence elastography at 3.2 MHz line rate," in *Proc.SPIE*(2023), p. 123680F.
18. S. Burhan, N. Detrez, K. Rewerts, P. Strenge, S. Buschschlüter, J. Kren, C. Hagel, M. M. Bonsanto, R. Brinkmann, and R. Huber, "Phase unwrapping for MHz optical coherence elastography and application to brain tumor tissue," Biomedical Optics Express **15**, 1038-1058 (2024).
19. M. A. Bashir, S. Lotz, M. Klufts, C. Jirauschek, and R. Huber, "1190 nm FDML laser: Challenges and Strategies," in *2023 Conference on Lasers and Electro-Optics Europe & European Quantum Electronics Conference (CLEO/Europe-EQEC)*(2023), pp. 1-1.
20. E. A. Swanson, and J. G. Fujimoto, "The ecosystem that powered the translation of OCT from fundamental research to clinical and commercial impact [Invited]," Biomed Opt Express **8**, 1638-1664 (2017).

21. D. Huang, E. A. Swanson, C. P. Lin, J. S. Schuman, W. G. Stinson, W. Chang, M. R. Hee, T. Flotte, K. Gregory, C. A. Puliafito, and J. G. Fujimoto, "Optical Coherence Tomography," Science **254**, 1178-1181 (1991).
22. B. Potsaid, I. Gorczynska, V. J. Srinivasan, Y. Chen, J. Jiang, A. Cable, and J. G. Fujimoto, "Ultrahigh speed Spectral / Fourier domain OCT ophthalmic imaging at 70,000 to 312,500 axial scans per second," Optics Express **16**, 15149-15169 (2008).
23. L. An, P. Li, T. T. Shen, and R. Wang, "High speed spectral domain optical coherence tomography for retinal imaging at 500,000 A-lines per second," Biomedical Optics Express **2**, 2770-2783 (2011).
24. Y. Chen, D. L. Burnes, M. de Bruin, M. Mujat, and J. F. de Boer, "Three-dimensional pointwise comparison of human retinal optical property at 845 and 1060 nm using optical frequency domain imaging," J Biomed Opt **14**, 024016 (2009).
25. S.-W. Lee, H.-W. Song, B.-K. Kim, M.-Y. Jung, S.-H. Kim, J.-D. Cho, and C.-S. Kim, "Fourier Domain Optical Coherence Tomography for Retinal Imaging with 800-nm Swept Source: Real-time Resampling in k-domain," J. Opt. Soc. Korea **15**, 293-299 (2011).
26. V. J. Srinivasan, R. Huber, I. Gorczynska, J. G. Fujimoto, J. Y. Jiang, P. Reisen, and A. E. Cable, "High-speed, high-resolution optical coherence tomography retinal imaging with a frequency-swept laser at 850 nm," Optics Letters **32**, 361-363 (2007).
27. M. Kendrisic, V. Agafonov, M. Salas, L. Ferrara, M. Niederleithner, H. Resch, S. Steiner, C. Vass, W. Drexler, and R. A. Leitgeb, "Thermally tuned VCSEL at 850 nm as a low-cost alternative source for full-eye SS-OCT," Optics Letters **48**, 3079-3082 (2023).
28. S. Marschall, C. Pedersen, and P. E. Andersen, "Investigation of the impact of water absorption on retinal OCT imaging in the 1060 nm range," Biomedical Optics Express **3**, 1620-1631 (2012).
29. L. Reznicek, J. P. Kolb, T. Klein, K. J. Mohler, W. Wieser, R. Huber, M. Kernt, J. Märtz, and A. S. Neubauer, "Wide-Field Megahertz OCT Imaging of Patients with Diabetic Retinopathy," Journal of Diabetes Research **2015**, 305084 (2015).
30. P. Boris, M. H. Boris, U. Angelika, H. Bernd, S. Harald, Z. Florian, E. M. James, F.-R. Christiane, M. D. Carl Glittenberg, M. D. Susanne Binder, and D. Wolfgang, "Three-dimensional optical coherence tomography at 1050 nm versus 800 nm in retinal pathologies: enhanced performance and choroidal penetration in cataract patients," Journal of Biomedical Optics **12**, 041211 (2007).
31. M. Klufts, A. M. Jiménez, S. Lotz, M. A. Bashir, T. Pfeiffer, A. Mlynek, W. Wieser, A. Chamorovskiy, A. Bradu, A. Podoleanu, and R. Huber, "828 kHz retinal imaging with an 840 nm Fourier domain mode locked laser," Biomed Opt Express **14**, 6493-6508 (2023).
32. M. Münter, M. Pieper, T. Kohlfaerber, E. Bodenstorfer, M. Ahrens, C. Winter, R. Huber, P. König, G. Hüttmann, and H. Schulz-Hildebrandt, "Microscopic optical coherence tomography (mOCT) at 600 kHz for 4D volumetric imaging and dynamic contrast," Biomed Opt Express **12**, 6024-6039 (2021).
33. D. Valente, K. V. Vienola, R. J. Zawadzki, and R. S. Jonnal, "Kilohertz retinal FF-SS-OCT and flood imaging with hardware-based adaptive optics," Biomedical Optics Express **11**, 5995-6011 (2020).
34. D. Hillmann, H. Spahr, C. Pfäffle, H. Sudkamp, G. Franke, and G. Hüttmann, "In vivo optical imaging of physiological responses to photostimulation in human photoreceptors," Proceedings of the National Academy of Sciences **113**, 13138-13143 (2016).
35. R. Huber, "Sources and swept source OCT," (NETLAS winter school, 2022).
36. R. Huber, M. Wojtkowski, K. Taira, J. G. Fujimoto, and K. Hsu, "Amplified, frequency swept lasers for frequency domain reflectometry and OCT imaging: design and scaling principles," Optics Express **13**, 3513-3528 (2005).
37. T. Klein, and R. Huber, "High-speed OCT light sources and systems [Invited]," Biomedical Optics Express **8**, 828-859 (2017).
38. S. Rivet, M. Maria, A. Bradu, T. Feuchter, L. Leick, and A. Podoleanu, "Complex master slave interferometry," Optics Express **24**, 2885-2904 (2016).
39. A. Bradu, N. M. Israelsen, M. Maria, M. J. Marques, S. Rivet, T. Feuchter, O. Bang, and A. Podoleanu, "Recovering distance information in spectral domain interferometry," Scientific Reports **8**, 15445 (2018).
40. J. P. Fingler, "Motion contrast using optical coherence tomography," (California institute of technology, 2007).
41. S. Aumann, S. Donner, J. Fischer, and F. Müller, "Optical Coherence Tomography (OCT): Principle and Technical Realization," in *High Resolution Imaging in Microscopy and Ophthalmology: New Frontiers in Biomedical Optics*, *J. F. Bille,* (Springer International Publishing, 2019), pp. 59-85.
42. J. P. Kolb, "Verbesserung und Anwendung der ultraschnellen optischen Kohärenztomographie am menschlichen Auge," (Universität zu Lübeck, 2017).

43. B. Hermann, E. J. Fernández, A. Unterhuber, H. Sattmann, A. F. Fercher, W. Drexler, P. M. Prieto, and P. Artal, "Adaptive-optics ultrahigh-resolution optical coherence tomography," Optics Letters **29**, 2142-2144 (2004).
44. R. J. Zawadzki, S. M. Jones, S. S. Olivier, M. Zhao, B. A. Bower, J. A. Izatt, S. Choi, S. Laut, and J. S. Werner, "Adaptive-optics optical coherence tomography for high-resolution and high-speed 3D retinal in vivo imaging," Optics Express **13**, 8532-8546 (2005).
45. J. F. de Boer, B. Cense, B. H. Park, M. C. Pierce, G. J. Tearney, and B. E. Bouma, "Improved signal-to-noise ratio in spectral-domain compared with time-domain optical coherence tomography," Optics Letters **28**, 2067-2069 (2003).
46. T. Pfeiffer, M. Petermann, W. Draxinger, C. Jirauschek, and R. Huber, "Ultra low noise Fourier domain mode locked laser for high quality megahertz optical coherence tomography," Biomedical Optics Express **9**, 4130-4148 (2018).
47. R. Leitgeb, C. K. Hitzenberger, and A. F. Fercher, "Performance of fourier domain vs. time domain optical coherence tomography," Optics Express **11**, 889-894 (2003).
48. G. Ebers, "The Eders Papyrus ", O. U. Press, ed. (1875).
49. F. Retief, A. Stulting, and L. Cilliers, "The eye in antiquity," South African medical journal = Suid-Afrikaanse tydskrif vir geneeskunde **98**, 697-700 (2008).
50. G. Sadovsky, Overnight Glasses, "Eyewear Industry Statistics and Facts," https://www.overnightglasses.com/eyewear-industry-statistics/, (2024).
51. I. Bhutto, and G. Lutty, "Understanding age-related macular degeneration (AMD): Relationships between the photoreceptor/retinal pigment epithelium/Bruch's membrane/choriocapillaris complex," Molecular Aspects of Medicine **33**, 295-317 (2012).
52. H. Kolb, The Organization of the Retina and Visual System, "Simple Anatomy of the Retina," https://webvision.med.utah.edu/book/part-i-foundations/simple-anatomy-of-the-retina/, (2011).
53. N. D. Wangsa-Wirawan, and R. A. Linsenmeier, "Retinal Oxygen: Fundamental and Clinical Aspects," Archives of Ophthalmology **121**, 547-557 (2003).
54. D. Majumder, "Anatomy of Retina," https://www.eophtha.com/posts/anatomy-of-retina, (2021).
55. Wikipedia, The free Encyclopedia, "Fundus (eye)," (2024).
56. H. Friedenwald, "The history of the invention and of the development of the ophthalmoscope," Journal of the American Medical Association **XXXVIII**, 549-552 (1902).
57. A. F. Fercher, K. Mengedoht, and W. Werner, "Eye-length measurement by interferometry with partially coherent light," Optics Letters **13**, 186-188 (1988).
58. E. A. Swanson, J. A. Izatt, C. P. Lin, J. G. Fujimoto, J. S. Schuman, M. R. Hee, D. Huang, and C. A. Puliafito, "In vivo retinal imaging by optical coherence tomography," Optics Letters **18**, 1864-1866 (1993).
59. W. Drexler, and J. G. Fujimoto, "*Optical Coherence Tomography,*" (Springer Cham, 2015).
60. M. Wojtkowski, R. Leitgeb, A. Kowalczyk, T. Bajraszewski, and A. Fercher, "In vivo human retinal imaging by Fourier domain optical coherence tomography," Journal of Biomedical Optics **7** (2002).
61. L. Schmetterer, and D. Gherghel, "Editorial: Vascular involvement in eye diseases," Frontiers in medicine **10**, 1301145 (2023).
62. M. Niederleithner, L. Sisternes, H. Stino, A. Sedova, T. Schlegl, H. Bagherinia, A. Britten, P. Matten, U. Schmidt-Erfurth, A. Pollreisz, W. Drexler, R. Leitgeb, and T. Schmoll, "Ultra-widefield OCT Angiography," IEEE Transactions on Medical Imaging **PP**, 1-1 (2022).
63. F. Schwarzhans, S. Desissaire, S. Steiner, M. Pircher, C. K. Hitzenberger, H. Resch, C. Vass, and G. Fischer, "Automatic retinal nerve fiber bundle tracing based on large field of view polarization sensitive OCT data," Biomedical Optics Express **13**, 65-81 (2022).
64. University of Vienna, "Development of advanced OCT technologies for biomedical imaging," https://mpbmt.meduniwien.ac.at/en/research/biophotonics/oct-technologies/,
65. A. Baghaie, Z. Yu, and R. M. D'Souza, "Involuntary eye motion correction in retinal optical coherence tomography: Hardware or software solution?," Medical Image Analysis **37**, 129-145 (2017).
66. Ento Key, "Introduction to OCT," https://entokey.com/introduction-to-oct/, (2017).
67. A. Einstein, "Über einen die Erzeugung und Verwandlung des Lichtes betreffenden heuristischen Gesichtspunkt," Annalen der Physik **322**, 132-148 (1905).
68. FiberLabs Inc., "Spontaneous and stimulated emission," https://www.fiberlabs.com/glossary/spontaneous-and-stimulated-emission/, (2021).
69. A. Einstein, "Zur Quantentheorie der Strahlung," Physikalische Zeitschrift 18 (1917).
70. H. J. Eichler, J. Eichler, and O. Lux, "Lasers," Springer Cham (2018).
71. M. Göb, T. Pfeiffer, W. Draxinger, S. Lotz, J. P. Kolb, and R. Huber, "Continuous spectral zooming for in vivo live 4D-OCT with MHz A-scan rates and long coherence," Biomedical Optics Express **13**, 713-727 (2022).

72. H. Goldstein, "*Classical Mechanics,"* (Addison-Wesley, 2002).
73. ANSI, "American National Standard for Safe Use of Laser (ANSI 136.1)," in *In: ANSI 136.1–2000*(2000).
74. IEC60825-1, "Safety of laser products - Part 1 : Equipment classification and requirements," (2014).
75. R. Paschotta, RP Photonics Encyclopedia, "Coherence," https://www.rp-photonics.com/coherence.html,
76. P. Microscope, "Photology 4: Coherence," (Youtube, 2024).
77. H. K. Sahoo, T. Ansbæk, L. Ottaviano, E. Semenova, F. Zubov, O. Hansen, and K. Yvind, "Tunable MEMS VCSEL on Silicon Substrate," IEEE Journal of Selected Topics in Quantum Electronics **25**, 1-7 (2019).
78. V. Jayaraman, D. John, C. Burgner, M. Robertson, B. Potsaid, J. Jiang, T. Tsai, W. Choi, C. Lu, P. J. S. Heim, J. Fujimoto, and A. Cable, "Recent advances in MEMS-VCSELs for high performance structural and functional SS-OCT imaging," SPIE BiOS **8934** (2014).
79. K. Yvind, "Wide and fast tunable MEMS VCSELs," (2022).
80. I. Grulkowski, J. J. Liu, B. Potsaid, V. Jayaraman, C. D. Lu, J. Jiang, A. E. Cable, J. S. Duker, and J. G. Fujimoto, "Retinal, anterior segment and full eye imaging using ultrahigh speed swept source OCT with vertical-cavity surface emitting lasers," Biomedical Optics Express **3**, 2733-2751 (2012).
81. C. Jirauschek, and R. Huber, "Wavelength shifting of intra-cavity photons: Adiabatic wavelength tuning in rapidly wavelength-swept lasers," Biomedical Optics Express **6**, 2448-2465 (2015).
82. M. E. Kuznetsov, F. Hakimi, R. Sprague, and A. Mooradian, "High-power (>0.5-W CW) diode-pumped vertical-external-cavity surface-emitting semiconductor lasers with circular TEM/sub 00/ beams," IEEE Photonics Technology Letters **9**, 1063-1065 (1997).
83. Y. Huo, C.-Y. Cho, K. Huang, Y.-F. Chen, and C. Lee, "Exploring the DBR superlattice effect on the thermal performance of a VECSEL with the finite element method," Optics Letters **44**, 327 (2019).
84. J. Piprek, T. Troger, B. Schroter, J. Kolodzey, and C. S. Ih, "Thermal conductivity reduction in GaAs-AlAs distributed Bragg reflectors," IEEE Photonics Technology Letters **10**, 81-83 (1998).
85. M. Kuznetsov, F. Hakimi, R. Sprague, and A. Mooradian, "Design and characteristics of high-power (>0.5-W CW) diode-pumped vertical-external-cavity surface-emitting semiconductor lasers with circular TEM/sub 00/ beams," IEEE Journal of Selected Topics in Quantum Electronics **5**, 561-573 (1999).
86. H. Kahle, C. M. N. Mateo, U. Brauch, P. Tatar-Mathes, R. Bek, M. Jetter, T. Graf, and P. Michler, "Semiconductor membrane external-cavity surface-emitting laser (MECSEL)," Optica **3**, 1506-1512 (2016).
87. H. Kahle, H.-M. Phung, J.-P. Penttinen, P. Rajala, A. Tukiainen, S. Ranta, and M. Guina, "Double-side pumped membrane external-cavity surface-emitting laser (MECSEL) with increased efficiency emitting > 3 W in the 780 nm region," in *Conference on Lasers and Electro-Optics*(Optica Publishing Group, San Jose, California, 2019).
88. A. Broda, B. Jezewski, M. Szymański, and J. Muszalski, "High-Power 1770 nm Emission of a Membrane External-Cavity Surface-Emitting Laser," IEEE Journal of Quantum Electronics **57**, 1-6 (2021).
89. H. Kahle, "(Novel) broadband semiconductor gain devices: Semiconductor optical amplifiers (SOAs) and membrane external-cavity surface-emitting lasers," (NETLAS winter school, 2022).
90. E. F. Schubert, "*Physical Foundations of Solid-State Devices,"* (E. Fred Schubert, 2022).
91. Core Ray, "Semiconductor Optical Amplifiers (SOA)," https://www.coreray.kr/shop_view/?idx=253, (2025).
92. H. Lim, J. F. d. Boer, B. H. Park, E. C. W. Lee, R. Yelin, and S. H. Yun, "Optical frequency domain imaging with a rapidly swept laser in the 815–870 nm range," Optics Express **14**, 5937-5944 (2006).
93. M. Strupler, N. Goulamhoussen, E. D. Montigny, and C. Boudoux, "Rapidly Wavelength-Swept Laser at 780 nm," IEEE Photonics Technology Letters **23**, 197-199 (2011).
94. S. Grelet, A. M. Jiménez, R. D. Engelsholm, P. B. Montague, and A. Podoleanu, "40 MHz Swept-Source Optical Coherence Tomography at 1060 nm Using a Time-Stretch and Supercontinuum Spectral Broadening Dynamics," IEEE Photonics Journal **14**, 1-6 (2022).
95. S. Moon, and D. Y. Kim, "Ultra-high-speed optical coherence tomography with a stretched pulse supercontinuum source," Optics Express **14**, 11575-11584 (2006).
96. A. M. Jiménez, S. Grelet, P. B. Montague, A. Bradu, and A. Podoleanu, "Dual Ultrahigh Speed Swept-Source & Time Domain Optical Coherence Tomography system using a time stretch laser and a KTN deflector," in *Optical Coherence Imaging Techniques and Imaging in Scattering Media V*(Optica Publishing Group, Munich, 2023), p. 126320B.

97. D. Huang, F. Li, Z. He, Z. Cheng, C. Shang, and P. K. A. Wai, "400 MHz ultrafast optical coherence tomography," Optics Letters **45**, 6675 (2020).
98. S. Tozburun, M. Siddiqui, and B. J. Vakoc, "A rapid, dispersion-based wavelength-stepped and wavelength-swept laser for optical coherence tomography," Optics Express **22**, 3414-3424 (2014).
99. S. Tozburun, C. Blatter, M. Siddiqui, E. F. J. Meijer, and B. J. Vakoc, "Phase-stable Doppler OCT at 19 MHz using a stretched-pulse mode-locked laser," Biomedical Optics Express **9**, 952-961 (2018).
100. L. Wang, M. Wan, Z. Shen, X. Wang, Y. Cao, X. Feng, and B.-o. Guan, "Wavelength-swept fiber laser based on bidirectional used linear chirped fiber Bragg grating," Photon. Res. **5**, 219-223 (2017).
101. K. Tamura, and M. Nakazawa, "Dispersion-tuned harmonically mode-locked fiber ring laser for self-synchronization to an external clock," Optics Letters **21**, 1984-1986 (1996).
102. S. Yamashita, and Y. Takubo, "Fast wavelength-swept dispersion-tuned fiber laser over 500kHz using a wideband chirped fiber Bragg grating," 21st International Conference on Optical Fibre Sensors (OFS21) **7753** (2011).
103. Y. Takubo, and S. Yamashita, "High-speed dispersion-tuned wavelength-swept fiber laser using a reflective SOA and a chirped FBG," Optics Express **21**, 5130-5139 (2013).
104. J. Mei, X. Xiao, and C. Yang, "1 μm wavelength swept fiber laser based on dispersion-tuning technique," Chin. Opt. Lett. **13**, 091403 (2015).
105. LibreTexts, "*University physics I: mechanics, sound, oscillations, and waves (openStax).*"
106. R. Paschotta, RP Photonics Encyclopedia, "Passive mode locking," https://www.rp-photonics.com/passive_mode_locking.html,
107. S. Lotz, M. Göb, W. Draxinger, A. Dick, and R. Huber, "13.4 MHz FDML Laser for Intra-Surgical Optical Coherence Tomography," in *Conference on Lasers and Electro-Optics/Europe (CLEO/Europe 2023) and European Quantum Electronics Conference (EQEC 2023)*(Optica Publishing Group, Munich, 2023).
108. R. Huber, " FDML (incl. Parallelization)," in *Optical Coherence Tomography*, *W. Drexler, and J. G. Fujimoto,* (Springer Cham, 2015).
109. T. Kraetschmer, and S. T. Sanders, "Ultrastable Fourier Domain Mode Locking Observed in a Laser Sweeping 1363.8 – 1367.3 nm," in *Conference on Lasers and Electro-Optics/International Quantum Electronics Conference*(Optica Publishing Group, Baltimore, Maryland, 2009).
110. S. Slepneva, B. O'Shaughnessy, S. Hegarty, B. Kelleher, S. Rica, and G. Huyet, "Convective Nozaki-Bekki holes in a long cavity laser," SPIE LASE **9732** (2016).
111. C. Jirauschek, B. Biedermann, and R. Huber, "A theoretical description of Fourier domain mode locked lasers," Optics Express **17**, 24013-24019 (2009).
112. M. Schmidt, C. Grill, S. Lotz, T. Pfeiffer, R. Huber, and C. Jirauschek, "Intensity pattern types in broadband Fourier domain mode-locked (FDML) lasers operating beyond the ultra-stable regime," Applied Physics B **127**, 60 (2021).
113. S. Lotz, C. Grill, M. Göb, W. Draxinger, J. P. Kolb, and R. Huber, "Cavity length control for Fourier domain mode locked (FDML) lasers with μm precision," Biomed Opt Express **12**, 2604-2616 (2021).
114. S. Todor, B. Biedermann, R. Huber, and C. Jirauschek, "Balance of physical effects causing stationary operation of Fourier domain mode-locked lasers," J. Opt. Soc. Am. B **29**, 656-664 (2012).
115. A. Bilenca, S. H. Yun, G. J. Tearney, and B. E. Bouma, "Numerical study of wavelength-swept semiconductor ring lasers: the role of refractive-index nonlinearities in semiconductor optical amplifiers and implications for biomedical imaging applications," Optics Letters **31**, 760-762 (2006).
116. M. Y. Jeon, J. Zhang, and Z. Chen, "Characterization of Fourier domain mode-locked wavelength swept laser for optical coherence tomography imaging," Optics Express **16**, 3727-3737 (2008).
117. S. Todor, B. Biedermann, R. Huber, and C. Jirauschek, "Analysis of the Optical Dynamics in Fourier Domain Mode-Locked Lasers," in *Advanced Photonics & Renewable Energy*(Optica Publishing Group, Karlsruhe, 2010), p. SWC4.
118. S. Slepneva, B. Kelleher, B. O'Shaughnessy, S. P. Hegarty, A. G. Vladimirov, and G. Huyet, "Dynamics of Fourier domain mode-locked lasers," Optics Express **21**, 19240-19251 (2013).
119. S. Song, W. Wei, B.-Y. Hsieh, I. Pelivanov, T. T. Shen, M. O'Donnell, R. K. Wang, and R. K. Wang, "Strategies to improve phase-stability of ultrafast swept source optical coherence tomography for single shot imaging of transient mechanical waves at 16 kHz frame rate," Appl Phys Lett **108**, 191104 (2016).
120. T. Pfeiffer, M. Göb, W. Draxinger, S. Karpf, J. P. Kolb, and R. Huber, "Flexible A-scan rate MHz-OCT: efficient computational downscaling by coherent averaging," Biomedical Optics Express **11**, 6799-6811 (2020).

121. Wikipedia, the free Encyclopedia, "Fabry-Pérot interferometer," https://en.wikipedia.org/w/index.php?title=Fabry%E2%80%93P%C3%A9rot_interferometer&oldid=1217745546, (2024).
122. J. W. Hahn, S. N. Park, and C. Rhee, "Fabry-Perot wavemeter for shot-by-shot analysis of pulsed lasers," Applied optics **32**, 1095-1099 (1993).
123. Wikipédia, "Interféromètre de Fabry-Perot - Wikipédia, l'encyclopédie libre," http://fr.wikipedia.org/w/index.php?title=Interf%C3%A9rom%C3%A8tre_de_Fabry-Perot&oldid=218146043, (2024).
124. Thorlabs Inc. , "Fabry-Perot Interferometer Tutorial," https://www.thorlabs.com/newgrouppage9.cfm?objectgroup_id=9021,
125. LightMachinery, "Etalons," https://lightmachinery.com/optics/custom-optics/etalons/?utm_source=RP_Photonics&utm_medium=referral&utm_campaign=advertising_package,
126. H. Robert, W. Wolfgang, K. Thomas, E. Christoph, B. Benjamin, M. Dieter, and E. Michael, "Danymical Fabry-Pérot tuneable filter device," L.-M.-U. München, US8855149B2, (2014).
127. M. Klufts, S. Lotz, M. Bashir, S. Karpf, and R. Huber, "Ultra-high-accuracy chromatic dispersion measurement in optical fibers," in *Proc.SPIE*(2022), p. 119970L.
128. R. Paschotta, RP Photonics AG, "Phase velocity," https://www.rp-photonics.com/phase_velocity.html,
129. Wikipedia, and contributors, "Group Velocity," https://en.wikipedia.org/wiki/Group_velocity, (2024).
130. R. Paschotta, The RP Photonics Encyclopedia, "Chromatic dispersion," https://www.rp-photonics.com/chromatic_dispersion.html,
131. G. Chauvel, Anritsu, "Dispersion in Optical Fibers," (2008).
132. I. S. Amiri, and M. Ghasemi, "Study of Optical Fibre Dispersion and Measuring Methods," in *Design and Development of Optical Dispersion Characterization Systems*, *I. S. Amiri, and M. Ghasemi,* (Springer International Publishing, 2019), pp. 11-24.
133. J. Y. Lee, and D. Y. Kim, "Versatile chromatic dispersion measurement of a single mode fiber using spectral white light interferometry," Optics Express **14**, 11608-11615 (2006).
134. W. Qi, X. Huang, D. Ho, S. Yoo, K. T. Yong, and F. Luan, "Dispersion measurement of optical fibers by phase retrieval from spectral interferometry," Journal of Optics **19**, 055611 (2017).
135. M. Tateda, N. Shibata, and S. Seikai, "Interferometric method for chromatic dispersion measurement in a single-mode optical fiber," IEEE Journal of Quantum Electronics **17**, 404-407 (1981).
136. J. Hult, R. S. Watt, and C. F. Kaminski, "Dispersion Measurement in Optical Fibers Using Supercontinuum Pulses," J. Lightwave Technol. **25**, 820-824 (2007).
137. L. G. Cohen, and C. Lin, "Pulse delay measurements in the zero material dispersion wavelength region for optical fibers," Applied optics **16**, 3136-3139 (1977).
138. A. Sugimura, and K. Daikoku, "Wavelength dispersion of optical fibers directly measured by ”difference method” in the 0.8–1.6 μm range," Review of Scientific Instruments **50**, 343-346 (1979).
139. T. Ito, O. Slezak, M. Yoshita, H. Akiyama, and Y. Kobayashi, "High-precision group-delay dispersion measurements of optical fibers via fingerprint-spectral wavelength-to-time mapping," Photon. Res. **4**, 13-16 (2016).
140. W. Wieser, B. R. Biedermann, T. Klein, C. M. Eigenwillig, and R. Huber, "Ultra-rapid dispersion measurement in optical fibers," Optics Express **17**, 22871-22878 (2009).
141. F. Koch, S. V. Chernikov, and J. R. Taylor, "Dispersion measurement in optical fibres over the entire spectral range from 1.1 μm to 1.7 μm," Optics Communications **175**, 209-213 (2000).
142. Wikipedia, The Free Encyclopedia, "Polarization (waves)," https://en.wikipedia.org/wiki/Polarization_(waves),
143. Wikipedia, The Free Encyclopedia, "Polarization mode dispersion," https://en.wikipedia.org/wiki/Polarization_mode_dispersion, (2023).
144. R. Paschotta, RP Photonics Encyclopedia, "Polarization mode dispersion," https://www.rp-photonics.com/polarization_mode_dispersion.html,
145. F. Roy, C. Francia, F. Bruyere, and D. Penninckx, "A simple dynamic polarization mode dispersion compensator," in *OFC/IOOC . Technical Digest. Optical Fiber Communication Conference, 1999, and the International Conference on Integrated Optics and Optical Fiber Communication*(1999), pp. 275-278 vol.271.
146. Z. Pan, Y. Xie, S. Lee, A. E. Willner, V. Grubsky, D. S. Starodubov, and J. Feinberg, "Chirp-Free Tunable PMD Compensation using Hi-Bi Nonlinearly-Chirped FBGs in a Dual-Pass Configuration," in *Optical Fiber Communication Conference*(Optica Publishing Group, Baltimore, Maryland, 2000), p. ThH2.

147. H. Sunnerud, X. Chongjin, M. Karlsson, R. Samuelsson, and P. A. Andrekson, "A comparison between different PMD compensation techniques," J. Lightwave Technol. **20**, 368-378 (2002).
148. H. Bülow, and S. Lanne, "PMD compensation techniques," in *Polarization Mode Dispersion*, *A. Galtarossa, and C. R. Menyuk,* (Springer New York, 2005), pp. 225-245.
149. M. Akbulut, A. M. Weiner, and P. J. Miller, "Broadband All-Order Polarization Mode Dispersion Compensation Using Liquid-Crystal Modulator Arrays," J. Lightwave Technol. **24**, 251 (2006).
150. J. Zhang, J. Jing, P. Wang, and Z. Chen, "Polarization-maintaining buffered Fourier domain mode-locked swept source for optical coherence tomography," Optics Letters **36**, 4788-4790 (2011).
151. K. H. Cheng, B. A. Standish, V. X. Yang, K. K. Cheung, X. Gu, E. Y. Lam, and K. K. Wong, "Wavelength-swept spectral and pulse shaping utilizing hybrid Fourier domain modelocking by fiber optical parametric and erbium-doped fiber amplifiers," Opt Express **18**, 1909-1915 (2010).
152. M. Harduar, A. Mariampillai, B. Vuong, K. Cheng, L. Chen, X. Gu, B. Standish, and V. Yang, "Dual Core Ytterbium Doped Fiber Ring Laser in Fourier Domain Mode Locked Operation for Swept-Source Optical Coherence Tomography," Proc. SPIE **7580**, 86 (2010).
153. H. Y. C. Kyle, A. S. Beau, X. D. Y. Victor, K. K. Y. Cheung, G. Xijia, Y. L. Edmund, and K. K. Y. Wong, "Hybrid Fourier domain modelocked laser utilizing a fiber optical parametric amplifier and an erbium doped fiber amplifier," in *Proc.SPIE*(2010), p. 75802Q.
154. B. Vuong, M. Harduar, K. Cheng, X. Gu, L. Chen, B. Standish, and V. Yang, "Cascaded Raman Fiber Laser in Fourier Domain Mode Lock Operation," Proceedings of SPIE - The International Society for Optical Engineering **7580** (2010).
155. G. Y. Liu, A. Mariampillai, B. A. Standish, N. R. Munce, X. Gu, and I. A. Vitkin, "High power wavelength linearly swept mode locked fiber laser for OCT imaging," Optics Express **16**, 14095-14105 (2008).
156. M. K. K. Leung, A. Mariampillai, B. A. Standish, K. K. C. Lee, N. R. Munce, I. A. Vitkin, and V. X. D. Yang, "High-power wavelength-swept laser in Littman telescope-less polygon filter and dual-amplifier configuration for multichannel optical coherence tomography," Optics Letters **34**, 2814-2816 (2009).
157. M. Y. Jeon, J. Zhang, Q. Wang, and Z. Chen, "High-speed and wide bandwidth Fourier domain mode-locked wavelength swept laser with multiple SOAs," Optics Express **16**, 2547-2554 (2008).
158. M. Klufts, S. Lotz, M. A. Bashir, T. Pfeiffer, A. Mlynek, W. Wieser, A. Chamorovskiy, V. Shidlovski, and R. Huber, "850 nm FDML: performance and challenges," in *Proc.SPIE*(2023), p. 1236705.
159. N. Yang, Q. Qiu, J. Su, and S.-j. Shi, "Research on the temperature characteristics of optical fiber refractive index," Optik - International Journal for Light and Electron Optics **125**, 5813-5815 (2014).
160. R. Huber, and T. pfeiffer, "Method for preserving the synchronism of a Fourier Domain Mode Locked (FDML) laser " Optores, H01S3/139, (2021).
161. K. S. Park, E. Park, H. Lee, H.-J. Lee, S.-W. Lee, and T. J. Eom, "Phase stable swept-source optical coherence tomography with active mode-locking laser for contrast enhancements of retinal angiography," Scientific Reports **11**, 16636 (2021).
162. B. Braaf, K. A. Vermeer, V. A. D. P. Sicam, E. van Zeeburg, J. C. van Meurs, and J. F. de Boer, "Phase-stabilized optical frequency domain imaging at 1-μm for the measurement of blood flow in the human choroid," Optics Express **19**, 20886-20903 (2011).
163. Y. Miao, M. Siadati, J. Song, D. Ma, Y. Jian, M. F. Beg, M. V. Sarunic, and M. J. Ju, "Phase-corrected buffer averaging for enhanced OCT angiography using FDML laser," Optics Letters **46**, 3833-3836 (2021).
164. R. Huber, D. C. Adler, and J. G. Fujimoto, "Buffered Fourier domain mode locking: unidirectional swept laser sources for optical coherence tomography imaging at 370,000 lines/s," Optics Letters **31**, 2975-2977 (2006).
165. H. Yoda, P. Polynkin, and M. Mansuripur, "Beam quality factor of higher order modes in a step-index fiber," J. Lightwave Technol. **24**, 1350-1355 (2006).
166. A. Bradu, K. Kapinchev, F. Barnes, and A. Podoleanu, "Master slave en-face OCT/SLO," Biomedical Optics Express **6**, 3655-3669 (2015).
167. B. E. A. Saleh, and M. C. Teich, "*Fundamentals of Photonics,"* (Wiley-Interscience, 2007).
168. Gentec-eo, "Spot size and beam waist," https://www.gentec-eo.com/laser-calculators/beam-waist-spot-size.

LIST OF FIGURES AND EQUATIONS

ACRONYMS AND ABBREVIATIONS

ADC	Analog to digital converter
AlGaAs	Aluminum Gallium Arsenide
ASE	Amplified spontaneous emission
AWG	Arbitrary waveform generator
CCD	Charge coupled device
CFBG	Chirped fiber Bragg grating
CMS	Complex master-slave
COD	Catastrophic optical damage
CS	Channel spectrum
CW	Continuous wave
dB	Decibel
DBR	Distributed Bragg reflector
DGD	Differential group delay
DPX	Digital Phosphor Technology (X)
DSO	Digital storage oscilloscope
EOM	Electro-optics modulator
FDML	Fourier domain mode locked
FD-OCT	Fourier-domain optical coherence tomography
FFP-TF	Fiber Fabry-Pérot – Tunable filter
FF-SS-OCT	Full field – swept source – optical coherence tomography
FFT	Fast Fourier transform
FOV	Field of view
FS	Fiber spool
FSR	Free spectral range
FWHM	Full width half maximum
GaAs	Gallium Arsenide
GVD	Group velocity dispersion
iFFT	inverse fast Fourier transform
IPL	Inner plexiform layer

LASER	Light amplification by spontaneous emission of radiation
LED	Light-emitting diode
MECSEL	Membrane external-cavity surface-emitting laser
MEMS	Micro-electromechanical systems
MPE	Maximum permissible exposure
MZI	Mach-Zehnder Interferometer
OCT	Optical coherence tomography
OCTA	Optical coherence tomography angiography
OD	Optical density
OPL	Outer plexiform layer
OSA	Optical spectrum analyzer
PD	Photodiode
PM	Polarization maintaining
PMD	Polarization mode dispersion
RIN	Relative intensity noise
SD-OCT	Spectral-domain optical coherence tomography
SESAM	Semiconductor saturable absorber
SM	Single mode
SNR	Signal to noise ration
SOA	Semiconductor optical amplifier
SS-OCT	Swept-source optical coherence tomography
STD	Standard deviation
TD-OCT	Time-domain optical coherence tomography
TEC	Thermoelectric controller
VCSEL	Vertical cavity surface emitting laser
VECSEL	Vertical external cavity surface emitting laser